

2018

Multiphysics analysis of electrochemical and electromagnetic system addressing lithium-ion battery and permanent magnet motor

Abhishek Sarkar
Iowa State University

Follow this and additional works at: <https://lib.dr.iastate.edu/etd>

 Part of the [Electromagnetics and Photonics Commons](#), [Mechanical Engineering Commons](#), and the [Physics Commons](#)

Recommended Citation

Sarkar, Abhishek, "Multiphysics analysis of electrochemical and electromagnetic system addressing lithium-ion battery and permanent magnet motor" (2018). *Graduate Theses and Dissertations*. 17307.
<https://lib.dr.iastate.edu/etd/17307>

This Dissertation is brought to you for free and open access by the Iowa State University Capstones, Theses and Dissertations at Iowa State University Digital Repository. It has been accepted for inclusion in Graduate Theses and Dissertations by an authorized administrator of Iowa State University Digital Repository. For more information, please contact digirep@iastate.edu.

**Multiphysics analysis of electrochemical and electromagnetic system addressing
lithium-ion battery and permanent magnet motor**

by

Abhishek Sarkar

A dissertation submitted to the graduate faculty
in partial fulfillment of the requirements for the degree of

DOCTOR OF PHILOSOPHY

Major: Mechanical Engineering

Program of Study Committee:
Abhijit Chandra, Co-Major Professor
Pranav Shrotriya, Co-Major Professor
Ikenna C. Nlebedim, Co-Major Professor
Steve W. Martin
Kurt Hebert
Michael Olsen

The student author, whose presentation of the scholarship herein was approved by the program of study committee, is solely responsible for the content of this dissertation. The Graduate College will ensure this dissertation is globally accessible and will not permit alterations after a degree is conferred.

Iowa State University

Ames, Iowa

2018

Copyright © Abhishek Sarkar, 2018. All rights reserved.

TABLE OF CONTENTS

LIST OF FIGURES	iv
LIST OF TABLES	vii
ACKNOWLEDGEMENTS	viii
ABSTRACT.....	ix
CHAPTER 1. INTRODUCTION AND LITERATURE REVIEW	1
1.1 Composition and Working Principle	1
1.2 Literature Overview	2
1.3 Current Work	4
CHAPTER 2. PARAMETRIC ANALYSIS OF ELECTRODE MATERIALS FOR MECHANICAL PERFORMANCE OF LITHIUM-ION BATTERY: A MATERIAL SELECTION APPROACH	7
2.1 Introduction.....	7
2.2 Mathematical and Parametric Analysis	9
2.2.1 Mathematical Model	9
2.2.2 Material Characterization for Lithium Electrodes:	15
2.2.3 Constraints and Free Variables	16
2.3 Results and Discussions	18
2.3.1 Charging Index	20
2.3.2 Elastic and Plastic Indices.....	21
2.3.3 Stress Index.....	22
2.3.4 Fracture Index	22
2.4 Conclusions.....	28
CHAPTER 3. PARAMETRIC ANALYSIS OF ELECTRODE MATERIALS ON THERMAL PERFORMANCE OF LITHIUM-ION BATTERY: A MATERIAL SELECTION APPROACH	30
3.1 Introduction.....	30
3.2 Mathematical and Parametric Analysis	32
3.2.1 Thermal Model	32
3.2.2 Parametric Analysis	37
3.3 Results and Discussion	38
3.3.1 Entropic Index.....	40
3.3.2 Polarization Index	41
3.3.3 Joule Index	43
3.3.4 Plastic Heat Index	44
3.3.5 Thermal Diffusion Index	46
3.3.6 Effect of charging rate on heat generation in lithium battery electrodes....	49
3.4 Conclusions.....	50
CHAPTER 4. MODELING AND PROGNOSTICS OF SEPARATOR MELTDOWN FOR LITHIUM-ION POUCH CELLS UNDER COMPRESSION: BASED ON OPEN- CELL FOAM MODEL.....	52
4.1 Introduction.....	52
4.2 Mathematical Model	55

4.2.1 Conductivity-stress analysis for a foam-based separator model:.....	56
4.2.2 Chemo-thermal model for pouch cells:.....	58
4.3 Results and Discussion	61
4.3.1 Validation of separator model:.....	61
4.3.2 Prediction of ionic-conductivity for different separator materials:	62
4.4 Conclusion	71
CHAPTER 5. CHEMO-ECONOMIC ANALYSIS OF BATTERY AGEING AND CAPACITY FADE IN LITHIUM-ION BATTERY	72
5.1 Introduction.....	72
5.2 Mathematical Model	75
5.3 Economic Analysis	78
5.4 Results and Discussion	81
5.5 Conclusion	88
CHAPTER 6. BOLTZMANN TRANSPORT EQUATION BASED MODELS FOR PREDICTION OF MODE-DEPENDENT PHONON THERMAL CONDUCTIVITY OF SILICON NANOPARTICLE	90
6.1 Introduction.....	90
6.2 Mathematical Model	91
6.3 Results and Discussion	95
6.4 Conclusion	97
CHAPTER 7. THERMO-MECHANICAL ANALYSIS OF BRUSHLESS DC MOTOR FOR APPLICATION OF BONDED PERMANENT MAGNETS	99
7.1 Introduction.....	99
7.2 Magnet Model.....	102
7.3 Material property prediction	106
7.4 Conclusion	110
7.5 Appendix.....	111
CHAPTER 8. CONCLUSION AND FUTURE SCOPE.....	112
8.1 Summary and Conclusions	112
8.2 Future Work.....	115
REFERENCES	117

LIST OF FIGURES

Figure 1.1 Lithium-ion Battery Representation. Lithium-ion and electron transfer circuit diagram with porous electrode representation for lithium metal oxide battery during discharge.....	2
Figure 2.1 a) Lithium battery schematic during the discharge cycle, b) Lithium cathode stress domains during the discharge cycle.....	10
Figure 2.2 Stress distribution profile of a spherical lithium manganese oxide particle during lithiation under a) 1C, and b) 2C rate of charging.....	19
Figure 2.3 Material selection based on multivariable merit index comparison of charging rate index and elastic stress index.....	23
Figure 2.4 Material selection based on multivariable merit index comparison of charging rate index and plastic stress index.....	25
Figure 2.5 Material selection based on multivariable merit index comparison of fracture index and hydrostatic stress index.....	26
Figure 3.1 Schematic of lithium-ion battery during discharge cycle with heat generation.....	33
Figure 3.2 Material index formation process representation.	37
Figure 3.3 Heat generation and material selection based on entropic heating mechanism at 1C rate of charging.	40
Figure 3.4 Heat generation and material selection based on polarization heating mechanism at 1C rate of charging.	42
Figure 3.5 Heat Generation and Material Selection based on Joule Heating Mechanism at 1C rate of charging.	44
Figure 3.6 Heat generation and material Selection based on plastic heating mechanism at 1C rate of charging.	46
Figure 3.7 Merit index analysis to compare thermal generation based on four mechanisms against thermal diffusion characteristics of electrode material, a) Polarization, b) Entropic, c) Joule, and d) Plastic.....	47
Figure 3.8 Total heat generation vs rate of charging for different electrode materials.....	49
Figure 4.1 a) Schematic of lithium pouch cell under compressive load, b) Open-cell foam structure for separator model, c) Stress-strain schematic demarcating domains of elastic, plastic and densification characteristics for a foam-based separator.....	56
Figure 4.2 a) Strain-stress data for Celgard 2340 from Peabody and Arnold, 2011(Peabody and Arnold 2011) and curve-fit of model, b) Conductivity vs stress	

data from Peabody and Arnold, 2011 and predicted conductivity validation against experimental data.....	62
Figure 4.3 a – e) Curve-fit of stress-strain constitutive relation for PP, Trilayer, Non-woven, Ceramic-coated and PE separators against Zhang et al 2014, f) Conductivity prediction for five separator materials over 0 - 100 (MPa) applied compression.	64
Figure 4.4. Average cell temperature vs time over one charge discharge cycle at 1C (CCCC) for three lithium-ion pouch cells, i.e. LCO/C, LMO/C and LFP/C, with natural convection boundary condition ($h = 5\text{W/m}^2\text{-K}$) under; a – c) No-load condition; d – f) 50MPa applied compression.	66
Figure 4.5. Thermal map contour predicting variation of average cell temperature for LCO/C, LMO/C and LFP/C pouch cells over a range of stress (0 – 100 MPa) and rate of charging (0.5 – 3) for three separator material, a – c) monolayer PP, d – f) trilayer PP/PE/PP, g – i) Non-woven.	68
Figure 4.6. Thermal map contour predicting variation of average cell temperature for LCO/C, LMO/C and LFP/C pouch cells over a range of stress (0 – 100 MPa) and convection coefficient (1 – 10 W/m ² K) for three separator material, a – c) monolayer PP, d – f) trilayer PP/PE/PP, g – i) Non-woven.....	69
Figure 5.1 Single particle electrolyte model representation of a lithium-ion battery with SEI growth.	75
Figure 5.2 Single particle electrolyte model with battery degradation due to SEI formation, a) Representation of the charging protocol, b) Comparison of the model predicted data for LCO/C against experiments performed by Hu et al. (C. Hu et al. 2014), c) Comparison of model predicted data for LFP/C against experimental data from Liu et al. (P. Liu et al. 2010), d) Deviation of model prediction from experimental data for LCO/C and LFP/C.	82
Figure 5.3 Comparison of capacity fading on LCO/C cell with two charging protocols, a) CCCVZC protocol, b) CCCV protocol, c) Comparison of relative capacity fade over 1000 cycles from Profile I and II, d) Deviation of capacity between Profile I and II over 1000 cycles.	84
Figure 5.4 a) Capacity fade over 100 cycles for aged-batteries from ageing span of 0 - 9 years, b) Relative capacity of aged-battery at the end of 100 cycles.	85
Figure 5.5 Economic analysis of 18650 cells to compare the capacity fade performance of aged-batteries against the total cost of manufacturing and ageing the cells.	87
Figure 6.1 Thermal conductivity predictions for a 115 nm silicon nanoparticle as a function of temperature as obtained from the Klemens, Callaway and Holland models based on the parameters listed in Table 1 are compared against experimental measurements in the literature (D. Li et al. 2003). While the Klemens model significantly overpredicts the thermal conductivities beyond the low temperature region, the Callaway model shows reasonable concurrence with	

experimental data at very low and at near room temperatures. The Holland model provides the best estimates for the thermal conductivity, with predictions within ~20% of the measured values.	95
Figure 6.2 The variation of the relaxation time (τ) as a function of temperature (T) and vibrational frequencies (ω) are illustrated for the (a) transverse acoustic (TA) and the (b) longitudinal acoustic (LA) modes used in the Holland formulation of the Boltzmann transport equation. While the effect of T on relaxation time is weak at low temperatures, τ decreases significantly with increasing temperature for higher T values.	96
Figure 7.1. 3D FEA model for a 20W SPM Brushless DC motor.....	102
Figure 7.2 Torque/Output Power versus time for a 20W BLDC motor.	104
Figure 7.3. Thermal profile over 1 hour of operation of a 20W BLDC motor, a) Initial design, natural convection; b) Initial design with forced water cooling, and revised low current density design with natural convection.	105
Figure 7.4. Force profile over 1 cycle operation of 20W BLDC motor.	109
Figure 7.5. Von-mises stress contour for 20W BLDC motor, a) stator armature; b) rotor with magnets.	110
Figure 7.6 Motor prototyping, a) Design of stator and rotor laminates; b) Design of the motor casing.....	111

LIST OF TABLES

Table 2.1 Material properties for mechanical analysis three cathode and anode materials used in lithium-ion batteries.	17
Table 3.1 Material properties for thermal analysis three cathode and anode materials used in lithium-ion batteries.	39
Table 4.1 Chemo-thermal properties for cathode and anode materials used in current work (A. Sarkar, Shrotriya, and Chandra 2018).	60
Table 4.2 Fit Parameter for Peabody and Arnold, 2011(Peabody and Arnold 2011) data.	63
Table 4.3. Fit data for five different separator material(Arora and Zhang 2004; Baldwin et al. 2010; Yen 2002).	65
Table 5.1 Chemo-thermal properties for cathode (LCO and LFP), anode materials (C) and SEI.(A. Sarkar, Shrotriya, and Chandra 2018; Safari et al. 2009).	79
Table 5.2 Cost analysis data for 18650 cell (Baksa and Yourey 2018; U.S. Energy Information Administration 2018).	80
Table 6.1 The input and fitting parameters for crystalline silicon required to predict thermal conductivity using Klemens, Callaway and Holland formulations of the Boltzmann transport equation are listed.	94
Table 7.1 Design parameter for 20W BLDC motor.	103
Table 7.2 Model prediction results for thermal conductivity of 65 vol.% NdFeB.	107
Table 7.3 ANSYS mechanical model materials for 20W BLDC motor components.	108

ACKNOWLEDGEMENTS

I sincerely acknowledge the guidance provided by my advisors, Dr. Abhijit Chandra, Dr. Pranav Shrotriya and Dr. Ikenna Nlebedim, towards my progress as a PhD student. I would like to thank them for providing me with resources, literature and solving even the smallest doubts during this project. They have been excellent mentors and always supported me through all the downfalls and triumphs in the duration of the PhD. I would like to thank Dr. Steve Martin, Dr. Kurt Hebert and Dr. Michael Olsen for being a part of my PhD committee. They have been extremely supporting towards joining my committee. I acknowledge the guidance provided by my Dr. Helena Khazdozian, who as a post-doctoral research associate guided me through the multiphysics modeling of electromagnetic systems. I acknowledge the immense resources provided by Iowa State University, which has been elemental towards the targeted research.

I would like to thank my father, Mr. Dipak Sarkar, for providing me with technical advice and counselling during difficult phases of research. He has supported me in every aspect of my graduate college with his paternal guidance. I thank my mother, Mrs. Alpana Sarkar, for her support and affectionate care, and bearing my complaints and joining in my success throughout my PhD. Finally, I thank my family for providing me with the moral support to strive through my research.

ABSTRACT

Lithium-ion batteries are the leading energy storage technology in the electronic-driven society. With the need for portable, long-life electronics the demand for lithium batteries has escalated over the decade. Lithium-ion batteries show remarkable electrochemical characteristics, including but not limited to, long cycle-life, high cut-off voltages and high energy-density. However, lithium-ion cells are problematic to design due to their inherent thermal and/or mechanical instability. The objective of the current research framework is to establish the criteria causing thermo-mechanical failure of the battery systems, material properties effecting the performance, and model cycle-life degradation due to electrolyte loss by solid electrolyte interface (SEI) formation. An extension of this thermo-mechanical analysis was performed on electromagnetic system. A FEM was performed for a 20W BLDC motor to predict the electromagnetic and thermo-mechanical performance under steady state operating conditions.

In our present research, we have studied the mechanical and thermal aspect of lithium battery electrodes. The first and second project encapsulated the material selection aspect for thermo-mechanically stable lithium battery electrodes. The objective of these projects was to develop a set of material indices (five for mechanical and five for thermal) which compare the performance of electrode materials based on heat generation, diffusion and mechanical strength and toughness. A mathematical model was formulated to determine particle deformation and stress fields based upon an elastic-perfectly plastic constitutive response. Mechanical deformation was computed by combining the stress equilibrium equations with the electrochemical diffusion of lithium ions into the electrode particle. The result provided a time developing stress field which shifts from purely elastic to partially plastic deformation as the lithium-ion diffuses into the particle. For the mechanical integrity, the materials were tested for strength, and toughness under elastic and plastic deformation. The model was used to derive

five merit indices that parametrize mechanical stability of electrode materials. The five indices were used to analyze the mechanical stability for the six candidate electrode materials – graphite, silicon, and titanium oxide for the anode and lithium manganese oxide, lithium cobalt oxide and lithium ferrous phosphate for the cathode. Finally, the work suggested ways to improve the mechanical performance of electrode materials and helps to identify mechanical and design properties that need to be considered for optimal electrode material selection. Materials were selected based upon high strength and toughness with the ability to handle faster charging capabilities.

A coupled thermo-chemical model was developed and used for deriving the heat generation by electrode particle of different materials. The thermal merit index analysis was based on performing a multivariable material selection based on four mechanisms of thermal generation against the thermal diffusion characteristics of the electrode material. A new mode of heat generation was conceptualized plausible for fast charging electrode materials. The heat generated by this mechanism accounted for the strain energy dissipated due to plastic deformation of the electrode particles upon lithiation. A parametric analysis was conducted to compare the thermal performance of six candidate electrode materials (for cathode and anode) using the merit indices and the results were validated against past experimental data. The effect of variable charging rates on thermal generation was analyzed. Finally, the paper identified the material properties which affect the thermal performance of battery systems. The thermo-mechanical material indices were designed to be a tool or platform for industries and experimentalists to compare new with existing electrode materials and isolate the material properties that need to be altered for better performance of the battery.

The third project undertaken was to work on the concept of structurally integrable and mechanically robust lithium-ion pouch cells applicable for hybrid electric vehicles. Branching out from the focus area of flexible lithium batteries, a structurally stable cell could be integrated

with the body of the vehicle, thereby eliminating the additional weight and support needed to install a battery pack. The analysis involves the conceptualization of the lithium-ion separator membrane as an open-cell foam under compression and the decrement in the ionic-conductivity was modelled analogous to the permeability loss in a foamy material. The thermal profiling for three different lithium-ion cells (LCO/C, (lithium manganese oxide) LMO/C and LFP/C) were simulated with five separator materials under variable applied load, rates of charging and cooling conditions. A set of thermal maps were created to demarcate the domains of thermal meltdown of the separator membrane and the conditions leading up to the thermal runaway. The proposed model could be used as a design tool for industrial application of structurally flexible lithium-ion pouch cell to predict thermally safe lithium battery, thereby reducing the risks and loss from battery meltdown during prototyping.

The fourth project undertook the modeling of battery degradation and life prediction due to SEI growth resulting into capacity fading. An efficient reduced-order electrochemical model was developed for lithium cobalt oxide (LCO)/graphite (C) pouch cell and a reaction-diffusion based SEI model was integrated to predict the cyclic capacity loss due to electrolyte deposition over the anode in the form of SEI. The experimental data was fitted based on a single-parameter fit to predict the reaction coefficient for SEI current. The algorithm developed for this battery module was designed to reduce the computational time for capacity fade calculation. The model was also applied for a lithium ferrous phosphate (LFP)/C cell without any fitting, and in both cases the predictions were within $\pm 1\%$ deviation from the experimental results, thereby predicting capacity fading for different cathode materials with graphite as the anode.

A novel concept was developed in which “aged-battery” could be used as an advantage for biomedical and EV applications. The fading rate decays as the cell ages $\left(\propto \frac{1}{\sqrt{t}}\right)$ and aged-cells could be operated for longer life cycles with negligible fading. A cost analysis was

performed to find the optimized point where the benefits from lower fading was weighed against the cost (material and electricity) involved in ageing the cell. The application for this concept would be in biomedical and EV industries, where the replacement of lithium-ion batteries over short periods of time is not feasible and the cost/risk of replacement exceeds the cost of ageing the battery. Aging the cell could prolong its cycle life thereby reducing the chances of battery replacement in a long duration of operation.

The fifth project undertook a small project to compare the prediction of thermal conductivity by different approaches of Boltzmann Transport Equations. The lattice thermal conductivity predictions for a silicon nanoparticle was performed using three popular formulations of the Boltzmann transport equation. The models as proposed by Klemens, Callaway and Holland, essentially differ in the phonon scattering mechanisms and the vibrational modes considered in the respective formulations. At low temperatures, results from all three models showed strong agreement with experimental measurements but deviated significantly with increasing temperatures. Estimates from the Holland model, which explicitly accounted for the normal and Umklapp scattering processes of the transverse and longitudinal modes, concur with the measured values. Similar predictions were obtained from both Holland and Callaway models at high temperatures since phonon transport was dominated by longitudinal modes, as revealed from our analyses of the relaxation times. In conclusion, the paper inferred the importance of mode dependent thermal conduction in silicon nanoparticle at elevated temperatures.

The final work done was to model a 20W BLDC motor with bonded magnets used as the surface permanent magnet for the rotor. A thermo-mechanical and electromagnetic analysis was performed to test the application of the 65 vol.% bonded NdFeB magnets in a motor. The performance analysis involved the prediction thermo-mechanical properties for the bonded

magnets and redesign of the motor to operate at safe thermal and mechanical limits. The design was finalized and considered for prototyping as a part of the demonstration for the project.

In conclusion, a thermo-mechanical multiphysics analysis and material selection was performed primarily for electrochemical and extended to electromagnetic systems to predict performance, mechanism of degradation and cycle life under variable operating conditions. These model act as tools and design guide to aid in the development of lithium-ion batteries and electromagnetic drives. The purpose of modeling and material selection is to reduce the cost of experimentation and prototyping prior to commercialization. The multiphysics modeling performed also isolates the parameters which effect the health and safety of the system, thereby reducing the risks of failure during operation. Therefore, selection of the correct design parameters and models to support the performance and life predictions allow a rapid and economic transition from prototyping to commercialization of electrochemical and electromagnetic systems.

CHAPTER 1. INTRODUCTION AND LITERATURE REVIEW

Lithium-ion battery is the foremost technology in the field of energy storage with in the fields of electronics, electric transportation, aerospace applications and biomedical devices (Tarascon and Armand 2001). As compared to other rechargeable batteries, like Ni-Cd or NiMH, lithium ion batteries have a larger energy storage capacity, longer service life and higher energy density. Due to high reusability and energy density compared to other rechargeable batteries, the lithium-ion batteries are a favorable power option in electronic and automobile industries.

1.1 Composition and Working Principle

A lithium-ion battery works on the principle of electrochemical ion transfer due to a driving potential difference between the negative electrode (anode) and the positive electrode (cathode). An electrolytic solution; generally, the same salt solution as the ions transferred submerges the electrodes providing a pathway for the ions to transfer (Armand and Tarascon 2008). A Li-ion battery comprises of current collectors, electrodes, a separator and an electrolyte. The material and microstructures of electrodes and separators vary widely. The materials being used in today's Li-ion batteries include a graphite, silicon, and titanium oxide for negative electrode. For the cathode materials, transition metal oxides of lithium are popular including lithium manganese oxide (LMO), lithium ferrous phosphate (LFP) and lithium cobalt oxide (LCO). An ion-selective polymeric separator, like polypropylene or similar polymers, is used to allow lithium-ion exchange between electrodes while preventing short-circuit due to direct contact between electrodes. The cell is filled with an electrolyte made of lithium salts like lithium hexafluorophosphate, lithium hexafluoroarsenate monohydrate, lithium triflate, etc. The electrolyte conducts the lithium-ion from the anode to the cathode during discharging cycle and vice-versa during charging as shown in the following reaction.

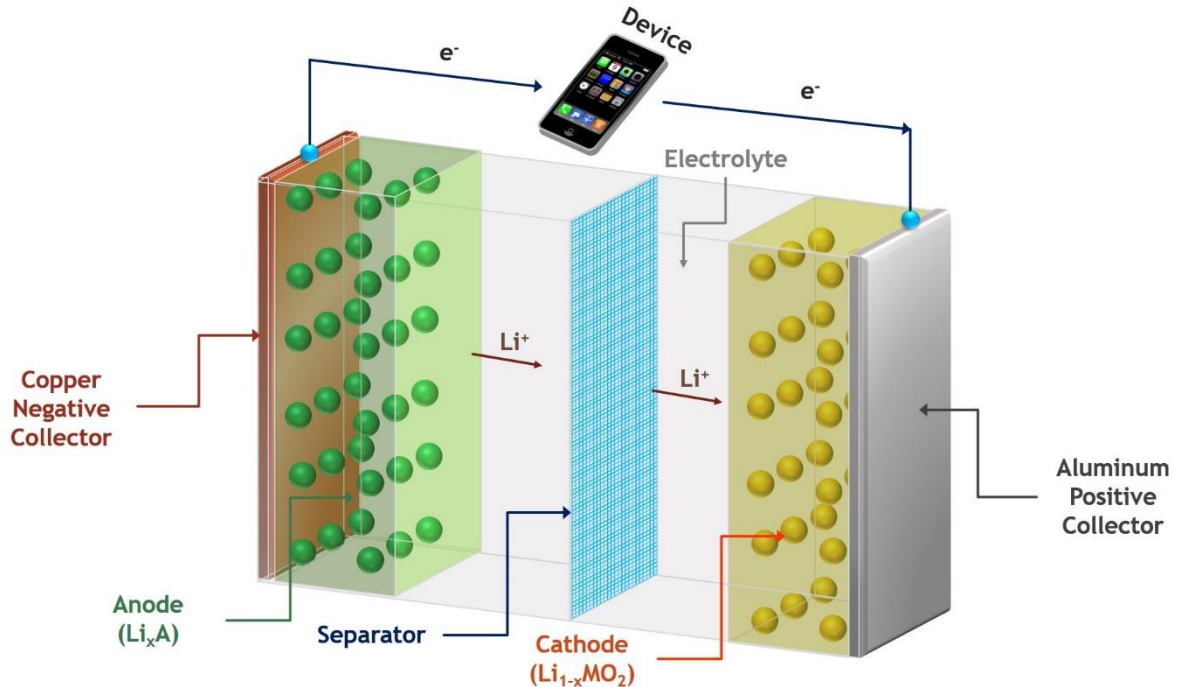
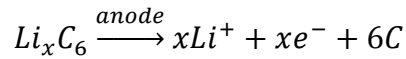
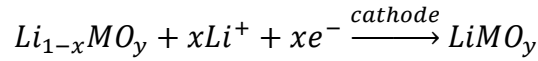


Figure 1.1 *Lithium-ion Battery Representation. Lithium-ion and electron transfer circuit diagram with porous electrode representation for lithium metal oxide battery during discharge.*

Figure 1.1 gives the 3D representation of a lithium-ion battery. During charging, the electrons flow into the anode and the Li^+ ion also flows towards the anode, to bond with the graphite (reduction) by absorbing the electron. The Li -ion is provided by the cathode, which oxidizes as it releases lithium-ion and electron. The opposite reaction occurs during discharge.

1.2 Literature Overview

Since the development of first commercial lithium-ion batteries by Sony in 1991, there has been paramount research and development related to this battery sector. These batteries are generally made with graphite as an anode and lithium cobalt oxide as a cathode (Whittingham 2004). However, cobalt oxide had several drawbacks including lower thermal stability (Joachim et al. 2009) and higher toxicity, which lead to the prominent use of manganese oxide as the cathode material. The current trend of research is focused on lithium-rich, manganese-

rich/nickel-rich, layered-lithium nickel manganese cobalt electrodes (NMC), which have become popular due to their ability to maintain high capacity ($>250\text{mAh/g}$) at operating discharge potential ($3.6\text{V} - 4.5\text{V}$) (Xiang et al. 2014; Fell et al. 2013).

Doyle et al (1993) (Doyle, Fuller, and Newman 1993) developed one of the earliest frameworks for electrochemical transport of species in a lithium-ion battery using concentrated solution theory, called the Newman porous electrode model. An application of the Newman porous electrode model was applied to graphite/LMO based battery (Doyle et al. 1996), where they validated the mathematical model with experimental results. Bernardi et al (1985) (Bernardi, Pawlikowski, and Newman 1985) developed a set equations defining different heating sources, like reactions, changes in heat capacity, phase change, mixing, electrical work and heat transfer with the surroundings. These equations were used by Thomas et al (2003) (Thomas and Newman 2003) in which they estimated the heat generation by $\text{Li}|\text{LiPF}_6$ in ethylene carbonate: dimethyl carbonate| $\text{LiAl}_{0.2}\text{Mn}_{1.8}\text{O}_{4.8}\text{F}_{0.2}$ cells and validated using isothermal calorimetry.

Zhang et al (2000) (D. Zhang, Popov, and White 2000) developed a simplified mathematical model to represent the lithium intercalation of a single spinel particle as a microelectrode under the stimulus of a cyclic linear potential sweep. Diffusion induced stress is a crucial cause of concern in lithium battery electrodes. The diffusion of lithium ions into electrodes during charge/discharge cause a concentration gradient due to the inherent diffusivity of the electrode material. Wang et al (2002) (W. L. Wang, Lee, and Chen 2002) developed a chemical stress model for a solid and a hollow cylindrical electrode being lithiated. Work by Zhang et al (2007) (Xiangchun Zhang, Shyy, and Sastry 2007) represented a stress model for spherical and ellipsoidal LMO electrode being intercalated under constant current conditions. They presented a fully three-dimensional simulation of ellipsoidal particles, to systematically study the intercalation-induced stresses developed in particles of various shapes

and sizes. They further worked on heat generation in electrode Zhang et al (2008) (Xiangchun Zhang, Sastry, and Shyy 2008). They developed a stress and heat generation model for an electrode spinel. They found that resistive heating, among resistive, entropic and heat of mixing, to be the most dominant heating source in battery electrode.

Two prominent works by Suo, Pharr and Zhao in 2010 (Y. Hu, Zhao, and Suo 2010; K. Zhao et al. 2010) have shown the fracture analysis of lithium-ion batteries using the fracture energy release rate as the criteria. Previous approaches by Zhao et al (2012) (K. Zhao et al. 2012) and Pharr et al (2012) (Pharr et al. 2012) towards mechanical analysis of silicon lithiation have either assumed a perfectly plastic material or elastic-perfectly plastic material response for amorphous lithiated silicon in order to accommodate the large volume expansion during lithiation. Xie et al (2016) (Xie et al. 2016) modeled the lithiated silicon response with a modulus of 80[GPa] and flow stress of 1[GPa] in silicon nanowires during lithiation. Nanoindentation tests on amorphous silicon have reported an elastic modulus within 8 – 12[GPa] (Berla et al. 2015) and tensile testing reveal the flow stress to be between 500 – 750[MPa] (Kushima, Huang, and Li 2012). The large discrepancy between the modeling assumptions and experimental results on mechanical response limit the understanding of silicon response to lithiation. The effect of tensile stresses in the silicon core on crack propagation, during lithiation during elastoplastic deformation of lithiated silicon, was studied by Sarkar et al (2017) (Abhishek Sarkar, Shrotriya, and Chandra 2017).

1.3 Current Work

Despite having several advantages in terms of performance, reliability and high energy storage, lithium-ion batteries are subject to thermal and mechanical stability leading to reduced performance, and in extreme cases, catastrophic failure during operation. Thereby, it is essential to study the reasons leading to failure of lithium-ion batteries and to develop the models for evaluations of the mechanical and thermal parameters for improvement of the future

generation of lithium-ion batteries. It is important to set up selection criteria for parameterizing and comparing new electrode materials.

The first work was based on the formulation of a chemo-mechanical model based on elastic-perfectly plastic deformation of spherical electrode particles. The stress field was evaluated over spatiotemporal domain to predict the growth of the plastic regime. The growth of the plastic regime was studied over multiple rates of charging. A set of material indices were developed from the coupled stress and diffusion equations for selection of electrode materials based upon their performance. Six candidate electrode materials were compared based on a multivariable parameterization approach to test their mechanical stability.

The second work presented a set of material indices derived from a thermo-chemical model of battery electrode to parametrize electrode materials based on their thermal performance. A novel conception was developed based on the heat generation due to plastic deformation of the electrode particle. Four heating mechanisms, i.e. polarization, entropic, joule and heat from plastic deformation, were evaluated. The heat of mixing is not considered as the battery was under constant charge-discharge cycling and the magnitude of this source was found to be a couple of order smaller than other sources. Five indices were created for comparison of electrode materials based on their thermal performance and the results were validated from prior experimental investigations.

The third task involved the thermo-chemical analysis of lithium-ion pouch cells under compressive loading. With the applications as structural units, these cells were simulated to predict the cycle temperature for different rates of charging, cooling characteristics and applied loading conditions. A novel model was proposed based on open-cell deformation of foam structure to simulate the separator membrane under compressive loading. A set of thermal contour maps were created to provide a design basis for selection of different combination of electrode and separators for lithium batteries.

The fourth task involved the development of a battery degradation electrochemical model to predict the cycle life and capacity fade in lithium battery due to SEI formation. An efficient numerical scheme was developed based on a reduced-order SPM to predict the electrochemical performance of LCO/C and LFP/C cells under variable loading conditions. A chemo-economic analysis was performed to demonstrate the concept of aged lithium-ion battery and their benefit of reduced effective fading over their cycle life.

The fifth work involved the prediction of thermal conductivity for silicon nanoparticles using three models based on Boltzmann Transport Equation (BTE) over a range of temperature. The final work was an extension of the thermo-mechanical analysis for multiphysics systems, involving performance prediction and material selection for electromagnetic system. A coupled thermo-mechanical and electromagnetic model was developed for a 20W Brushless DC motor with surface permanent magnets to test the application of the novel bonded magnets. The model was tested for thermo-mechanical performance under steady state operating conditions.

CHAPTER 2. PARAMETRIC ANALYSIS OF ELECTRODE MATERIALS FOR MECHANICAL PERFORMANCE OF LITHIUM-ION BATTERY: A MATERIAL SELECTION APPROACH

2.1 Introduction

Increasing energy demand and need for high energy density portable storage devices make lithium-ion batteries a prime source for energy storage and utilization in the electronic and electric vehicle industry (Armand and Tarascon 2008). With graphite/lithium cobalt oxide as the first electrode materials (Whittingham 2004), rigorous experimental and theoretical study on novel high capacity and stable electrode materials have allowed lithium batteries to achieve higher energy density, longer cycle life, and safer operation (Ellis, Lee, and Nazar 2010). Mechanical stability of new electrode materials for lithium-ion battery has been extensively investigated both experimentally and computationally. The literature provides datasets on electrode performance that have been generated from experiments, molecular dynamics simulation and multiphysics modeling of battery materials for life predictions (Lu et al. 2013). Recent developments have focused the work on experimentation and finite element modeling for understanding the thermo-mechanical functioning of electrodes and developing newer battery materials which show better mechanical and thermal performance at higher charging rates (Ramadesigan et al. 2012; Kermani and Sahraei 2017).

Mechanical stability of electrodes is crucial for life prediction of lithium-ion battery. Several electrode materials have been experimented to understand their performance under conditions of faster charging. Mechanisms governing lithium-ion diffusion and storage are different in different materials. For cathode materials, different lithium transition-metal oxides have been investigated including lithium manganese dioxide, lithium cobalt oxide, and lithium ferrous phosphate. Lithium manganese oxide gets oxidized in presence of lithium-ion and

diffusion process is governed by the chemical potential across the electrodes (J. J. Xu et al. 1998; Paulsen and Dahn 1999). In case of lithium cobalt oxide electrodes, there is a phase change from alpha to beta structure in presence of lithium ions (Gabrish, Yazami, and Fultz 2004; Padhi, Nanjundaswamy, and Goodenough 1997; Yamada et al. 2005). This process is diffusion driven but the phase change affects the kinetics of the diffusion process. Graphite has been popularly used as anode material in lithium-ion batteries (Etacheri et al. 2011). With recent development in nanotechnology, silicon nanoparticle-based electrodes have been tested as a promising anode material because of their large energy storage capacity (3579 mAh/g) (Chang et al. 2014). Graphite intercalates with lithium without any reaction. However, silicon in the first cycle reacts with lithium to convert from crystalline to amorphous structure (F. Wang et al. 2013; Abhishek Sarkar, Shrotriya, and Chandra 2017). For silicon, during the first cycle of charge, the process is kinetically driven because of smaller time scale for reaction than diffusion.

Analytical models predicting the stability of lithium-ion battery electrodes have either assumed a perfectly plastic material or an elastic-perfectly plastic material behavior during lithiation (K. Zhao et al. 2012; Pharr et al. 2012). Christensen et al. modeled lithiation induced stress development assuming that stress is a function of the lithium-ion concentration gradient in the particle (Christensen and Newman 2006a). Zhang et al (Xiangchun Zhang, Shyy, and Sastry 2007; Xiangchun Zhang, Sastry, and Shyy 2008), modeled the radial and hoop stress development in ellipsoidal particles considering elastic deformation of lithium manganese oxide spinel in fully coupled stress-diffusion models. In contrast, perfect plasticity-based models have been developed for anode materials (especially silicon) (K. Zhao et al. 2012, 2011; Sethuraman et al. 2013). These models considered pure plasticity due to small impact of the elastic deformation compared to the plastic deformation leading to material failure. TEM analysis by Liu et al (X. H. Liu et al. 2012) has shown plastic deformation of 320% by silicon

during lithiation. The transition from the graphite-based anode to a combination of graphite with silicon electrode is a step towards development and selection of novel electrode materials for obtaining high energy storage lithium batteries. The research focused on novel materials like layered-lithium nickel manganese cobalt electrodes (NMC), which have become popular due to their high capacity ($>250\text{mAh/g}$) at high discharge potential ($3.6\text{V} - 4.5\text{V}$) (Xiang et al. 2014; Fell et al. 2013). However, these electrodes are mechanically unstable in high potential domains. Therefore, there is a need for material selection techniques that highlight the chemo-mechanical properties critical towards better characterization of electrode materials.

Motivated by the advancements in the field of materials for newer battery electrodes, a rigorous mathematical formulation for an elastic-perfect plastic diffusion-induced stress model in a spherical electrode particle was developed in this work. The model was used to study the stress evolution and fracture response in electrode particles of different materials. A set of five merit indices were created which parameterize the materials based on their mechanical performance and fracture stability. A detailed analysis of these indices provided an insight of the material properties useful for a performance boost of the electrode materials. Six electrode materials, three for the cathode and three for the anode, were selected for this study. The results discussed the electrode materials that stand out among the others for having the better mechanical stability and fracture resistance. The paper concludes with a detailed understanding of the crucial material properties which influence the life of a battery, a set of indices to compare new materials with existing data and an approach to improve the mechanical performance of lithium-ion battery electrode.

2.2 Mathematical and Parametric Analysis

2.2.1 Mathematical Model

A lithium-ion battery works by the principle of electrochemical diffusion due to a potential difference between the electrodes by exchanging lithium ions. As the cell discharges

the lithium ions diffuse into the cathode from the anode, thereby converting chemical energy into electrical work. The Figure 2.1 and Equations (2.1, 2.2) represent the discharge reaction in any generic lithium transition metal during the discharging process.

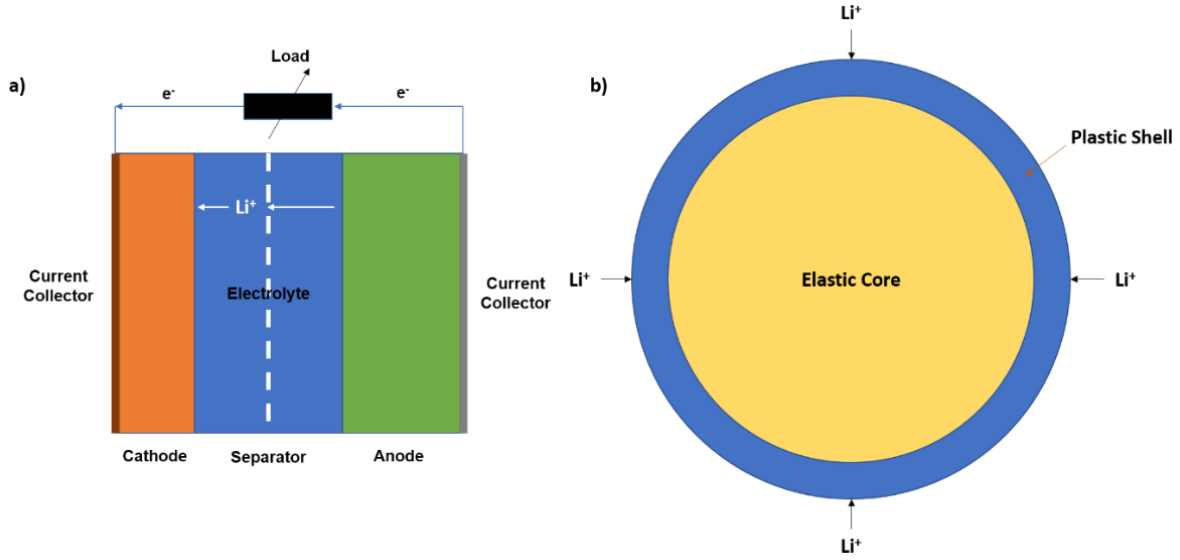
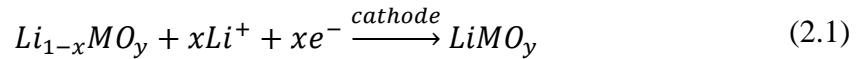


Figure 2.1 a) *Lithium battery schematic during the discharge cycle*, b) *Lithium cathode stress domains during the discharge cycle*.



During discharge, lithium ions dissociate from the anode and intercalate with the cathode, made up of a metal oxide of lithium, to form a lithium intercalation compound and vice-versa during charging. An understanding of the diffusion/reaction mechanism is crucial towards material selection. Many mathematical models have been developed based on the elastic deformation of electrode particle which predicts the mechanical performance of certain electrode materials (Xiangchun Zhang, Shyy, and Sastry 2007; Xiangchun Zhang, Sastry, and Shyy 2008; F. Yang 2005). To model the deformation in the plastic regime certain assumptions have been made to simplify the complexity of the highly involved chemo-mechanical equations which govern the battery cycling and performance mechanism. The porous electrode theory was considered for this analysis (Christensen and Newman 2006a) with the electrolyte to be an

infinite source of lithium ion. The particle surface was assumed to expand freely (nor surface radial stress) and the material was assumed perfectly plastic at yield point. The above assumptions were used to formulate species transport equation which is influenced by the hydrostatic stress due to diffusion. The mass transport of lithium ions in the electrode material depends upon the gradient of the electrochemical potential.

$$J = cV = -cM\nabla\mu \quad (2.3)$$

Where, μ is the electrochemical potential, M is the mobility and c is the lithium-ion concentration. The electrochemical potential is a function of both concentrations of the ion and the chemical stress generated.

$$\mu = \mu^0 + RT\ln(x) - \Omega\sigma_h \quad (2.4)$$

Where, σ_h is the hydrostatic stress on the particle due to differential expansion, Ω is the partial molar volume, μ^0 is the electromotive potential and x is the mole fraction of lithium in the particle. Substituting the electrochemical potential (Equation 2.4) into mass flux (Equation 2.3), the equivalent stress dependent ion flux equation was derived.

$$J = -Mc \left[RT \frac{\nabla c}{c} - \Omega \nabla \sigma_h \right] = -D \left[\nabla c - \frac{\Omega c}{RT} \nabla \sigma_h \right] \quad (2.5)$$

Where, D is the mass diffusion coefficient of the lithium-ion in the electrode, R is the gas constant and T is the operating temperature. Fick's Law of diffusion was expressed for a spherically symmetric particle from the diffusion mass flux (Equation 2.5).

$$\frac{\partial c}{\partial t} = D \left[\frac{1}{r^2} \frac{\partial}{\partial r} \left(r^2 \frac{\partial c}{\partial r} \right) - \frac{\Omega}{RT} \left\{ \frac{\partial c}{\partial r} \frac{\partial \sigma_h}{\partial r} + \frac{c}{r^2} \frac{\partial}{\partial r} \left(r^2 \frac{\partial \sigma_h}{\partial r} \right) \right\} \right] \quad (2.6)$$

To solve this differential equation, a set of boundary and initial conditions were needed. To decouple the stress from the concentration, it is necessary to solve the mechanical aspect of the problem. The following boundary conditions were applied to the mass transport equation.

$$i = \frac{\alpha \rho r_0}{3} C_{rate} \quad (2.7)$$

$$J|_{r=r_0} = \frac{i}{F} \quad (2.8)$$

$$\left. \frac{\partial c}{\partial r} \right|_{r=0} = 0 \quad (2.9)$$

For a spherical particle, the current flux on the surface depends on the theoretical capacity of the electrode material (α), density (ρ), Faraday's constant (F), radius (r_0) and the rate of charging (C_{rate}). At the center of the spherical electrode particle, an asymptotic boundary condition was considered. The current was assumed constant during charging/discharging and dependent on the rate of charging. The initial condition was considered as zero lithium-ion concentration throughout during lithiation and maximum lithium-ion concentration during delithiation.

Equation 2.6 shows hydrostatic stress coupled with lithium-ion concentration, which affects the diffusion process. The intercalation of lithium-ion into the electrode causes an expansion (displacement) of the particle. Particle expansion leads to shifting of atomic planes causing dislocation. The dislocation of atoms from their natural lattice sites leads to the generation of a stress field in the particle. Assuming the stress within the limits of elastic isotropic behavior, the strain is to stress using the Hooke's Law. During lithiation, the spherical electrode particle expands and vice-versa during delithiation. So, the formulation of the elastic component of strain was found similar to the strain produced during to thermal expansion (Xiangchun Zhang, Shyy, and Sastry 2007).

$$\varepsilon_r^e = \frac{1}{E} [\sigma_r - 2\nu\sigma_\theta] + \frac{\tilde{c}\Omega}{3} = \frac{du}{dr} \quad (2.10)$$

$$\varepsilon_\theta^e = \frac{1}{E} [(1 - \nu)\sigma_r - \nu\sigma_\theta] + \frac{\tilde{c}\Omega}{3} = \frac{u}{r} \quad (2.11)$$

$$\tilde{c} = c - c_0 \quad (2.12)$$

The radial (ε_r) and hoop (ε_θ) strain equations depended upon the concentration variation across the particle. Where, E is the modulus of elasticity, ν is the Poisson's ratio, u is the radial

displacement and c_0 is the initial lithium-ion concentration. As the electrode got further lithiated, the equivalent stress could exceed the yield stress pushing the material to deform plastically. For a spherical particle, the yield criterion is given below.

$$|\sigma_r - \sigma_\theta| \leq S_y \quad (2.13)$$

When the stresses go beyond the yield limit (S_y), the total strain generated was due to both the elastic and plastic deformation of the particle. Figure 2.1(b) represents the elasto-plastic schematic of a cathode particle during lithiation. The total (hydrostatic) strain would be equal to the summation of the volumetric elastic and plastic strain.

$$\varepsilon_{ij} = \varepsilon^e_{ij} + \varepsilon^p_{ij} \quad (2.14)$$

Since the particle was assumed completely spherical, the stress equilibrium equation was solved in the spherical coordinates considering radial symmetry.

$$\frac{\partial \sigma_r}{\partial r} + \frac{2}{r}(\sigma_r - \sigma_\theta) = 0 \quad (2.15)$$

Where, σ_r is the radial stress component and σ_θ is the hoop stress component. This equation was solved for the elastic segment by substituting the elastic displacements and for the plastic part by substituting the yield equality into the equilibrium equation. The stress equilibrium was solved using the following boundary conditions (Bower 2009).

$$\left. \frac{\partial \sigma_r^{el}}{\partial r} \right|_{r=0} = 0 \quad (2.16)$$

$$\sigma_r^{el} = \sigma_r^{pl} |_{r_p} \quad (2.17)$$

These conditions satisfied the radial stress continuum at the core and interface between elastic and plastic domain (r_p). The plastic stress was solved by substituting the yield equality into the stress equilibrium equation with free expansion along the radial direction on the surface.

$$\sigma_r^{pl} |_{r_o} = 0 \quad (2.18)$$

The stress (radial and hoop) was calculated by solving the elastic-perfectly plastic equations for the plastic domain.

$$\sigma_r^{pl} = 2S_y \ln \left[\frac{r_o}{r} \right]; r_p \leq r \leq r_o \quad (2.19)$$

$$\sigma_\theta^{pl} = 2S_y \ln \left[\frac{r_o}{r} \right] - S_y; r_p \leq r \leq r_o \quad (2.20)$$

The differential equation for the elastic domain was solved by using the plastic radial stress at the plastic interface.

$$\sigma_r^{el} = 2S_y \ln \left[\frac{r_o}{r_p} \right] + \frac{2\Omega E}{3(1-\nu)} \left[\frac{1}{r_p^3} \int_0^{r_p} \tilde{c} r^2 dr - \frac{1}{r^3} \int_0^r \tilde{c} r^2 dr \right]; 0 \leq r \leq r_p \quad (2.21)$$

$$\sigma_\theta^{el} = 2S_y \ln \left[\frac{r_o}{r_p} \right] + \frac{\Omega E}{3(1-\nu)} \left[\frac{2}{r_p^3} \int_0^{r_p} \tilde{c} r^2 dr + \frac{1}{r^3} \int_0^r \tilde{c} r^2 dr - \tilde{c} \right]; 0 \leq r \leq r_p \quad (2.22)$$

The mean (hydrostatic) stress was found for the elastic and plastic equations.

$$\sigma_h = \frac{\sigma_r + 2\sigma_\theta}{3} \quad (2.23)$$

$$\sigma_h^{pl} = 2S_y \ln \left[\frac{r_o}{r} \right] - \frac{2}{3} S_y; r_p \leq r \leq r_o \quad (2.24)$$

$$\sigma_h^{el} = 2S_y \ln \left[\frac{r_o}{r_p} \right] + \frac{2\Omega E}{9(1-\nu)} \left[\frac{3}{r_p^3} \int_0^{r_p} \tilde{c} r^2 dr - \tilde{c} \right]; 0 \leq r \leq r_p \quad (2.25)$$

The elastic and plastic stresses (in Equations 2.24 and 2.25) were substituted into Equation 2.6 to decouple the concentration from stress.

$$\frac{\partial c}{\partial t} = D \left[\frac{1}{r^2} \frac{\partial}{\partial r} \left(r^2 \frac{\partial c}{\partial r} \right) + \theta \left(\frac{\partial c}{\partial r} \right)^2 + \theta c \left\{ \frac{1}{r^2} \frac{\partial}{\partial r} \left(r^2 \frac{\partial c}{\partial r} \right) \right\} \right]; 0 \leq r \leq r_p \quad (2.26)$$

$$\frac{\partial c}{\partial t} = D \left[\frac{1}{r^2} \frac{\partial}{\partial r} \left(r^2 \frac{\partial c}{\partial r} \right) - \frac{\Pi}{r} \left(\frac{c}{r} + \frac{\partial c}{\partial r} \right) \right]; r_p \leq r \leq r_o \quad (2.27)$$

Where, $\theta = \frac{2\Omega^2 E}{9RT(1-\nu)}$ and $\Pi = \frac{2S_y \Omega}{RT}$ are constants which couple the gap between stress driven concentration and diffusion driven concentration in the elastic and plastic equations respectively.

The fracture of the spherical electrode during lithiation occurs due to the hoop stress. The particle having a circumferential crack may open when sufficient load is applied based on the fracture mechanics of the electrode. The simplest model for an edge crack relates the stress intensity with the applied stress and crack size.

$$K_I = C \sigma_\theta \sqrt{\pi a} \quad (2.28)$$

Where a is the crack depth from the surface, K_I is the stress intensity factor and C is a geometric factor.

2.2.2 Material Characterization for Lithium Electrodes:

The stress generation in a lithium battery electrode influences its performance and life. The mathematical model showed how diffusion could lead to stress generation in the electrode. The concentration gradient during lithiation could push the domain to plasticity when the equivalent stress exceeds the yield criteria. The life of the battery depends on the hoop stress and critical stress intensity of the given material. The diffusion-induced stress depends on several physical and material properties like particle diameter, state of charge, theoretical capacity, specific molar volume, yield strength, Young's Modulus, etc. From experimentation, it is known that different materials intercalate differently, some undergoing phase transformation while reacting with lithium. However, the lithiation process is diffusive for all battery materials. Therefore, it is reasonable to compare different candidate electrode materials based on their material properties.

The parametric analysis was performed based on three fundamentals. First was the selection of a quantity or parameter that needs to be optimized. The second was a set of constraints which allow the selection of suitable approximations to create a common ground

for comparison. The third was a free variable that could be used to substitute the constraint into the quantity to be optimized (Ashby 2005). Five material indices (M) were created in this paper to express mechanical performance and fracture resistance.

2.2.3 Constraints and Free Variables

In the mechanical parametric analysis of battery systems, it is important to set certain constraints to limit the degree of variability of the material indices. These constraints allow comparison on a homogenous basis and provide flexibility to set certain parameters common for all materials to be compared.

Setting the average non-dimensional concentration profile to a constant allows all electrode particles to have the same amount of lithium ions diffused within them.

$$\hat{c}(\hat{r}) = \frac{c}{c_{max}} = Cons \quad (2.29)$$

Another constraint was to set time of diffusion or the particle radius as constant. This became slightly challenging as keeping equal radius particle seems to be a more apt decision (from a manufacturing perspective). However, from an electrochemist point of view, the time required for charging was crucial compared to the radius of the particle. Comparison based on equality of temporal coordinates was more suitable.

$$\hat{t} = \frac{tD}{r_o^2} \quad (2.30)$$

If the total time required for diffusion was constant, and the following could be stated.

$$r_o \propto \sqrt{D} \quad (2.31)$$

Table 1 provides the data for six electrode materials that are popularly studied and used in lithium-ion batteries.

Table 2.1 *Material properties for mechanical analysis three cathode and anode materials used in lithium-ion batteries.*

Properties	LiMn ₂ O ₄	LiCoO ₂	LiFePO ₄	Li _x C	Li _x Si	Li _x TiO ₂
D (m ² /s)	7.08×10 ⁻¹⁵ (Christensen and Newman 2006a)	1.00×10 ⁻¹³ (Renganathan et al. 2010)	7.96×10 ⁻¹⁶ (Satyavani et al. 2016)	3.90×10 ⁻¹⁴ (Renganathan et al. 2010)	1.00×10 ⁻¹⁶ (Ma et al. 2015)	6.80×10 ⁻¹⁵ (M. Chen et al. 2015)
ρ (kg/m)	4100 (Christensen and Newman 2006a)	5030 (Renganathan et al. 2010)	3600 (Y. Zhu and Wang 2010)	2100 (Renganathan et al. 2010)	2328 (Dash and Pannala 2016)	3510 (“Lithium Titanate” 2017)
α _{th} (mAh/g)	148 (Julien et al. 2014)	166 (Julien et al. 2014)	170 (Julien et al. 2014)	372 (Julien et al. 2014)	4200 (Julien et al. 2014)	175 (Kam and Doeff 2012)
c _{max} (mol/m ³)	2.29×10 ⁴ (Christensen and Newman 2006a)	4.99×10 ⁴ (Renganathan et al. 2010)	2.12×10 ⁴	3.05×10 ⁴ (Renganathan et al. 2010)	8.87×10 ⁴ (L. Chen et al. 2014)	5.00×10 ⁴ (M. Chen et al. 2015)
Ω (m ³ /mol)	3.50×10 ⁻⁶ (Christensen and Newman 2006a)	1.92×10 ⁻⁶ (Renganathan et al. 2010)	67.32×10 ⁻⁶ (Lundgren 2015)	3.17×10 ⁻⁶ (Renganathan et al. 2010)	32.25×10 ⁻⁶ (K. Zhao et al. 2010)	5.00×10 ⁻⁶ (M. Chen et al. 2015)
S _y (MPa)	776 (Kushima, Huang, and Li 2012)	1056 (Qi et al. 2014)	500 (Qi et al. 2014)	23 (Julien et al. 2014)	720 (X. H. Liu et al. 2012)	836
E (GPa)	194 (Qi et al. 2014)	264 (Qi et al. 2014)	125 (Qi et al. 2014)	10 (Qi et al. 2014)	12 (Berla et al. 2015)	209 (Qi et al. 2014)
N	0.26 (Qi et al. 2014)	0.32 (Qi et al. 2014)	0.28 (Qi et al. 2014)	0.24 (Qi et al. 2014)	0.25 (Qi et al. 2014)	0.19 (Qi et al. 2014)
K _{1C} (MPa-m ^{0.5})	1.50 (Wolfenstine et al. 2013)	1.30 (Wolfenstine et al. 2013)	1.50 (Wolfenstine et al. 2013)	1.25 (Wolfenstine et al. 2013)	1.00 (Wolfenstine et al. 2013)	1.50 (Wolfenstine et al. 2013)

Thus, the radius emerges out to be the free variable which is substituted the square root of the diffusion coefficient in the material indices. Another constraint was attained from the yield criterion.

$$\sigma_r^{el} - \sigma_\theta^{el} = \frac{\Omega E}{3(1-\nu)} \left[\tilde{c} - \frac{3}{r_p^3} \int_0^{r_p} \tilde{c} r^2 dr \right] \leq S_y \quad (2.32)$$

In the dimensionless form, $\hat{c} = \frac{\tilde{c}}{c_{max}}$ was substituted and from Equation 2.29, the integral term became constant. The maximum allowed concentration was expressed proportional to the yield stress.

$$c_{max} \propto \frac{S_y(1-\nu)}{\Omega E} \quad (2.33)$$

The temperature was also assumed constant. For the fracture analysis, the upper limit for the stress intensity factor was bound by the fracture toughness of the material.

$$K_I \leq K_{1c} \quad (2.34)$$

2.3 Results and Discussions

An elastic-perfectly plastic chemical diffusion model was developed to perform the stress and fracture analysis during lithiation of different electrode materials. The electrode materials were compared based on their mechanical stability, ability to handle faster charging without yielding and higher fracture characteristics. The lithiation process was considered with the same mechanism for candidate materials, avoiding any effects of reaction or phase transformation. The indices were created based on the assumption of constant concentration, diffusing at constant time and at a constant temperature of 298K. The equations for the stress analysis and merit indices was solved using MatLab platform (MATLAB 2017).

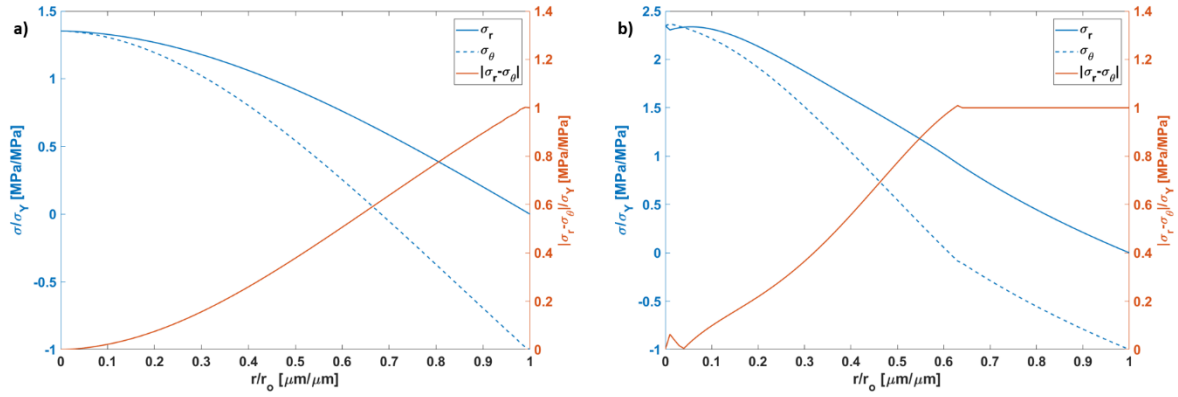


Figure 2.2 Stress distribution profile of a spherical lithium manganese oxide particle during lithiation under a) 1C, and b) 2C rate of charging.

The diffusion of lithium ions during (de)lithiation of the electrodes generate a stress field inside the electrode particle. The rate of charging is defined as the time required to charge the battery in one hour (= 1C). During lithiation, the lithium-ion concentration is higher near the surface of the particle and decreases near the core which occurs due to the effect of Fick's law of mass diffusion. The intercalation of lithium-ion with the electrode material causes it to expand proportionally to the relative concentration of lithium-ion. Therefore, the surface of the particle tries to expand more during lithiation than the core. This variable degree of expansion causes the surface to be under compression while the core to be under tension. The mathematical analysis in this paper was formulated considering the electrode material to be elastic and perfectly plastic. Therefore, when the yield criteria (Equation 2.13) was obtained, the equivalent stress ($|\sigma_r - \sigma_\theta|$) remained equal to the yield stress of the material, while the material kept expanding plastically. In Figure 2.2, the normalized stress distribution was plotted against the normalized radius of a lithium manganese oxide particle. The lithium manganese oxide particle was considered of 10 μm in radius and charged under 2C and 3C rates of charging. The plastic deformability of lithium manganese oxide has been experimentally observed by Kosova et al. (Kosova et al. 2000) and Schilcher et al. (Schilcher, Meyer, and Kwade 2016). For the 2C charging rate, the lithium manganese oxide particle was barely plastic near the particle surface, where the equivalent stress equaled the yield stress of the material.

However, with an increase in the charging rate to 3C, the electrode particle deformed plastically from the surface till about $0.65r_0$. The stress distribution in the 2C case was found to be much more uniform, while for higher rate of charging, the stress profile became sharp in the plastic shell. This pushed the tensile stress domain in the core to a very high stress state. It was interesting to note that the stress (radial and hoop) was 1.3 times and 2.4 times in magnitude of the yield stress for the 2C and 3C cases, respectively. However, the material does not fail under such high loads because the equivalent stress near the core was nearly zero (zero at the center). Hence, the material was under a purely tensile hydrostatic load which prevented failure because the electrode particle was considered to be solid without any crack. It could be inferred that the presence of small voids or microcracks in this domain, as observed experimentally in silicon (Kushima, Huang, and Li 2012), would lead to the voids to coalesce and form cracks. These cracks would propagate rapidly towards the surface and get closed in the compressive domain near the surface. This would lead to failure of the electrode material above a certain dimension and rate of charging. From the above analysis, it could be inferred that lithium manganese oxide particles of $10\mu\text{m}$ radius are safe for operation under 2C charging rate.

2.3.1 Charging Index

Faster rate of (dis)charging is one of the most desired outcomes of battery research. A material that can maintain its performance when (dis)charged faster is more desirable in the industry. Under the constraint of yield (Equation 2.33), the boundary condition in Equation 2.8 was modified by substituting the flux from Equation 2.5 and elastic stress from Equation 2.25.

$$-D \frac{\partial c}{\partial r} (1 + \theta c) = \frac{i}{F} \quad (2.35)$$

Equation 2.35 was normalized with $\hat{c} = \frac{\tilde{c}}{c_{\max}}$, $\hat{r} = \frac{r}{r_0}$ and the current flux term was expanded from Equation 2.7.

$$-\frac{\partial \hat{c}}{\partial r} (1 + \theta c_{max} \hat{c}) = \frac{\rho \alpha r_o^2}{DF c_{max}} C_{rate} \quad (2.36)$$

Ignoring one in the left bracket and considering constraint of constant concentration and gradient from Equation 2.29, time constraint (Equation 2.30) and approximation for maximum concentration from Equation 2.33, we could evaluate the rate of charging. The following merit index was minimized for the objective of determining materials that could handle higher rates of charging.

$$M_{Cr} = \frac{\rho E \alpha}{S_y^2 (1 - \nu)^2} \quad (2.37)$$

The charging rate merit index parameterizes materials based on their ability to handle high charging rates without yielding. This index was created with the constraint on the maximum lithium ion concentration that the electrode material could hold without yielding. Moreover, the time of complete lithiation remains constant for all the materials compared. A material that can store more charge in a lesser time without yielding shows better promise as a future battery material for HEV battery systems.

2.3.2 Elastic and Plastic Indices

The concentration partial differential equations (Equation 2.26, 2.27) were related to stress-based diffusion through θ and Π . These terms influence the diffusion process. The elastic equation was promoted by θ (additive), while the plastic equation reduced with the increase of Π (subtractive). The concentration gradient during diffusion should be minimized for lower stress response. So, the elastic merit index and the plastic merit index should be minimized.

$$M_{El} = \frac{\Omega^2 E c_{max}}{(1 - \nu)} \quad (2.38)$$

$$M_{Pl} = \frac{1}{S_y \Omega} \quad (2.39)$$

From Equation 2.25, it is understandable that the diffusion equation gets modified by the addition of extra concentration terms from the mean elastic stress field. These terms deviate

the concentration distribution from its general parabolic structure to a higher gradient distribution, resulting in hindered diffusion in the particle. Higher gradient, or slower diffusion, leads to high stress build up and battery not being utilized to its utmost potential. It is crucial to understand the importance of this effect and find ways to minimize its impact on the diffusion process.

2.3.3 Stress Index

Under elastic loading, the hydrostatic stress in Equation 2.25 was influenced by the concentration gradient in the particle. For very small plastic stress effects and normalizing the concentration and radius, the elastic mean stress could be simplified.

$$\hat{\sigma}_h^{el} \propto \frac{\Omega E c_{max}}{S_y(1-\nu)} \left[\frac{3}{\hat{r}_p^3} \int_0^{\hat{r}_p} \hat{c} \hat{r}^2 dr - \hat{c} \right] \quad (2.40)$$

The stress was normalized by the yield stress and the integral part is constant (Equation 2.29). The merit index for stress was minimized for prediction of low stress induced materials.

$$M_{St} = \frac{\Omega E c_{max}}{S_y(1-\nu)} \quad (2.41)$$

Equation 2.25 expressed the hydrostatic stress for the elastic domain. The stress developed in the battery was dependent on the concentration profile due to stress-driven diffusion. In the normalized form, the collection of material properties in front of the integral terms needed to be minimized to reduce the effect of stress.

2.3.4 Fracture Index

The fracture formulation (Equation 2.28), with the hoop stress from Equation 2.25 (simplified for negligible yield stress) and the fracture toughness constraint (Equation 2.34), was used to express the detectable crack length, which needed to be maximized for longer life. Therefore, the merit index was minimized in order to select a material with high fracture resistance.

$$M_{Fr} = \frac{\Omega E c_{max}}{K_{1c}(1 - \nu)} \quad (2.42)$$

Material under stress tends to fail in the presence of cracks. Cracks or flaws act as stress concentrators which magnify the local stress field. If the crack size is beyond the critical limit, the stress at the crack tip exceeds the fracture strength of the material causing failure due to crack propagation.

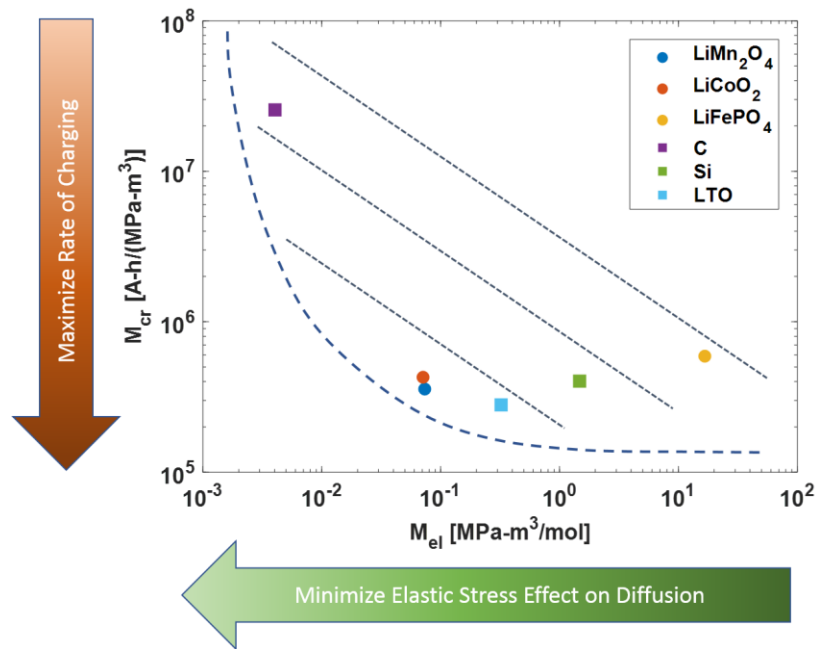


Figure 2.3 Material selection based on multivariable merit index comparison of charging rate index and elastic stress index.

Figure 2.3 demonstrates a multivariable comparison between the merit index based on maximizing the charging rate and the merit index for reducing the effect of elastic stress on diffusion. The objective of this comparison was the selection of high capacity electrode materials which could maintain the lithium-ion storage capacity under heavy elastic deformation. The elastic merit index was dependent on the partial molar volume, modulus of elasticity and maximum concentration of lithium that the material can store. All these terms need to be minimized for lower elastic effects on diffusion. The partial molar volume of an electrode material represents the percentage volumetric expansion a material undergoes when

it's lithiated. Since the elastic stress is dependent on the degree of volumetric expansion, this property should be minimized for lower elastic stress generation.

The selected electrode materials, three for the cathode and three for the anode, were compared based on the formulated indices. Figure 2.3 shows that lithium manganese oxide was the most suitable material for the cathode and lithium titanate showed good promise for anode based on their high charge storage capability and low effects of elastic stress on lithium diffusion. It has been experimentally validated that lithium manganese oxide is more stable than commercially used lithium cobalt oxide (Scrosati and Garche 2010). The three-dimensional structure of the manganese oxide spinel allows more space for intercalation with lithium ions during discharge and vice-versa for charge (Paulsen and Dahn 1999). This meant manganese oxide allows faster lithiation without significant deformation. Silicon shows a tremendous performance compared to graphite, based on the ability to be operated at high charging rates. This was validated from the experimental results by Chan et al. (Chan et al. 2008). However, graphite being soft generates lower elastic stresses during lithiation. While silicon did not perform well because of its high molar volume. Silicon expands by 4 times its volume on full lithiation leading to a severe effect on lithium diffusion during lithiation. Lithium titanate showed good performance amongst the anode material due to its higher yield strength and high capacity. When compared based on the ability to store charge silicon exceeded lithium titanate but its lower yield strength made it more prone to yielding than the later (X. H. Liu et al. 2012).

The charging index depended directly on the square of the yield strength of the material and inversely to the charge capacity and elastic modulus. Materials like lithium ferrous phosphate have a lower rating on this index, it is advisable to apply strengthening mechanism to improve the yield strength. Furthermore, lithium ferrous phosphate showed very poor characteristics on the elastic merit index scale because of its very high molar volume. This

meant that ferrous phosphate electrodes elastically deform more than lithium manganese oxide and lithium cobalt oxide electrodes. Newer materials could be work hardened and/or alloyed to improve their performance. This would allow materials to be charged quicker without failure. Furthermore, the stress developed in the particle came from the mass flux of lithium ions. From Equation 2.7, if the radius of the particle is reduced it would allow higher charging rates for same flux. This is a tradeoff between manufacturability to the mechanical performance of the electrode.

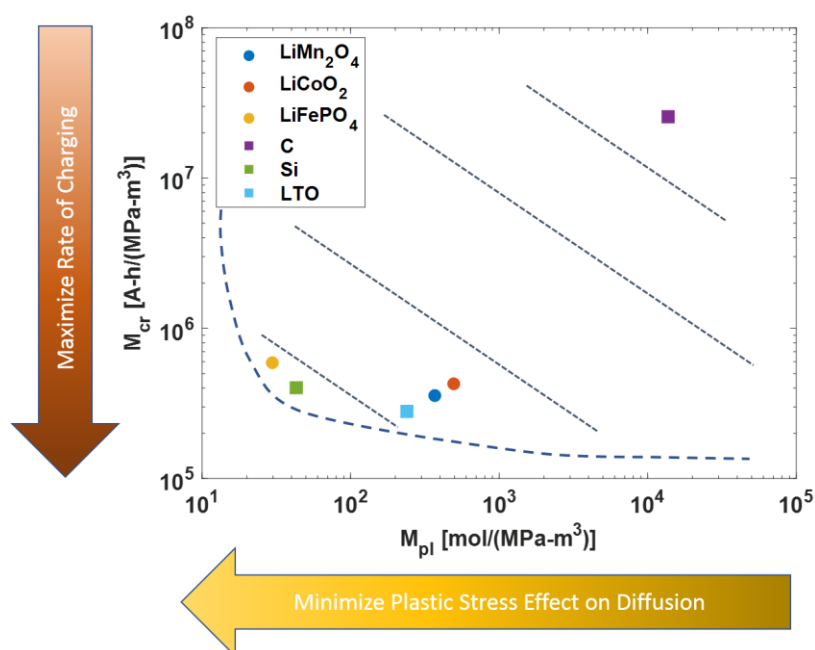


Figure 2.4 Material selection based on multivariable merit index comparison of charging rate index and plastic stress index.

With the increase in charging rates and search for better charging materials, only consideration of the elastic effects during lithiation is not a justified approximation. Faster charging increases the slope of the concentration profile in the electrode particle. This causes the equivalent stress of the particle to exceed the yield limits and deform plastically. Plastic mean stress also affects the diffusion process. However, the yield stress and molar volume reduce the concentration gradient and allowing free expansion of the particle. Therefore, it is useful to maximize this scale to understand which material can withstand the plastic

deformation. Figure 2.4 compared the materials by maximizing the merit index for charging while minimizing the plastic deformation effect on diffusion. Lithium ferrous phosphate electrode was found to be an excellent cathode material under this category. It has a high yield strength, making it more resilient during plastic deformation compared to lithium manganese oxide and lithium cobalt oxide. The merit index clearly stood out the performance of silicon for the anode. Silicon's ability to lithiate under plastic deformation has been observed experimentally (X. H. Liu et al. 2012), which validates the integrity of the plastic merit index. Graphite showed very poor plastic performance because of its low yield strength and brittle nature, making it vulnerable in the plastic deformation domain. Therefore, silicon is an excellent choice for HEV batteries which have very high capacities with the ability to operate under plastic deformation.

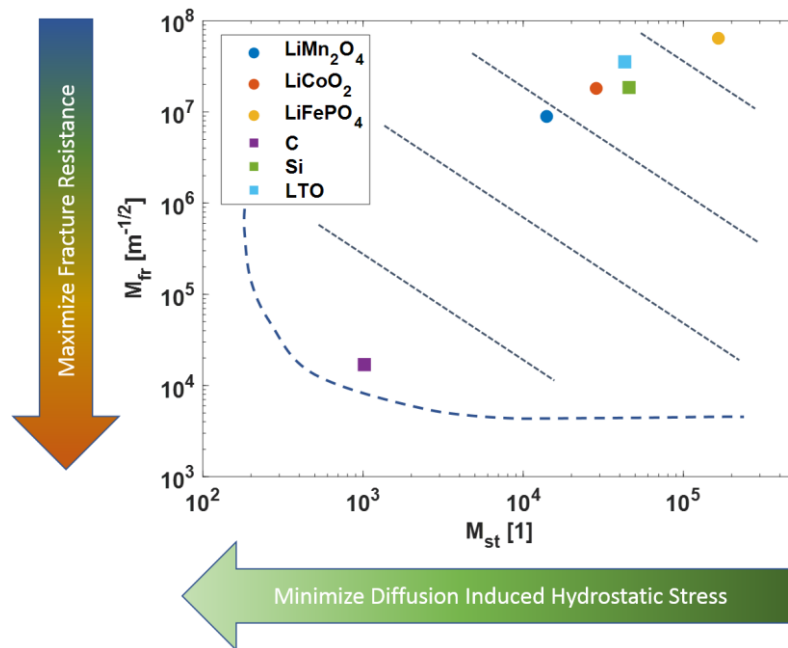


Figure 2.5 Material selection based on multivariable merit index comparison of fracture index and hydrostatic stress index.

The strength of the material was compared against the material toughness. Figure 2.5 shows a comparison between the diffusion induced hydrostatic stress-based index against the fracture resistance index for different electrode materials. It could be inferred that higher yield

strength means better mechanical performance, lower elastic modulus means a softer material which would generate less stress during deformation, while lower molar volume means smaller volumetric deformation during lithiation. Lithium manganese oxide showed the best mechanical performance among the cathode. The stress developed due to the concentration gradient, which is the prime source of stress for this analysis, was minimum for lithium manganese oxide and highest for lithium ferrous phosphate as a cathode. This was attributed due to the lower modulus of elasticity and molar volume of lithium manganese oxide, which could generate low stress and have high fracture toughness, making it more resilient to fracture. Among the anode, graphite showed the best characteristic. Silicon was comparably poor to graphite because of its low elastic modulus. However, silicon was comparable to other cathodic material making it the second-best candidate of choice under elastic loading. Silicon can store an order of magnitude more charge than graphite making this tradeoff favorable towards the former. To improve any new materials mechanical characteristics, it is important to reduce the molar volume and/or increase the yield strength.

Different chemo-mechanical processes can harden the material making it durable. Doping the electrode material with a chemical reagent is an excellent way to alter the molar volume of a material. By altering the stoichiometry, it is possible to reduce the distortion strains in the material causing it to expand less. Furthermore, to improve fracture characteristics, it is crucial to reduce the parameters affecting the stress and improve the toughness of the material. Silicon, for example, can be made tougher by coating it with a more resilient inert layer (like titanium oxide) to improve its fracture performance (Rong et al. 2013). The selection of material based on their mechanical performance and fracture stability is crucial for improving battery performance and life under higher charging rates. Higher mechanical stability is offered for materials with higher yield strength, which can be improved by toughening the material. Size of the electrode particle also plays a crucial role in determining its performance. The

current flux depends on the radius and rate of charging of the lithium battery. Smaller particles can be charged faster for the same stress generated. Moreover, smaller particles allow better diffusion, which leads to lower concentration gradient and consequently better mechanical stress characteristics. Silicon has a very high charge capacity which makes it a good choice for high charging systems where plastic deformation is dominant. However, its fracture characteristics need to be improved for a safer design.

2.4 Conclusions

The work developed an elasto-plastic based diffusion-induced stress model and a set of five material indices for material categorization and selection, based on the mechanical and fracture characteristics. The elastic-perfect plastic chemical diffusion model was solved to attain the concentration profile for lithium-ion in the elastic and plastic domain. The concentration was used to attain the stress profile for the electrode during lithiation. The comparison between the stress profile for lithium manganese oxide under 2C and 3C charging rates showed that the center of the particle was under a huge tensile hydrostatic loading during lithiation. The equivalent stress being zero prevents failure of the particle. However, the presence of voids would lead to failure by crack nucleation and propagation over multiple cycles. This would affect the capacity of the battery. The materials were evaluated based on their charge holding capability under elastic and plastic loading. It was found that under elastic loading conditions lithium manganese oxide and graphite were the best cathode and anode materials, while under plastic loading lithium ferrous phosphate and silicon were the best material choice for the battery. The strength of the electrode material was compared against its toughness, and lithium manganese oxide and graphite showed the best performance. From the material parameterization, it was inferred that lithium manganese oxide was the most suited cathode material due to its ability to perform well under faster charging and showing excellent mechanical and fracture characteristics. Graphite performed great in handling elastic stress and

was resistant to fracture, however newer material like silicon and lithium titanate was found to be good for faster charging and in handling plastic deformation. This made them good choices for HEV battery modules. Furthermore, newer materials could be made better by lowering the elastic modulus and molar volume and improving the yield strength by toughening. Fracture toughness could be improved by coating the material with a more resilient substance to absorb the fracture energy. Reducing particle size would be a great alternative, as it would allow higher rates of charging for same current flux and lower mechanical stresses. These indices have a great importance in classifying good electrode materials and aid in the search for newer battery materials.

CHAPTER 3. PARAMETRIC ANALYSIS OF ELECTRODE MATERIALS ON THERMAL PERFORMANCE OF LITHIUM-ION BATTERY: A MATERIAL SELECTION APPROACH

3.1 Introduction

Lithium-ion Batteries (LIBs) are the technologically leading source of energy storage for electronic device and in electric vehicle industry (Armand and Tarascon 2008). The lithium-ion transportation and storage are an exothermic process and battery failure due to overheating and melting of lithium-ion batteries is a primary concern in the battery industry. A large number of transition metal oxides have been tested for cathode materials of which lithium manganese oxide, lithium ferrous phosphate, and lithium cobalt oxide are the most widespread (“BU-205: Types of Lithium-Ion” 2017). For the anode, graphite is the material of preference for over a decade (X. Zhao et al. 2011). In recent years, silicon nanosphere and nanowire have shown good promise as an anode material because of their high-energy storage capacity (~4200mAh/g). This is due to the conversion of Si to $\text{Li}_{22}\text{Si}_5$ (Su et al. 2014), causing silicon to undergo an extensive plastic deformation during lithiation (~300% volumetrically) making them mechanically unstable to design. However, mixing small fractions of silicon with graphite electrodes has proved to improve the capacity of the anode significantly (J. Wang, Chen, and Qi 2011). Depending on the anode and cathode materials, mechanisms governing storage and diffusion of lithium may follow different pathways. For example, lithium manganese oxide electrode gets directly reduced during lithiation and the diffusion process is governed by the chemical potential across the electrodes (Doyle, Fuller, and Newman 1993). In case of lithium cobalt oxide electrodes, there is a phase change from alpha to beta structure during reduction of cobalt beyond a certain lithium ion concentration (Al Hallaj et al. 2000). This process is kinetically-driven, but the phase change affects the kinetics of the diffusion process. Newer cathode materials are being developed for obtaining stable high capacity batteries (Blomgren

2017). The current trend of research is focused on lithium-rich, manganese-rich/nickel-rich, layered-lithium nickel manganese cobalt electrodes (NMC), which have become popular due to their ability to maintain high capacity ($>250\text{mAh/g}$) at operating discharge potential (3.6V – 4.5V) (Xiang et al. 2014; Fell et al. 2013). Graphite electrodes intercalate with lithium through chemical mass transport without reaction. However, silicon reacts with lithium during the first cycle to convert from crystalline to amorphous state (F. Wang et al. 2013). This process is kinetically driven rather than being purely diffusive. Once the entire silicon particle gets lithiated to an amorphous structure, it behaves similar to graphite and allows diffusion dependent intercalation.

In a cell, the energy generated from the reaction (or ion transfer) between the cathode and the anode represents the work delivered by the cell. However, losses due to irreversibility and from other sources cause heat generation in the cell. Heat generation in lithium-ion batteries can be accounted for four dominant mechanisms which include polarization heating, entropic heating, resistive (joule) heating and heat generated during plastic deformation. Polarization heating is associated with the energy required for the current to transport over the potential barrier resulting from the accumulation of surface charges. Surface charge accumulation occurs when the applied potential in the electrolyte varies from the open circuit potential of the electrode particles. Entropic heating is due to the energy changes associated with entropic changes during insertion and removal of lithium ion into/from the electrode particle. For example, in a lithium manganese oxide electrode, the deformation of the tetrahedral structure of manganese oxide during lithium insertion causes the change in entropic states leading to heat generation. Resistive heating is due to the intrinsic resistance of different battery components like separator, electrodes, current collectors and electrolyte to the flow of ions through the cell during discharge/charge. With the advent of faster charging, the battery industries face the challenge of plastically deforming electrodes under heavy loading

conditions. When equivalent stress exceeds the yield criteria, a part of the plastic strain energy is dissipated in the form of heat. Heat generation due to plastic deformation may occur in the outer layer of an electrode particle. Other heating sources like reaction, phase change and heat due to mixing are negligible at room temperature and become dominant only at high temperatures for certain combination of electrodes leading to thermal runaway (B. Liu et al. 2017; Ren et al. 2017).

In this chapter, a multiscale thermal model that incorporates the different lithium intercalation mechanisms of the electrode particles was utilized to estimate the heat generation during charging and discharging cycles. Three dominant mechanisms were considered for heat generation during lithium diffusion and storage, i.e. polarization, entropic and joule heating. The heat generated from the plastic flow was also taken into account separately to analyze electrode performance under heavy loading conditions. Material properties-based merit index was derived for each heat generation mechanism in order to facilitate the comparison of the thermal performance of both existing and novel electrode materials. The multiscale model and material indices were tested on six candidate electrode materials. Finally, the model and indices were used to suggest critical material properties which affect the thermal generation and provide pathways to improve the thermal performance of newer high-capacity electrode materials.

3.2 Mathematical and Parametric Analysis

3.2.1 Thermal Model

Charging and discharging in a lithium battery occurs through the exchange of lithium ions between the electrodes. As the cell discharges the lithium ions diffuse from the anode into the cathode driven by the electrochemical potential difference between the electrodes. Lithium-ions dissociate from the anode and intercalate with the cathode to form a lithium intercalation compound during the discharge process and vice-versa during the charging cycle. Mass

transport in a spherical electrode particle was modeled using chemical potential-driven diffusion, as represented in Figure 3.1.

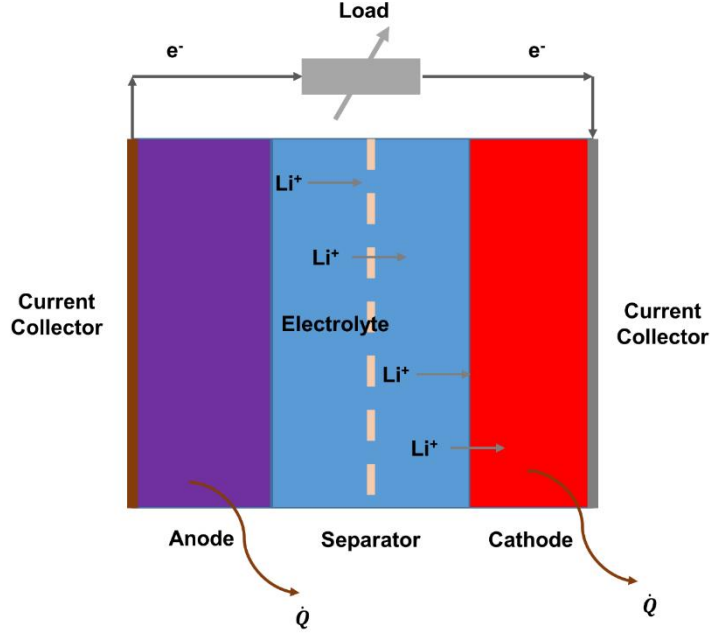
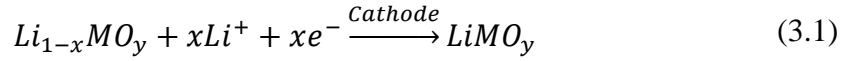


Figure 3.1 Schematic of lithium-ion battery during discharge cycle with heat generation.



The concentration of lithium-ion in the electrode was considered zero before lithiation. The porous electrode theory was assumed for this analysis. The model estimated the total heat generation per unit volume (\dot{q}) in the electrode based on four volumetric heat generation sources, i.e. polarization (\dot{Q}_p), entropic (\dot{Q}_e), joule (\dot{Q}_j), and a geometry dependent heating source from plastic deformation of the electrode particle (\dot{Q}_{plast}). The average heat generated was calculated by volume averaging all the heating sources.

$$\dot{q} = \frac{\dot{Q}_p + \dot{Q}_e + \dot{Q}_j + \dot{Q}_{plast}}{V_{par}} \quad (3.3)$$

Where, V_{par} is the particle volume. This microscale heat generation was applied to a macroscale diffusion equation considering all particles in the electrode layer generate the same average volumetric heat.

$$\rho c_p \frac{\partial T}{\partial t} = k_{th} \nabla^2 T + \dot{q} \quad (3.4)$$

Where, ρ is the material density, c_p is the specific heat capacity and k_{th} is the thermal conductivity of the electrode. Joule heating depends on the electrical resistivity (ρ_R) of the material. The electrolyte was assumed to be perfectly conducting, thereby having zero resistance. The joule heating was calculated based on Ohm's Law.

$$\dot{Q}_j = i^2 \rho_R V_{par} \quad (3.5)$$

Where, i is the current flux across the cell.

The other three heating sources require the concentration profile of lithium-ions in the electrode. To obtain the concentration profile in a spherical electrode particle, the lithium-ion transport was modeled using the diffusion equation:

$$\frac{\partial c}{\partial t} = D \left(\frac{\partial^2 c}{\partial r^2} + \frac{2}{r} \frac{\partial c}{\partial r} \right), \quad (3.6)$$

With boundary conditions corresponding to the constant applied current on the particle surface.

$$i = \frac{\alpha \rho r_0}{3} C_{rate} \quad (3.7)$$

$$J|_{r=r_0} = \frac{i}{F} \quad (3.8)$$

$$\frac{\partial c}{\partial r}|_{r=0} = 0 \quad (3.9)$$

Where, D is the mass diffusivity of the electrode material with respect to the lithium-ion and c is the concentration of lithium-ion diffused inside the particle. The current flux on the surface depends on the theoretical capacity of the electrode material (α), density (ρ), radius (r) and the rate of charging (C_{rate}). At the center of the spherical electrode particle, a symmetry

boundary condition was used to ensure continuity. The current was assumed constant during lithiation and dependent on the rate of charging. The concentration and radius were normalized, $\hat{c} = c/c_{\max}$ and $\hat{r} = r/r_0$.

The current and surface over-potential (η), were expressed as a function of the normalized concentration of lithium-ions, using the Butler-Volmer equation:

$$\frac{i}{F} = k_r c_l^{1-b} c_\theta^{1-b} c_s^b \left[\exp\left(\frac{(1-\alpha)F\eta}{RT}\right) - \exp\left(\frac{-\alpha F\eta}{RT}\right) \right] \quad (3.10)$$

$$\eta(\hat{c}) = [V_{app} - U_{OCP}(\hat{c})] \quad (3.11)$$

Where, c_l is the lithium-ion concentration in the electrolyte, c_s is the lithium-ion concentration on the electrode surface and c_θ is the lithium-ion concentration in vacant sites ready for intercalation ($c_l - c_s$). The rate of reaction for the given material is represented by k_r . The open circuit potential (U_{OCP}) is a material property of the electrode and function of lithium-ion concentration. The applied voltage (V_{app}) was calculated for a given material due to an applied current.

The Butler-Volmer reaction rate equation was used to calculate the overpotential and consequently the applied voltage for the battery, under a constant-current condition. The polarization-based heat generation was modeled based on the applied current and the calculated over-potential.

$$\dot{Q}_p = I_{app} \eta(\hat{c}) \quad (3.12)$$

$$I_{app} = i A_{par} \quad (3.13)$$

Where the applied current (I_{app}) is defined as the current flux (i) times the surface area of the particle (A_{par}).

The entropic heating was quantified based on the following formulation (Bernardi, Pawlikowski, and Newman 1985):

$$\dot{Q}_e = I_{app} T \left[\frac{\partial \bar{U}_{OCP}}{\partial T} (\hat{c}) \right] \quad (3.14)$$

Where the differential of U_{OCP} with respect to temperature (T) has been experimentally found to be a function of the lithium-ion concentration but can be approximated as a constant for most battery materials (Doyle, Fuller, and Newman 1993).

In the case of fast charging of the electrode material, the lithium-ion does not completely diffuse through the particle. This leads to a large concentration gradient across the particle. Since the radial and hoop stresses in the particle are dependent on this concentration gradient, the equivalent stress state grows with the concentration gradient. When the yield criteria is attained at the particle surface, the particle starts to flow plastically. As lithium-ion keeps diffusing into the particle, this plastic domain grows in thickness and forms a shell over the elastic regime. A part of this plastic strain energy is dissipated in the form of heat. A typical volume averaged plastic heat generation was modeled as follows:

$$\dot{Q}_{plast} = \beta S_y (\dot{\varepsilon}_r^p + 2\dot{\varepsilon}_\theta^p) = \beta \frac{S_y c_{max} \Omega r^3}{t} \int_{\hat{r}_p}^1 \hat{c} \hat{r}^2 d\hat{r} \quad (3.15)$$

Here, c_{max} is the maximum lithium-ion concentration in the electrode particle, $\dot{\varepsilon}^p$ is the plastic strain rate in radial (r) and hoop (θ) direction, Ω is the partial molar volume of the electrode material and S_y is the yield stress of the material. The integral term holds between the plastic radius (r_p) and total radius (r_o) at a given time (t) of lithiation. The conversion efficiency from plastic work to heat is β (Ravichandran et al. 2002). The plastic heat is generated only in a thin film of plastic deformation smeared over the elastic spherical domain. The plastic strain is produced purely from volumetric expansion since no external stress is applied to the particle (Huang, Suo, and Ma 2002).

3.2.2 Parametric Analysis

Different heat sources are dependent on material properties like electrode capacity, lithium-ion diffusivity, reaction rate, entropic capacity, internal resistivity, etc. as well as design/operating parameters like the diameter of the particle, charging rate and state of charge. Previous research reports (Christensen and Newman 2006b) have shown that the diffusion-based chemical transport may be used to describe lithium-ion transport in all electrode materials. Even though different electrode materials intercalate differently, and some undergo phase transformation while others react with lithium. Hence it is convenient to compare the candidate electrode materials based on heat generation and lithium-ion diffusion.

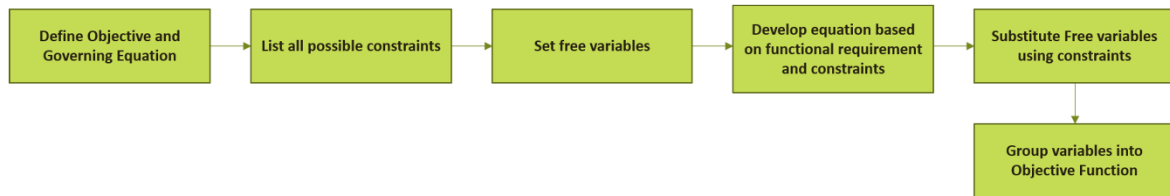


Figure 3.2 *Material index formation process representation.*

Figure 3.2 shows the process flow of the material index design based on Ashby's method for material selection (Ashby 2005). In order to facilitate comparison across different electrode materials, the heat generation was compared with the constraint that all electrode particles have the same state-of-charge (SOC) during lithiation. This constraint was imposed to create a datum for uniform lithiation in the following analysis. This meant that all electrode particles had the same lithium concentration.

$$\hat{c}(\hat{r}) = \frac{c}{c_{\max}} = \text{Constant} \quad (3.16)$$

Constraint for either the time of diffusion or the radius of the electrode was required to be the same for different electrode materials. Uniformity based on particle size is difficult to obtain from a manufacturing perspective. On the other hand, the commercial trend for battery

dictates faster charging, thus making a comparison based on constant diffusion time to charge the particle.

$$\hat{t} = \frac{tD}{r_o^2} = \text{Constant} \quad (3.17)$$

Considering the total time required for diffusion (t) is constant, the following proportionality was used.

$$r_o \propto \sqrt{D} \quad (3.18)$$

Table 3.1 provides the data for six selected electrode materials that are popularly studied in lithium-ion batteries.

3.3 Results and Discussion

The thermo-chemical model was developed for a generalized material candidate for lithium-ion battery electrodes. Six different materials were selected as candidates for based on their heat generation ability and thermal performance. The materials were lithiated by ignoring any phase transformation during lithiation process. The energy released as the heat was estimated for half-cell electrodes based upon the established constraints (Equation 3.16-3.18). All calculations were performed on MatLab platform (MATLAB 2017). The temperature for the following calculations was maintained at 298K. The lithium-ion of the electrolyte (c_l) was taken as 1000 mol/m³ and the SOC (\hat{c}) was considered 50%. The particle was lithiated for a C_{rate} of 1, for all materials. The plastic deformation energy to heat conversion factor (β) is an experimentally determined quantity and is dependent on material microstructure and strain rate. It was taken to be 0.75 considering $\beta \in (0.45 - 0.95)$ (Ravichandran et al. 2002).

Table 3.1 Material properties for thermal analysis three cathode and anode materials used in lithium-ion batteries.

Properties	LiMn ₂ O ₄	LiCoO ₂	LiFePO ₄	LiC ₆	Li ₂₂ Si ₅	Li ₂ TiO ₃
D (m ² /s ⁻)	7.08×10 ⁻¹⁵ (Christensen and Newman 2006b)	1.00×10 ⁻¹³ (Renganathan et al. 2010)	7.96×10 ⁻¹⁶ (Satyavani et al. 2016)	3.90×10 ⁻¹⁴ (Renganathan et al. 2010)	1.00×10 ⁻¹⁶ (Ma et al. 2015)	6.8×10 ⁻¹⁵
ρ (kg/m ³)	4100 (Christensen and Newman 2006b)	5030 (Renganathan et al. 2010)	3600 (Y. Zhu and Wang 2010)	2100 (Renganathan et al. 2010)	2240 (Dash and Pannala 2016)	3430 (“Lithium Titanate” 2017)
α_{th} (mAh/g)	148 (Julien et al. 2014)	166 (Julien et al. 2014)	170 (Julien et al. 2014)	372 (Julien et al. 2014)	4200 (Julien et al. 2014)	175 (Kam and Doeff 2012)
c_{max} (mol/m ³)	2.29×10 ⁴ (Christensen and Newman 2006b)	4.99×10 ⁴ (Renganathan et al. 2010)	2.12×10 ⁴	3.05×10 ⁴ (Renganathan et al. 2010)	8.87×10 ⁴ (K. Zhao et al. 2011)	5.00×10 ⁴ (M. Chen et al. 2015)
k_r (m ^{5/2} /mol-m ³)	1.90×10 ⁻⁹ (D. Zhang, Popov, and White 2000)	5.18×10 ⁻⁹	3.12×10 ⁻¹² (Hellwig, Sörgel, and Bessler 2011)	5.03×10 ⁻¹¹ (Takahashi and Srinivasan 2015)	5.00×10 ⁻¹⁰	5.00×10 ⁻¹³ (C. H. Chen and Amine 2001)
$\frac{d\bar{U}_{OCP}}{dT}$ (mV/K)	0.50 (Bach et al. 1992)	0.25 (Al Hallaj et al. 2000)	0.30 (Bazinski and Wang 2014)	0.14 (Al Hallaj et al. 2000)	0.50 (Maher and Yazami 2013)	0.10 (M. Chen et al. 2015)
ρ_R (Ω -m)	81.00 (Hoang 2014)	1.00×10 ⁴ (Rao and Smakula 1965)	1.00×10 ⁷ (B. Wu, Ren, and Li 2011)	6.00×10 ⁻⁴ (Giancoli 2008)	60.00	0.10 (Ogihara 2012)
k_{th} (W/m-K)	0.80 (Gotcu and Seifert 2016)	0.32 (Gotcu and Seifert 2016)	2.70 (X.-H. Yang, Tan, and Liu 2016)	80.00	4.50 (W. Xu, Zhang, and Li 2015)	1.04 (M. Chen et al. 2015)
S_Y (MPa)	776 (Kushima, Huang, and Li 2012)	1056 (Kushima, Huang, and Li 2012)	500 (Kushima, Huang, and Li 2012)	23 (Kushima, Huang, and Li 2012)	720 (Kushima, Huang, and Li 2012)	836

In the following analysis, the heat generation from all four mechanisms was compared. The objective of the analysis was to find the minimum merit index (M) value among the cathode and anode materials for each heat generation mode.

3.3.1 Entropic Index

The second heat generation source considered was due to entropic changes in the electrode material.

$$Q_e \propto A_4(\rho\alpha_{th}\sqrt{D})\frac{\partial\bar{U}_{OCP}}{\partial T}D \quad (3.19)$$

The entropic heating was minimized in this merit index (M_e).

$$M_e = (\rho\alpha_{th})\frac{\partial\bar{U}_{OCP}}{\partial T}D^{\frac{3}{2}} \quad (3.20)$$

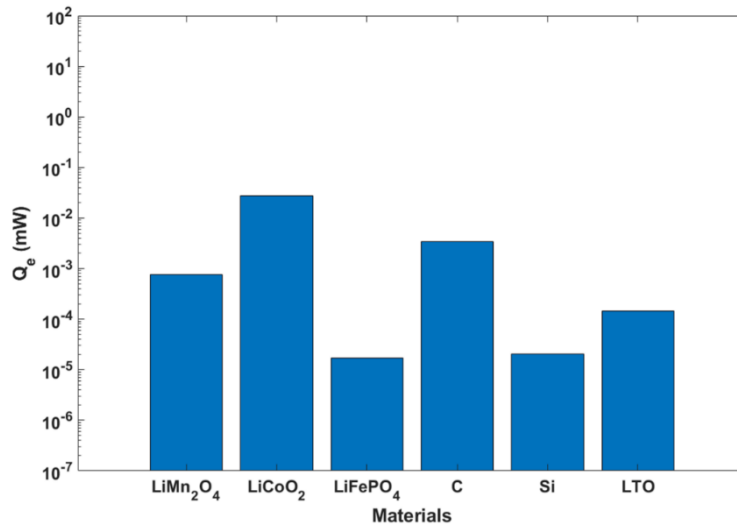


Figure 3.3 Heat generation and material selection based on entropic heating mechanism at 1C rate of charging.

Entropic heating in a battery occurs due to the entropic changes in the material when it gets lithiated. As the material reacts with lithium-ions, its bond structure is altered to accommodate the insertion of the ions. The change in the bond energy and resulting changes in the overall dipole of the material cause energy generation (or absorption) during lithiation/delithiation. Entropic heating and the change of open circuit potential with the variation of temperature are of major importance as they contribute to heat generation in the

electrode. It was observed from the thermal generation comparison in Figure 3.3 that amongst the cathode materials, lithium ferrous phosphate had the lowest entropic heating tendency while lithium cobalt oxide produced the highest heat. The experiments by Viswanathan et al (2010) (Viswanathan et al. 2010) observed that lithium cobalt oxide electrodes have a very large entropic change contributing to high heat generation during charging. This index depends on three parameters (based on Equation 3.14), i.e. density, diffusion coefficient and entropic potential. The product of the current and entropic potential results in the change in the thermodynamic entropy ($\Delta S = I \frac{d\bar{U}_{OCP}}{dT}$) of the electrode particle. Although lithium cobalt oxide has a slightly lower entropic potential than lithium ferrous phosphate (Table 3.1), the total entropy change in lithium ferrous phosphate was found lower than lithium cobalt oxide. Lithium titanate showed better entropic behavior compared to graphite during lithiation, counterintuitive to graphite having higher entropic potential and current characteristics than lithium titanate. Thereby the later has lower entropic heating potential. Silicon showed very low entropic heat generation potential compared to other anodic materials, making it an excellent choice for anode material. Since entropic heating is dominant at low charging rates, it is important to find solutions to mitigate the entropy generation in the electrode materials. A suggested option would be to dope the electrode materials with some relaxant chemicals like MgO, Al₂O₃, etc. (C. Li et al. 2006).

3.3.2 Polarization Index

The polarization heating in lithium-ion electrodes is due to the difference between applied voltage and open circuit potential when current flows through the electrode. From Equations 3.10 and 3.11 the overpotential was derived.

$$\eta = \frac{RT}{\alpha F} \operatorname{asinh} \left(\frac{i}{F k c_{\max} c_l^{1-\alpha} \hat{c}^\alpha \hat{c}^{1-\alpha}} \right) \quad (3.21)$$

$$\eta = A_1 a \sinh \left(\frac{A_2 \rho \alpha_{th} \sqrt{D} t_0}{k c_{max}} \right) \quad (3.22)$$

Where, A_1 and A_2 are constants. The current flux (i) was replaced by Equation 3.8. Equations 3.8 and 3.20 were substituted into polarization heat generation in Equation 3.12. The diffusion time constant (t_0) was assumed to be one.

$$Q_p \propto A_3 (\rho \alpha_{th} \sqrt{D}) a \sinh \left(\frac{A_2 \rho \alpha_{th} t_0 \sqrt{D}}{k c_{max}} \right) D \quad (3.23)$$

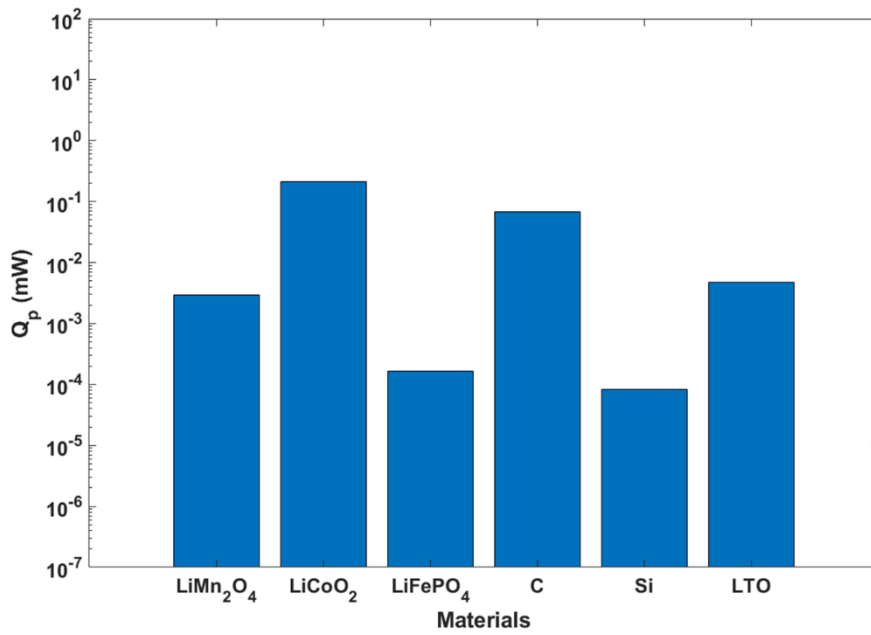


Figure 3.4 Heat generation and material selection based on polarization heating mechanism at 1C rate of charging.

The simulation was performed to estimate the heat generation due to electrode surface charge deposition with the objective to reduce the heat from this overpotential created during lithiation of the electrode particle. The comparison between the cathode materials showed that lithium ferrous phosphate had the lowest polarization heating. Figure 3.4 shows that lithium cobalt oxide electrodes generated three orders of magnitude more heat due to polarization than other comparable materials. In order to determine a merit index, the constant A_2 in Equation 3.23 was ignored as it had minimum variation across the different electrode materials. Here, the merit index (M_p) was created based on the minimization of the polarization heating.

$$M_p = (\rho\alpha_{th})a \sinh\left(\frac{\rho\alpha_{th}t_0\sqrt{D}}{kc_{\max}}\right) D^{\frac{3}{2}} \quad (3.24)$$

Based on the mathematical formulation of polarization heating (Equation 3.12) and merit index (Equation 3.24), we found two primary properties that govern the polarization heating, i.e. density and mass diffusivity. A dense electrode material has a higher ability to store charge for the same capacity. This leads to a higher current absorption ability which is a primary cause of heating in batteries. Moreover, higher mass diffusivity can be related to larger particle radius, under the constraint of uniform diffusion time. Larger particles tend to generate more heat which also adds up to the increase in lithium-ion absorption during lithiation. From the data in Table 3.1, lithium cobalt oxide was found to have high density and low capacity amongst the cathode materials which justifies its high polarization heating tendency, while lithium ferrous phosphate and silicon were found to generate the lowest heat as cathode and anode materials respectively, closely followed by lithium titanate. The low mass diffusivity of lithium ferrous oxide indicated that its particle size should be small for same diffusion time as other electrode materials. Amorphous silicon has significantly low diffusion coefficient compared to others and thus generates very low polarization heat. For high heat generating materials like lithium cobalt oxide, we conclude that maintaining lower particle diameter will reduce the heating tendency. This may be challenging due to manufacturing difficulties, but a trade-off is essential to attain better thermal performance.

3.3.3 Joule Index

The resistivity of the electrode material is a material property. The joule heating is proportional to the resistivity (ρ_R) of the material and the square power of the charging rate.

$$Q_j \propto A_5 (\rho\alpha_{th}\sqrt{D})^2 \rho_R D^{\frac{3}{2}} \quad (3.25)$$

Figure 3.5 shows the simulated heat generation to compare cathode and anode materials based on their joule heating. This resistance is proportional to the electromotive force within

the battery. The internal resistance occurs due to the resistance which the lithium ions face from the electrolyte and electrode during charging and discharging. The merit index for joule heating (M_j) was optimized based on minimization of the heat generation.

$$M_j = (\rho\alpha_{th})^2 \rho_R D^{\frac{5}{2}} \quad (3.26)$$

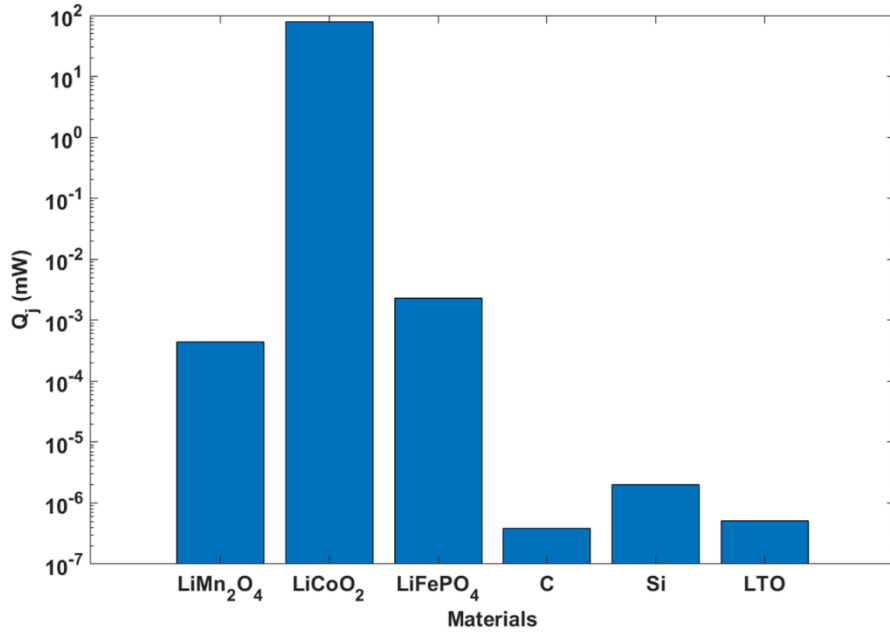


Figure 3.5 Heat Generation and Material Selection based on Joule Heating Mechanism at 1C rate of charging.

From Figure 3.5, it was observed that lithium cobalt oxide generated the highest heat because of its higher theoretical capacity and resistivity (Table 3.1). Among the cathode materials, lithium manganese oxide had the least resistive heat generation due to its superior conducting nature amongst other cathode materials. While graphite had the least resistance among the anode materials and therefore it was found a good choice as a low joule heating material. The high joule heat generation by lithium cobalt oxide in Figure 3.5, has been observed experimentally (Sato 2001).

3.3.4 Plastic Heat Index

The plastic heating was not considered to be a direct contributor to the total heat generation since it is dependent on the plastic yielding of the material.

$$Q_{plast} \propto A_6 S_y c_{max} \Omega D^{\frac{3}{2}} \quad (3.27)$$

Higher loading conditions and faster charging requirements put a great deal of stress on the electrodes. Most of the electrodes, except silicon, have a semi-brittle nature. These materials expand plastically under limited strain condition (or have very high yield limit). The plastic deformability of lithium manganese oxide has been experimentally observed by Kosova et al. (Kosova et al. 2000) and Schilcher et al. (Schilcher, Meyer, and Kwade 2016), while silicon's ability to lithiate under plastic deformation has been observed experimentally (X. H. Liu et al. 2012). The merit index for the plastic heat generation (M_{plas}) was minimized for better thermal performance.

$$M_{plas} = S_y c_{max} \Omega D^{\frac{3}{2}} \quad (3.28)$$

Silicon in the amorphous lithiated state behaves like a polymer and deforms plastically to four times of its initial state. Due to the unavailability of β -factor for the electrode materials, it was approximated to be 0.75, i.e. 75% of the plastic work was converted to thermal output. The analysis yielded silicon to be an excellent anode material while lithium ferrous phosphate to be a good cathode material in terms of thermal stability under plastic loading. This analysis however ignored the integral term in Equation 3.15, which represents the volumetric distribution of heat in the plastic shell. In case of polymeric materials like amorphous silicon, the particle would be fully plastically deformed, unlike graphite. This would impact the overall plastic heat generation.

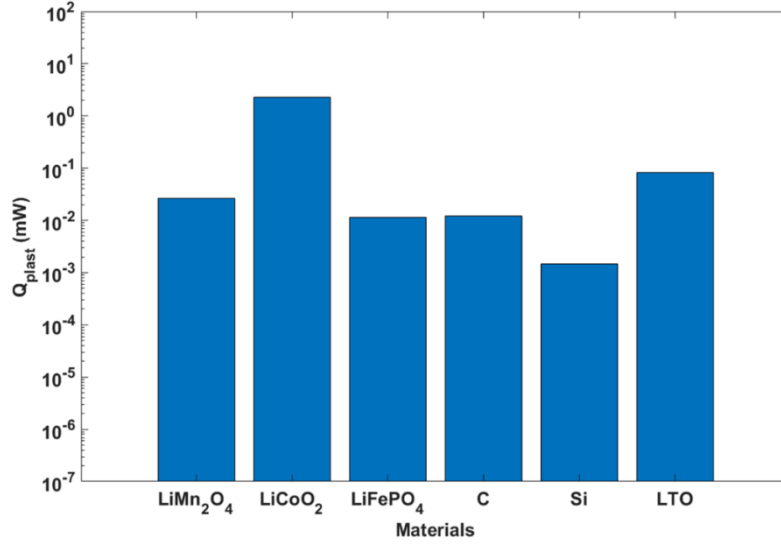


Figure 3.6 Heat generation and material Selection based on plastic heating mechanism at 1C rate of charging.

3.3.5 Thermal Diffusion Index

Thermal diffusion ability is important for studying the thermal performance of electrode materials. A good electrode material should not only be able to generate less heat but also be able to dissipate heat rapidly. Normalizing Equation 3.4 we get,

$$\frac{\partial \theta}{\partial \hat{t}} = \frac{1}{\hat{r}^2} \frac{\partial}{\partial \hat{r}} \left(\hat{r}^2 \frac{\partial \theta}{\partial \hat{r}} \right) + \frac{\dot{q} r^2}{k_{th} \theta_{\max}} \quad (3.29)$$

Considering all particles generated the same amount of heat and replacing the free variable, r , the normalized heat generation term was minimized for lower temperature variation.

$$M_d = \frac{D}{k_{th}} \quad (3.30)$$

It is essential that thermal diffusion of heat generated by the electrode material during charging /discharging cycles needs to be efficient for the better thermal performance of the battery. With the present analysis, the material should not only be able to generate less heat but also diffuse heat efficiently to the environment.

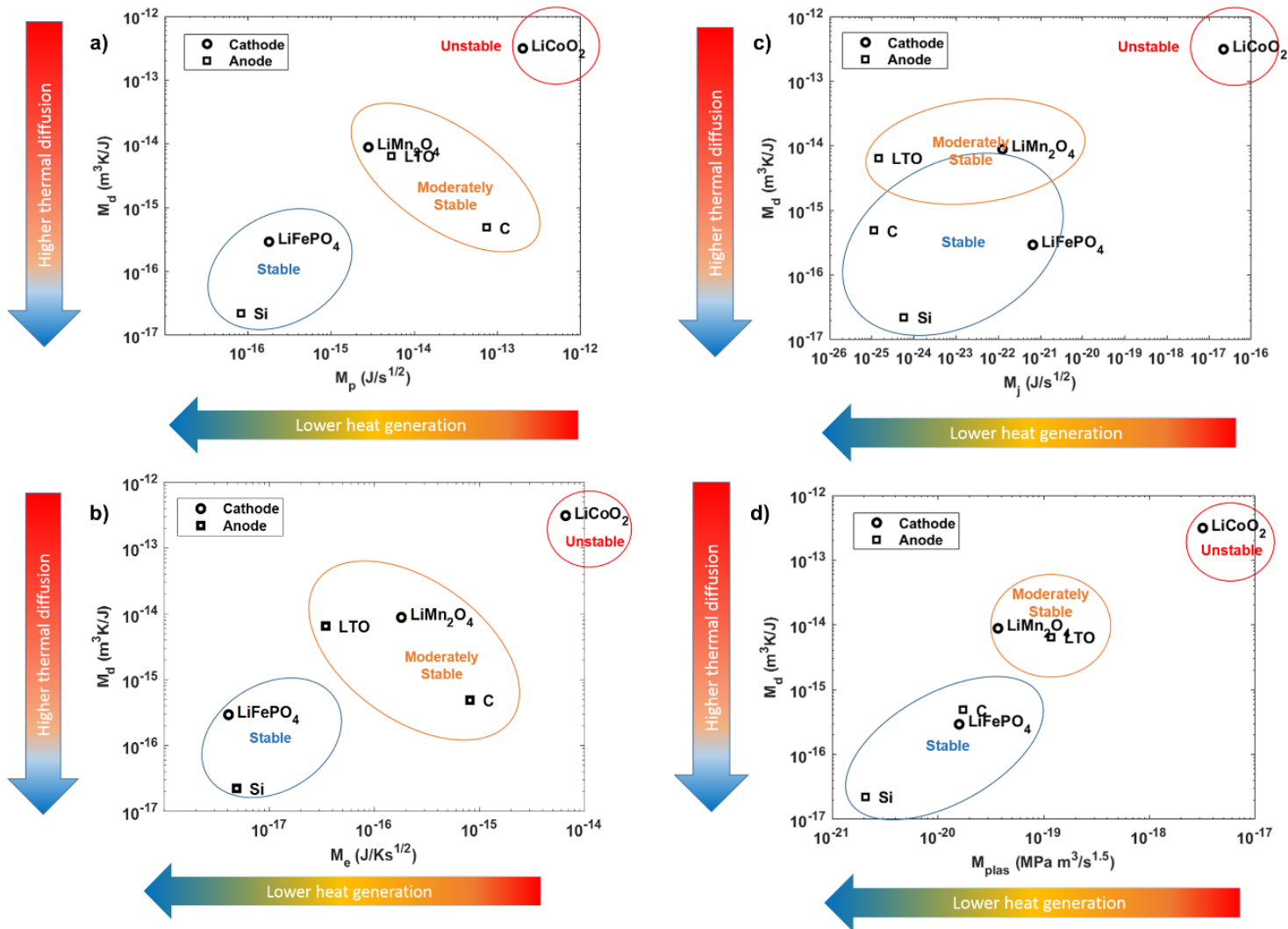


Figure 3.7 Merit index analysis to compare thermal generation based on four mechanisms against thermal diffusion characteristics of electrode material, a) Polarization, b) Entropic, c) Joule, and d) Plastic.

The equivalent thermal conductivity for the electrode with the binder and the conductive filler was considered. In Figure 3.7, the merit indices for the four modes of heat generation were compared against the merit index for thermal diffusion. The lower left corner of the plots represents low heat generation according to the individual mechanism (x-axis) and higher thermal diffusion characteristics (y-axis). This is the domain of thermal stability. The upper right corner is the domain of thermal instability due to high heat generation and lower heat diffusion. Amongst the cathode material, lithium cobalt oxide was found in the unstable domain while lithium ferrous phosphate was found to be the most stable. This meant that cobalt oxide batteries have the potential to generate more heat during lithiation/delithiation and diffuse heat poorly, compared to other cathode materials. The results were validated from the experiments conducted by Joachin et al (2009) (Joachin et al. 2009). According to their paper, lithium ferrous phosphate electrodes have a higher thermal stability at higher temperatures as compared to other oxide electrodes. Further validation was inferred from the experimental work by Viswanathan et al (2010) (Viswanathan et al. 2010) predicting a very large entropic change contributing to high heat generation conditions during charging for lithium cobalt oxide electrode. Yuan et al and Park et al (Yuan et al. 2011; Park et al. 2011) have experimentally established that olivine lithium ferrous phosphate electrodes have a longer lifespan and higher thermal stability compared to lithium cobalt oxide and lithium manganese oxide electrodes. Among the anode materials, Figure 3.7 showed that graphite generated the most heat (except the joule component) amongst all other anode materials. But graphite being an excellent thermal conductor dissipates the heat very effectively. In Figure 3.7(c), graphite generated the least heat due to its high electrical conductivity. It was found that silicon had the least thermal contribution with the best thermal diffusion characteristic in all heating mechanisms except the joule heating. It was closely followed by lithium titanium oxide. This was

validated against Viswanathan et al (2010) (Viswanathan et al. 2010), which compared graphite with lithium titanate and established the better thermal performance of lithium titanate over graphite electrodes. Silicon nanoparticle being smaller in volume than other anode materials is also able to dissipate heat faster, even though silicon has a poor thermal conductivity.

3.3.6 Effect of charging rate on heat generation in lithium battery electrodes

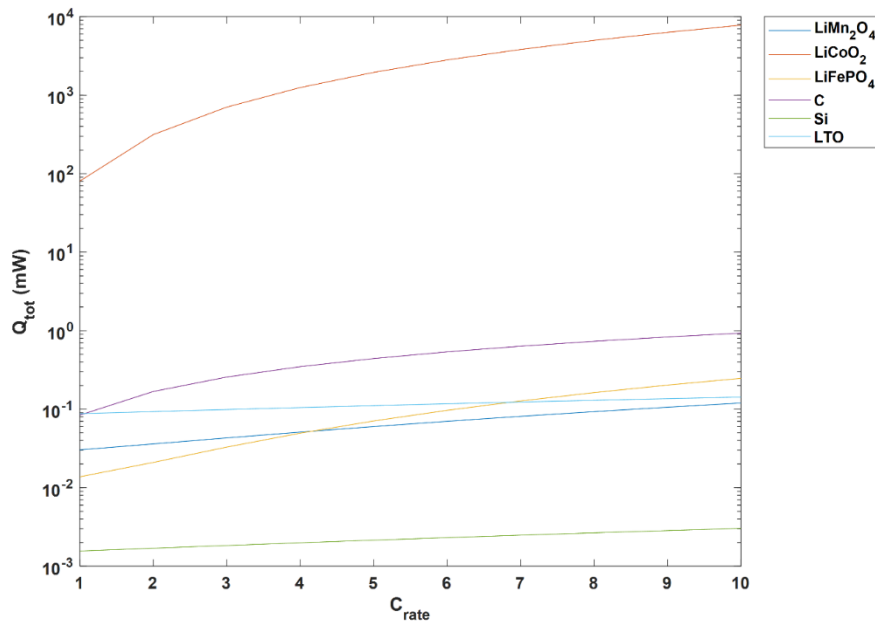


Figure 3.8 Total heat generation vs rate of charging for different electrode materials.

With the trend for exploration of stable electrode materials for faster charging applications, a parametric analysis was performed to compare the total heat generation from all thermal mechanisms for different electrode materials over a range of charging rates. Figure 3.8 shows the total heat generated for different electrode materials operated between 1C and 10C rates of charging. The analysis of the cathode materials showed that for low rates of charging ($C_{rate} < 4$), lithium ferrous phosphate generated the least heat. However, with an increase of the rate of charging, the joule heating component of ferrous phosphate electrodes became dominant due to its dependence on the square power of the current and poor electrical conductivity. Beyond C_{rate} of 4,

lithium manganese oxide was a better choice of the cathode material. Better discharge capabilities of lithium manganese oxide electrodes at faster charging have been established experimentally (Park et al. 2011). Lithium cobalt oxide always generated high thermal output, making it unsuitable for faster-charging applications. Among the anode, silicon was the best choice as observed from Figure 3.8, with respect to its lowest heat generation.

The simulated thermal prediction and merit index analysis based on polarization, entropic, joule and plastic heating characteristically showed that among the selected cathode electrode materials, lithium ferrous phosphate was found to be the best cathode material. In contrast, lithium cobalt oxide had the highest potential for thermal instability. The high heating problem in lithium cobalt oxide could be mitigated by manufacturing smaller sized cobalt oxide particles. This would reduce the current of the particle without affecting the capacity. Similarly, silicon was found to be the best choice among the candidate anode materials. It has excellent thermal diffusion ability and low thermal generation with high capacity. The only drawback for silicon is its tendency to plastically deform when it reacts with lithium and generate heat of reaction during the first cycle. So, pre-testing of first cycle survival for Si anode particles would be recommended.

3.4 Conclusions

The work demonstrated an innovative method to parametrize and compare electrode materials in a lithium-ion battery for thermal performance and stability. The paper was based on the development of a heat generation model from a chemo-mechanical diffusion model. Four mechanisms of heat transfer were considered, i.e. polarization heat, entropic heat, joule heat and heat contribution from plastic deformation, to get the net heat generation. Six different materials were selected, three for each cathode and anode, and for analyzing using the multiphysics model. Five merit indices were created of which four were used to compare the materials based on their

heat generation and their thermal diffusion characteristics. The results clearly established that amongst the candidate cathode materials, lithium ferrous phosphate was the best candidate having minimum heat generation among all four mechanisms and best diffusive performance from the fifth index. Silicon was the best anodic counterpart, showing least heat generation and best thermal stability. These materials could be considered as excellent candidates for high speed charging systems. However, materials like lithium cobalt oxide (cathode) and graphite (anode), which are the most commonly used electrode materials for lithium-ion batteries, had the poorest thermal performance. They generate huge amounts of heat by all the thermal mechanisms and have very poor thermal diffusive ability. It was also observed that with increasing charging rates, the joule heating component of the lithium ferrous phosphate made it generate more heat than lithium manganese oxide. It was inferred that for faster charging applications lithium manganese oxide and silicon are better choices of materials with respect to the thermal stability of lithium-ion battery. To mitigate the problem of high heat generation, it is advisable to reduce the particle size. Another solution is to dope the materials with some relaxing reagent to reduce the bond strain resulted from deformation during lithiation, thereby lowering the entropy generated in the process. Particle size optimization and chemical structure modifications seem to be few plausible options for improving materials having poor thermal properties. The search for newer materials would be greatly aided by the use of these material indices, as they provide a basis for comparison of the thermal performance with existing electrode materials.

CHAPTER 4. MODELING AND PROGNOSTICS OF SEPARATOR MELTDOWN FOR LITHIUM-ION POUCH CELLS UNDER COMPRESSION: BASED ON OPEN-CELL FOAM MODEL

4.1 Introduction

Lithium-ion batteries provide a low-cost, long cycle-life and high-energy density solution to the expediting energy requirement of the electronic and automotive industry (Armand and Tarascon 2008). Recent advancements in energy storage technologies require bendable lithium-ion cells which can support flexible electronics. Flexible lithium cells need to be foldable, stretchable and light-weight without losing their performance and stability (W. Liu et al. 2017). A flexible battery needs viable electrodes, better packaging, good-quality separator membrane and advanced cell assembly. Flexing of lithium cells would produce tensile and compressive stressed on the separator membrane leading to poor contact between electrodes and a rise in the internal resistance of the cell. It is therefore utmost important to have an excellent electrode-electrolyte interface under loaded conditions.

Flexible lithium-ion cells would be of great advantage when used as structural units installed within the body of hybrid vehicles. The application of such battery units would require the cells to have a low self-discharge, high capacity, stable cycling performance, and high rate capability (Tao, Lu, and Chen 2018). A key aspect in design of such lithium cells would be the issue to separator failure due to rupture or meltdown under loaded conditions. Under the condition of thermal runaway, the electrode material starts to disintegrate by reacting with the electrolyte (Hatchard et al. 2001). The process emits a lot of gases thereby needing the arrangement of a good venting mechanism in the battery (Michalak et al. 2015). The emissions would further increase the applied pressure on the separator membrane. Therefore, the separator membranes would need to

have high ionic-conductivity, good mechanical strength and flexibility, and high electrochemical stability (Wang and Wallace 2015). The separator in lithium-ion cells have been modeled and experimentally fitted as a viscoelastic material showing creep characteristics (W. Wu et al. 2014; Sheidaei et al. 2011; Cannarella and Arnold 2014). An excellent review article by Arora and Zhang (Arora and Zhang 2004), provide a detailed insight of different types of battery separators, their electrochemical behavior and applications. Mechanical models have been developed to capture the combination of viscoelastic behavior of the polymer skeleton and poro-elastic behavior caused by the flow of the fluid through the membrane pores. Poro-elastic characteristic causes effective stiffening of the separator under incremental strain rate (Gor et al. 2014). Several electrochemical-mechanical-thermal experiments, and analytical and FEM models for lithium-ion cells under tensile, compression and bending loads have been developed predicting the battery stability and life (Breitfuss et al. 2013; Lai, Ali, and Pan 2014). Several punch-indentation tests and models have been performed to obtain the desired mechanical properties for the separator membrane and predict the condition of battery short due to separator puncture (Lai, Ali, and Pan 2014; Kermani and Sahraei 2017; Sahraei, Meier, and Wierzbicki 2014; Sahraei et al. 2015).

Experimental investigations by Peabody and Arnold (Peabody and Arnold 2011) provide data for the effect of stress on ionic-conductivity of separator membrane. The proposed model in the current investigation suggests the separator membrane behavior similar to an open-cell foam structure. One of the earliest mathematical framework suggested to model open-cell foams was pioneered by Lakes et al (Lakes, Rosakis, and Ruina 1993) and Gioia et al (Gioia, Wang, and Cuitiño 2001), in which the energetics foam was modeled as a stack of tetrahedral structures which collapse upon application of compressive load. These models have been the basis of several works

on the mechanical characterization of open-cell structures (Deshpande and Fleck 2000; J. Zhang et al. 1998; H. X. Zhu, Mills, and Knott 1997; Gong, Kyriakides, and Jang 2005).

Three broad applications justifying the need for a compressive loading chemo-thermal model of the separator's mechanical and pouch cell's thermal behavior could be established. The first concept is the application of the pouch cell as an integrable structural unit in EV and HEV. The design and installation of pouch cells as a part of the vehicles body would allow reduced battery unit weight due to reduced number of casing components required in the installation. A more integrated and robust vehicle design could be proposed with the battery distributed throughout the vehicle depending on the locations of power requirement (like motor drive, automatic doors/windows, air-conditioning system, etc.). The separator model could be applied for flexible lithium-ion battery design where the application of the battery technology could vary from flexible wearable electronics to integrable biomedical devices (Pu et al. 2015; B. Liu et al. 2012).

The most imminent application of the thermal prognostics of lithium pouch cell under compressive load would be to address the effect of gaseous emissions in lithium battery, especially under the condition of thermal runaway and battery failure. At elevated temperatures, the electrode and electrolyte react kinetically to produce gaseous emissions causing the cell to swell (Coman et al. 2017; Coman, Rayman, and White 2016; Seo et al. 2010). Swelling of the pouch cell would apply pressure on the separator, causing a collapse of the pores leading to lower lithium conductivity and higher thermal generation. Increased temperature due to high joule heating would further aid the production of gas in the pouch cell thereby creating an unstable forward feedback loop leading to thermal runaway. Furthermore, gas emissions include CO_2 , C_2H_4 , C_2H_6 , CH_4 and

CO (Teng et al. 2015). Most of the emissions are highly flammable and could lead to explosive failure of the battery.

In the current work, an open-cell foam permeability model (Dawson, Germaine, and Gibson 2007) was utilized to model the variation of ionic-conductivity of separator membrane under uniform compressive loading. The model predictions were validated against the experimental data from Peabody and Arnold (Peabody and Arnold 2011). A chemo-thermal model was developed to simulate three different lithium-ion pouch cells (LCO/C, LMO/C and LFP/C) in combination with five separator materials (monolayer polypropylene, monolayer polyethylene, trilayer, nonwoven and ceramic-coated). The thermal performance of all these cells were simulated over a range of rates of charging, applied load and convective-cooling conditions, and thermal contour maps were created to predict the conditions leading to thermal meltdown of separator membrane. The overall implication of the proposed work was to create a design guideline for engineering of pouch-cells for application as structural units under loaded condition. The model could be further modified to consider the effects of gaseous emissions from electrode decomposition under high temperatures. An increase in the cell pressure would cause a lowering of separator conductivity and more heat generation, thus creating an unstable feedback leading to thermal runaway.

4.2 Mathematical Model

The lithium-ion cell was modeled based on a porous electrode, single particle model (SPM) under conditions of applied load (Fig. 4.1.a). A pouch cell type battery is considered for this analysis in which layers of electrodes and separator are under uniform compressive loading. The following analysis is divided into two segments. The first step was to model the separator material under load. The ionic conductivity of lithium-ion transport is predicted as a function of stress. Five

different types of separator membranes were considered in this analysis. In the following step, the thermal profiling of the pouch cell was performed under different applied load, charging conditions and convection boundary condition. The average cell temperature was simulated based on the solution of the thermal diffusion equation with three different modes of heat generation, i.e. polarization, entropic and resistive heating (Bernardi, Pawlikowski, and Newman 1985).

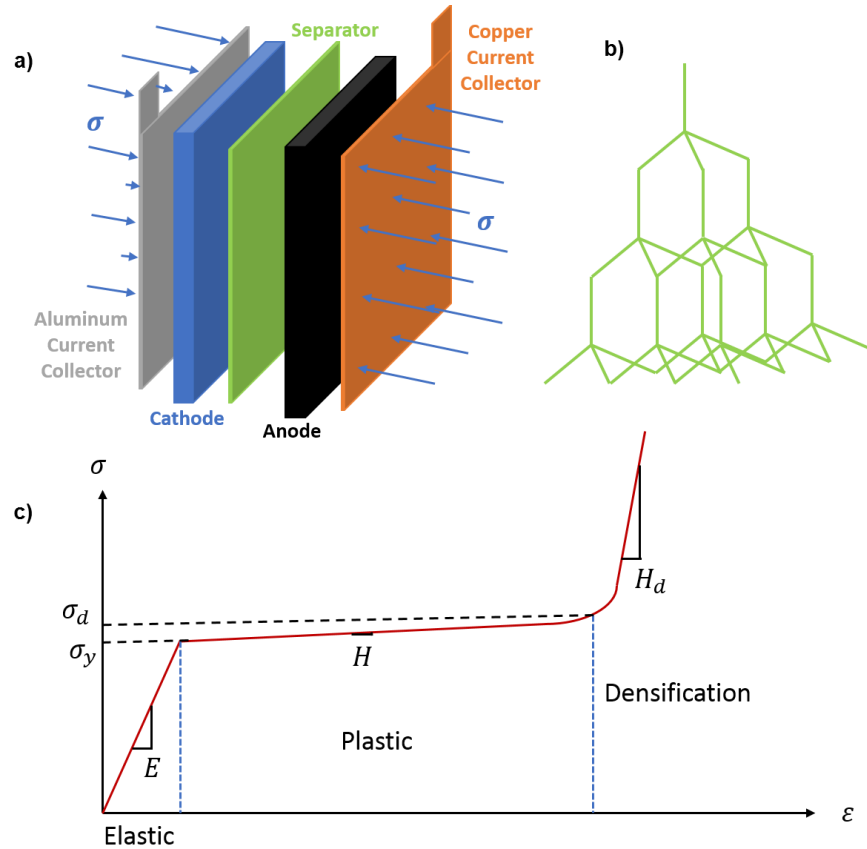


Figure 4.1 a) Schematic of lithium pouch cell under compressive load, b) Open-cell foam structure for separator model, c) Stress-strain schematic demarcating domains of elastic, plastic and densification characteristics for a foam-based separator.

4.2.1 Conductivity-stress analysis for a foam-based separator model:

The separator membrane was modelled as an open-celled foam structure (Fig 4.1.b). The foam could be assumed as a structure of tetrahedral arrangement of beams linked by rotary joints (Gioia, Wang, and Cuitiño 2001). Upon application of load, these columns compress and buckle.

In Fig 4.1.c, a typical stress-strain behavior is represented for a foam-like material. The material behavior could be modelled in three domains, i.e. elastic (I), plastic (II), and densification (III). In domain I, the columns of the foam structure deform compression and elastic buckling. Upon release of the applied load in domain I, the material would relax back to its natural state. In domain II, the foam undergoes plastic buckling. The columns buckle plastically and do not return to the original state. Domain III is where the foam cells completely collapse and densify. The pores close completely, and the foam behaves like a solid material.

The constitutive relations for a foam was developed for the three domains. The elastic domain was modeled using elastic Hooke's law, the plastic domain using linear isotropic hardening and the densification domain based on power law hardening.

$$\varepsilon = \frac{\sigma}{E}; 0 \leq \sigma < \sigma_y \quad (4.1)$$

$$\varepsilon = \frac{\sigma_y}{E} + \frac{\sigma - \sigma_y}{H}; \sigma_y \leq \sigma < \sigma_d \quad (4.2)$$

$$\varepsilon = \frac{\sigma_y}{E} + \frac{\sigma_d}{H} + \frac{(\sigma - \sigma_d)^m}{H_d}; \sigma \geq \sigma_d \quad (4.3)$$

Where, ε is the observed strain, σ is the applied stress, E is the modulus of elasticity, H is the isotropic hardening coefficient, H_d is the densification hardening coefficient, m is the densification hardening exponent, σ_y is the yield stress, and σ_d is the densification stress.

The stress-strain relations were used to fit the material parameters like $\sigma_y, \sigma_d, H, H_d$ and m from experimental data for different separator materials. The ionic-conductivity of lithium flowing through the separator is modeled analogous to the permeability of fluid in a foam. The permeability decreases as a foamy-material is compressed, which is an effect of the pore-closure upon loading. A similar analogy is considered in our present model, where the separator under compressive load is unable to maintain the flow of lithium-ions due to pore-collapse.

A framework developed by Dawson et al (Dawson, Germaine, and Gibson 2007) was considered to model the conductivity-stress model. In the elastic domain, the ionic-conductivity (κ) was modeled linearly varying with the compressive stretch ($1 + \varepsilon$).

$$\kappa = \kappa_0(1 + \varepsilon); 0 \leq \varepsilon \leq \varepsilon_{el} \quad (4.4)$$

Where, ε_{el} is the yield strain ($= \frac{\sigma_y}{E}$) of the material and κ_0 is the ionic-conductivity of the foam material under no load condition. In the plastic and densification domains (up to ε_{max}), the conductivity is modeled as a linear superposition (rule of mixture) of elastic and densified conductivity based on the relative density of the material. The elastic density and densified density (χ_{el} and χ_d) are found from the strain.

$$\chi_{el} = \frac{(\varepsilon_d - \varepsilon)(1 - \varepsilon_{el})}{(1 - \varepsilon)(\varepsilon_d - \varepsilon_{el})} \quad (4.5)$$

$$\chi_d = \frac{(\varepsilon - \varepsilon_{el})(1 - \varepsilon_d)}{(1 - \varepsilon)(\varepsilon_d - \varepsilon_{el})} \quad (4.6)$$

The conductivity in domains II and III was found as following.

$$\kappa = \kappa_0 \frac{(1 + \varepsilon_d)^{2\alpha}(1 + \varepsilon_{el})}{\chi_{el}(1 + \varepsilon_d)^{2\alpha} + \chi_d(1 + \varepsilon_{el})}; \varepsilon_{el} \leq \varepsilon \leq \varepsilon_d \quad (4.7)$$

In order to simplify the analysis, the electrodes were assumed to behave like a ceramic plate with negligible deformation upon compression. The entire effect of the applied load was implied upon the separator membrane.

4.2.2 Chemo-thermal model for pouch cells:

The diffusion mechanism of the pouch cells was simulated based on Single Particle Model (SPM) (Doyle, Fuller, and Newman 1993). The electrode was assumed to be represented by a single electrode particle (spherical) and the effective electronic current was assumed to be constant throughout the electrode. This assumption is valid considering that the electrolyte is a lithium source and the liquid-phase potential difference is negligible. The charge/discharge was performed

at constant current with same rate of charging over the entire cycle. Three different modes of heat generation were considered in the analysis, i.e. i.e. polarization (\dot{Q}_p), entropic (\dot{Q}_e), and resistive (or joule) (\dot{Q}_j). The equivalent volumetric heat generation for the electrode (q_e) was found by volume averaging all the heating sources with the particle volume (V_{par}).

$$q_e = \frac{\dot{Q}_p + \dot{Q}_e + \dot{Q}_j}{V_{par}} \quad (4.8)$$

The lithium-ion diffusion into the particle was assumed to be completely based on a diffusion-intercalation mechanism, governed by the Fick's Second Law of mass transport. A constant mass flux (Neumann-type) was considered at the particle surface and zero-flux at the particle center to maintain spherical symmetry.

$$\frac{\partial c_s}{\partial t} = D \left(\frac{\partial^2 c_s}{\partial r^2} + \frac{2}{r} \frac{\partial c_s}{\partial r} \right) \quad (4.9)$$

$$-D \frac{\partial c_s}{\partial r} \Big|_{R_e} = i_n = \frac{I_{app}}{\frac{3\epsilon}{R_e} L_e F} \quad (4.10)$$

$$\frac{\partial c_s}{\partial r} \Big|_0 = 0 \quad (4.11)$$

Where, I_{app} is the applied current flux, c_s is the solid-phase lithium-ion concentration, D is the lithium diffusion coefficient of the electrode, ϵ, L_e are the porosity and thickness of the electrode, R_e is the average electrode particle radius, and F is the Faraday's constant.

The current and surface over-potential ($\eta = \phi_s - U_{OCV}$) for the electrode, were expressed as a function of the normalized lithium-ion concentration $\left(\frac{c}{c_{max}}\right)$, using the Butler-Volmer kinetics.

$$i_n = 2Fk_r \sqrt{c_l(c_{max} - c_s)c_s} \sinh\left(\frac{\alpha F}{RT}\eta\right) \quad (4.12)$$

Where, c_i is the molar concentration of the electrolyte, c_{max} is the maximum lithium concentration in the electrode, k_r is the reaction constant of an electrode. The heat generation in the electrode from the three mechanisms were calculate as follows.

$$\dot{Q}_p = i_n \eta A_{par} \quad (4.13)$$

$$\dot{Q}_e = i_n T \frac{\partial U_{OCV}}{\partial T} A_{par} \quad (4.14)$$

$$\dot{Q}_j = i_n^2 \rho_s V_{par} \quad (4.15)$$

Where, A_{par} is the electrode surface area, ρ_s is the electrical resistivity of the electrode material, $\frac{\partial U_{OCV}}{\partial T}$ is the entropic heating parameter measured as the variation of the open circuit voltage (U_{OCV}) with temperature (T).

Three different lithium battery were considered with graphite anode and lithium cobalt oxide/lithium manganese oxide/lithium ferrous phosphate as cathode materials. Table 4.1 provides the simulation data for the three different electrode material.

Table 4.1 *Chemo-thermal properties for cathode and anode materials used in current work (A. Sarkar, Shrotriya, and Chandra 2018).*

Cathode Material	LCO	LMO	LFP	C
Property				
$R_s (\mu m)$	4.2	1.3	0.4	15
$L_e (\mu m)$	100	100	100	150
$D (m^2/s)$	2×10^{-13}	7×10^{-15}	8×10^{-16}	3.9×10^{-14}
$k_r \left(\frac{m^{\frac{5}{2}}}{mol.m^3} \right)$	1×10^{-10}	2×10^{-11}	3.12×10^{-12}	5×10^{-11}
$\frac{\partial U_{OCV}}{\partial T} \left(\frac{mV}{K} \right)$	0.25	0.50	0.30	0.14
$\rho_s (\Omega.m)$	1×10^4	81	1×10^5	6×10^{-4}
$k_{th} \left(\frac{W}{m.K} \right)$	0.32	0.80	2.70	80
$c_{max} \left(\frac{mol}{m^3} \right)$	49,900	22,900	21,200	30,500

The heat generation in the separator membrane is due to the resistance to ion transport due to the internal conductivity of the membrane material.

$$\dot{q}_{sep} = \frac{\left(\frac{I_{app}}{\delta_{sep}}\right)^2}{\kappa} \quad (4.16)$$

The thermal diffusion equation was solved for the entire battery by considering the respective heat generation sources in each component.

$$\rho c_p \frac{\partial T}{\partial t} = k_{th} \nabla^2 T + \dot{q} \quad (4.17)$$

Where, ρ is the material density, c_p is the specific heat capacity and k_{th} is the thermal conductivity of the electrode. A convective boundary was assumed at the surface. The current collectors were assumed to have zero thermal resistance. An effective average cell temperature was calculated using the individual component temperature and their thickness.

4.3 Results and Discussion

The chemo-thermal model was simulated for three different lithium batteries. The particle radius was selected such that the time for charge/discharge was same in all the cells considered for the analysis. Six different separator materials were considered in the analysis. The first case study was used as a validation/cure-fit case and the ionic-conductivity of the remaining five separators were predicted. The individual layer thickness was assumed to be $150\mu m$, $100\mu m$, and $50\mu m$, for the anode, cathode and separator, respectively. Any phase-transformation in the electrode material was ignored for simplification and the models were simulated on Matlab 2017a (MATLAB 2017) platform.

4.3.1 Validation of separator model:

The assumption that the separator membrane behaves like an open-cell foam needed to be validated against experimental data. In a paper by Peabody and Arnold (Peabody and Arnold

2011), a jelly-rolled Celgard 2340 trilayer separator was tested with a LCO/C cell. The separator was operated under an external compressive load ranging from 0 – 30 MPa. The stress-strain and stress-conductivity data were estimated and plotted to show that the ionic-conductivity diminishes with load increment.

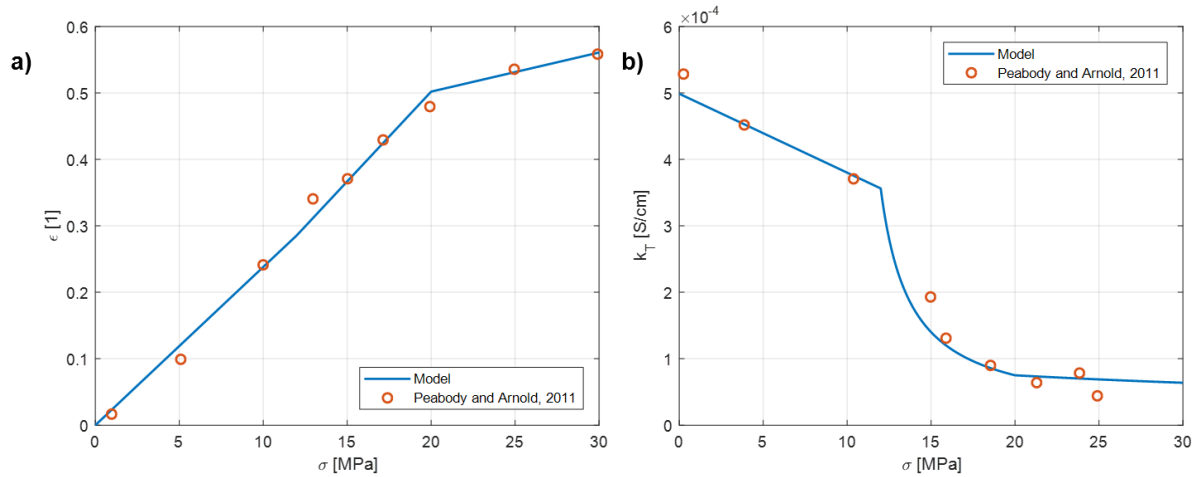


Figure 4.2 a) Strain-stress data for Celgard 2340 from Peabody and Arnold, 2011 (Peabody and Arnold 2011) and curve-fit of model, b) Conductivity vs stress data from Peabody and Arnold, 2011 and predicted conductivity validation against experimental data.

The strain/stress data was fitted with the developed model in Fig 4.2.a. The parameters were evaluated based on the best fit possible (Table 4.2). The conductivity prediction in Fig 4.2.b showed an excellent match between the experimental and predicted data. This analysis validated the foam-based material behavior assumption of the separator membrane.

4.3.2 Prediction of ionic-conductivity for different separator materials:

After model, the foam-based analysis was extended to five different separator materials, i.e. monolayer polyethylene (PE), trilayer PP/PE/PE (TL), non-woven (NW), ceramic-coated (CC), and monolayer polypropylene (PP). The material properties were allocated from experiments performed by Zhang et al. (Xiaowei Zhang, Sahraei, and Wang 2016) and Cannarella and Arnold (Cannarella and Arnold 2013).

Table 4.2 Fit Parameter for Peabody and Arnold, 2011(Peabody and Arnold 2011) data.

Property	Fitted Data (Peabody & Arnold, 2011)
E (MPa)	42
H (MPa)	37
H_d (MPa)	170
σ_y (MPa)	12
σ_d (MPa)	20
ε_{el}	0.2857
α	1.25
m	1.0
κ_0 (S/cm)	5.0×10^{-4}

In a comprehensive study of the separators represented by Arora and Zhang (Arora and Zhang 2004), the separators for batteries were divided based on their physical and chemical properties. Microporous separators are fabricated from polyethylene (PE), polypropylene (PP), Teflon (PTFE), polyvinyl chloride (PVC), etc. with pore size ranging from 50 – 100 (Å). These materials are suitable to be operated at low temperatures (<100°C), especially in lithium-ion cells. Non-woven separators are produced from textile fibers, manufactured as sheets, web or matt of directional or randomly oriented fibers. The pore size for such materials vary between 1 – 100 (μm). Their difficulty to be made thin (<25 μm) makes them a hard choice for lithium-ion cells. Coated separators have a solid matrix with a liquid phase, for example PVdF coated polyolefin-based microporous separators. Commercial separators for lithium battery offer pore size in the

range $0.03 - 0.1 \text{ } (\mu\text{m})$, with porosity of $30 - 50\%$. The low melting point of polyethylene separators allows them to be used as a thermal fuse. DSC results for PE and PP separators show a spike at 135°C and 165°C , respectively (Baldwin et al. 2010). The membrane melts at these temperatures leading to an internal short causing a condition for thermal runaway. The trilayer membrane (PP/PE/PP) was developed by Celgard where a PP layer is designed to maintain the integrity of the film, while the low melting point of PE layer was intended to shut down the cell if an over-temperature condition was obtained.

The experiments performed by Zhang et al. (Xiaowei Zhang, Sahraei, and Wang 2016), provided a detailed understanding of the material behavior of separator membrane under tensile and compressive loading, also showing the creep strain rate dependence of these materials.

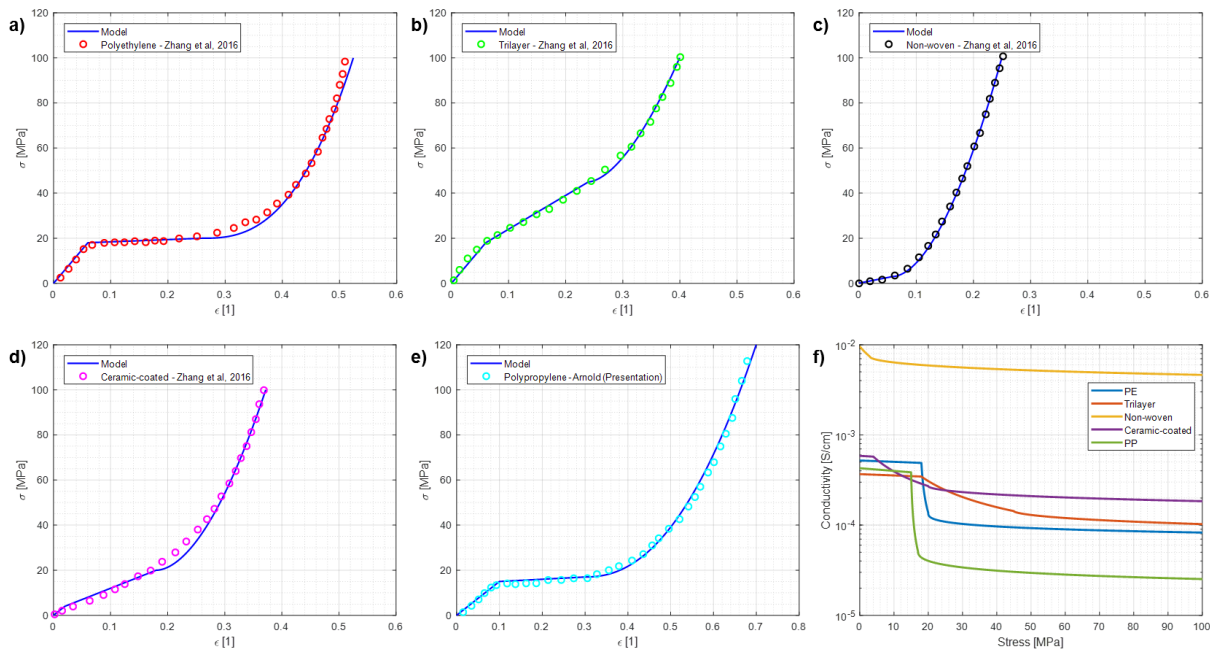


Figure 4.3 a – e) Curve-fit of stress-strain constitutive relation for PP, Trilayer, Non-woven, Ceramic-coated and PE separators against Zhang et al 2014, f) Conductivity prediction for five separator materials over 0 - 100 (MPa) applied compression.

Table 4.3. *Fit data for five different separator material(Arora and Zhang 2004; Baldwin et al. 2010; Yen 2002).*

Property	PE	Trilayer	Non-woven	Ceramic-coated	PP
E (MPa)	300	300	300	200	150
H (MPa)	10	150	50	100	10
H_d (MPa)	1.45	1.10	1.45	1.10	0.9
σ_y (MPa)	18	18	0.1	4	15
σ_d (MPa)	20	45	3	20	17
ε_{el}	0.06	0.06	0.0003	0.02	0.1
ε_d	0.52	0.40	0.25	0.37	0.3
m	0.38	0.6	0.55	0.6	0.45
$\kappa_0 \times 10^{-4}$ (S.cm ⁻¹)	5.48	3.87	100	6.17	4.50

In Fig. 4.3.a – e, the experimental data was fitted by the constitutive model developed in this paper. Materials like monolayer PP, PE, and trilayer PP/PE/PP have a well-defined elastic domain followed by plasticity and densification. The trilayer material has a higher plastic hardening characteristic than monolayer material. As for the non-woven and ceramic-coated separator materials, the elastic domain is almost non-existent. The conductivity for the different foam materials were predicted by substituting the stress-strain relation into the permeability model (Fig. 4.3.f). Apart from the non-woven separator, all other materials have a similar ionic-conductivity but follow different fade characteristics upon application of load. Polypropylene separator has a better ionic-conductivity than the trilayer material at no-load condition. As the load increases, the PP materials shows the most dramatic decay causing it to have high resistance to ion

transport under load. The trilayer membrane has a much shallower fade making the suitable for stable application under loaded conditions.

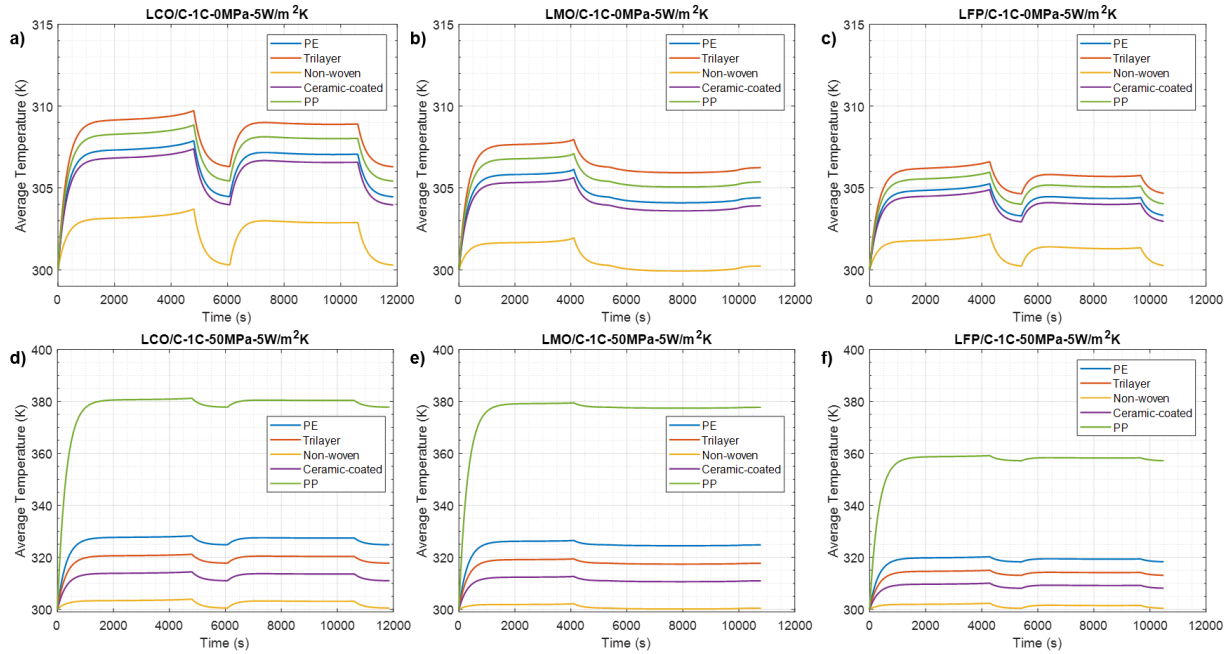


Figure 4.4. Average cell temperature vs time over one charge discharge cycle at 1C (CCCC) for three lithium-ion pouch cells, i.e. LCO/C, LMO/C and LFP/C, with natural convection boundary condition ($h = 5W/m^2 \cdot K$) under; a – c) No-load condition; d – f) 50MPa applied compression.

Three different cathode material were simulated with five different separator material for thermal analysis (Fig. 4.4.a – f). The cells were operated at 1C constant current charge/discharge cycle with zero current at the end of each cycle to normalize to concentration profile. A natural convection boundary condition ($h = 5W/m^2 \cdot K$) was implied on the outer surface of the cell. Two case-studies were considered, i.e. one with no-load (Fig. 4.4.a – c) and second with a 50MPa of applied compressive load (Fig. 4.4.d – f). The comparison among the three different lithium cells predict that LCO/C cell has the highest heating tendency closely followed by the LMO/C cell. The LFP/C cell generates the lowest heat and hence are the most thermally stable among the three [Sarkar et al]. Comparing the different separator membrane under no loading condition, the trilayer membrane generates the most heat (or produces the highest average cell temperature in Fig

4.4.a – c) closely followed by the monolayer propylene (PP) membrane. However, the temperature difference among PP, PE, TL and CC is within $\pm 3^{\circ}\text{C}$ and therefore not significant at 1C rate of charging. For the 50MPa case-study, the PP separator shows the worst thermal profile leading to meltdown upon operation. The trilayer membrane performs much better (refer Fig. 4.3.f) because the trilayer conductivity does not decay rapidly compared to PP monolayer separator. The non-woven separator membrane works best in all conditions due to excellent ion-conductivity.

A thermal map was conceived as an output of the chemo-thermal model for the lithium-ion pouch cell. The average cell temperature over a cycle was predicted from the model. The model was simulated for different loading conditions, rates of charging and cooling characteristics. The advantage of such thermal maps is to provide a design guideline depicting domains of safe versus unsafe operating conditions for such pouch cells. In order to pursue the application of lithium-ion pouch cell as a structural and flexible battery unit, it is quintessential to have a criterion for thermally safe design of pouch cells under applied load. The contour maps in Fig. 4.5 and Fig. 4.6 provide a layout for selection of operating parameters, for example, the cooling system necessary or the maximum rate of charging allowable for structural lithium cells under a known applied compressive load.

The first analysis was performed by predicting the maximum cell temperature over a cycle upon variation of the applied stress (0 – 100 MPa) and the rate of charging (0.5C – 3C). Contour maps were plotted for three different lithium-ion pouch cells with monolayer PP (Fig 4.5.a – c), trilayer PP/PE/PP (Fig 4.5.d – f), and non-woven (Fig 4.5.g – i) as separator membranes.

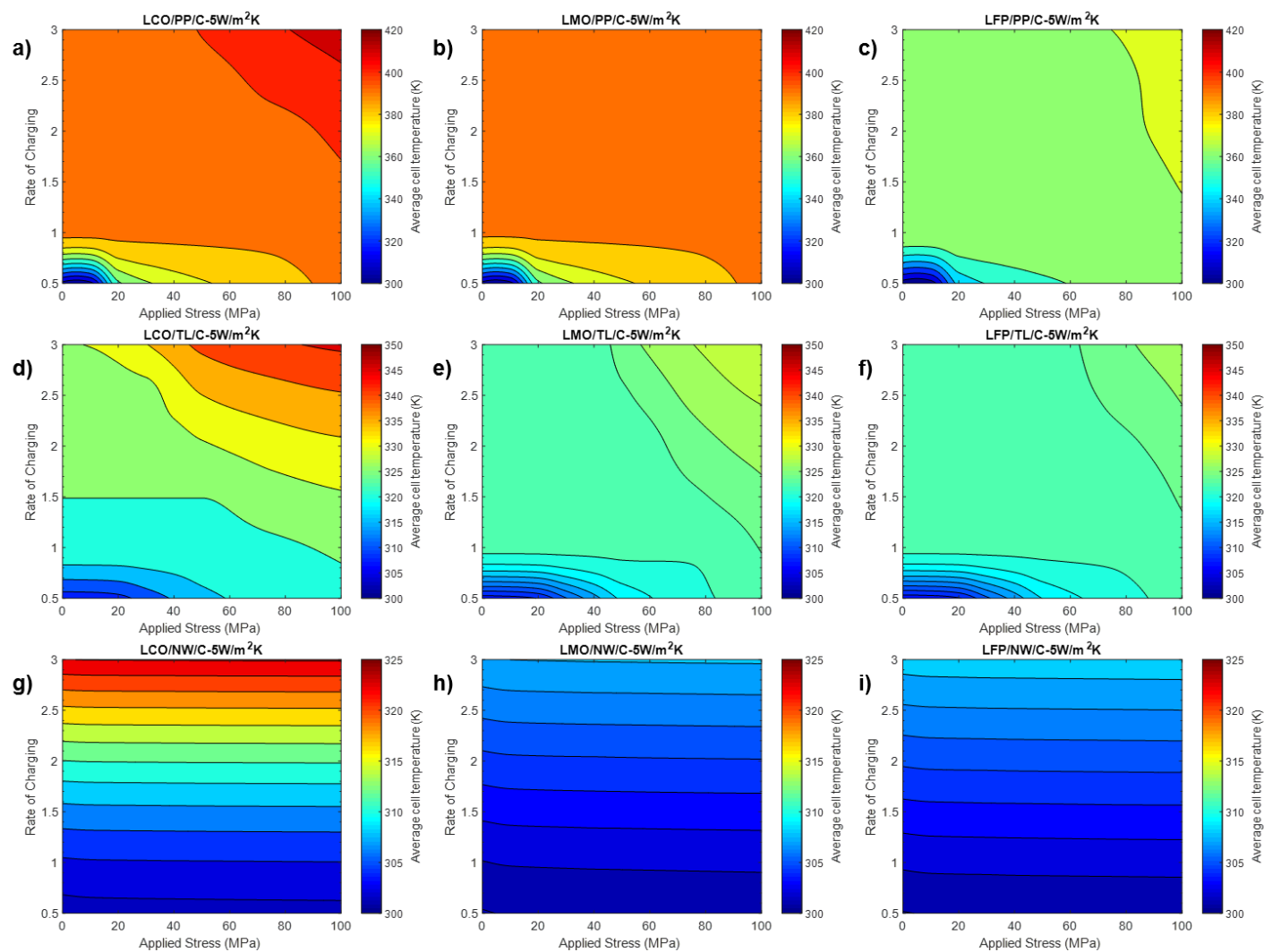


Figure 4.5. Thermal map contour predicting variation of average cell temperature for LCO/C, LMO/C and LFP/C pouch cells over a range of stress (0 – 100 MPa) and rate of charging (0.5 – 3) for three separator material, a – c) monolayer PP, d – f) trilayer PP/PE/PP, g – i) Non-woven.

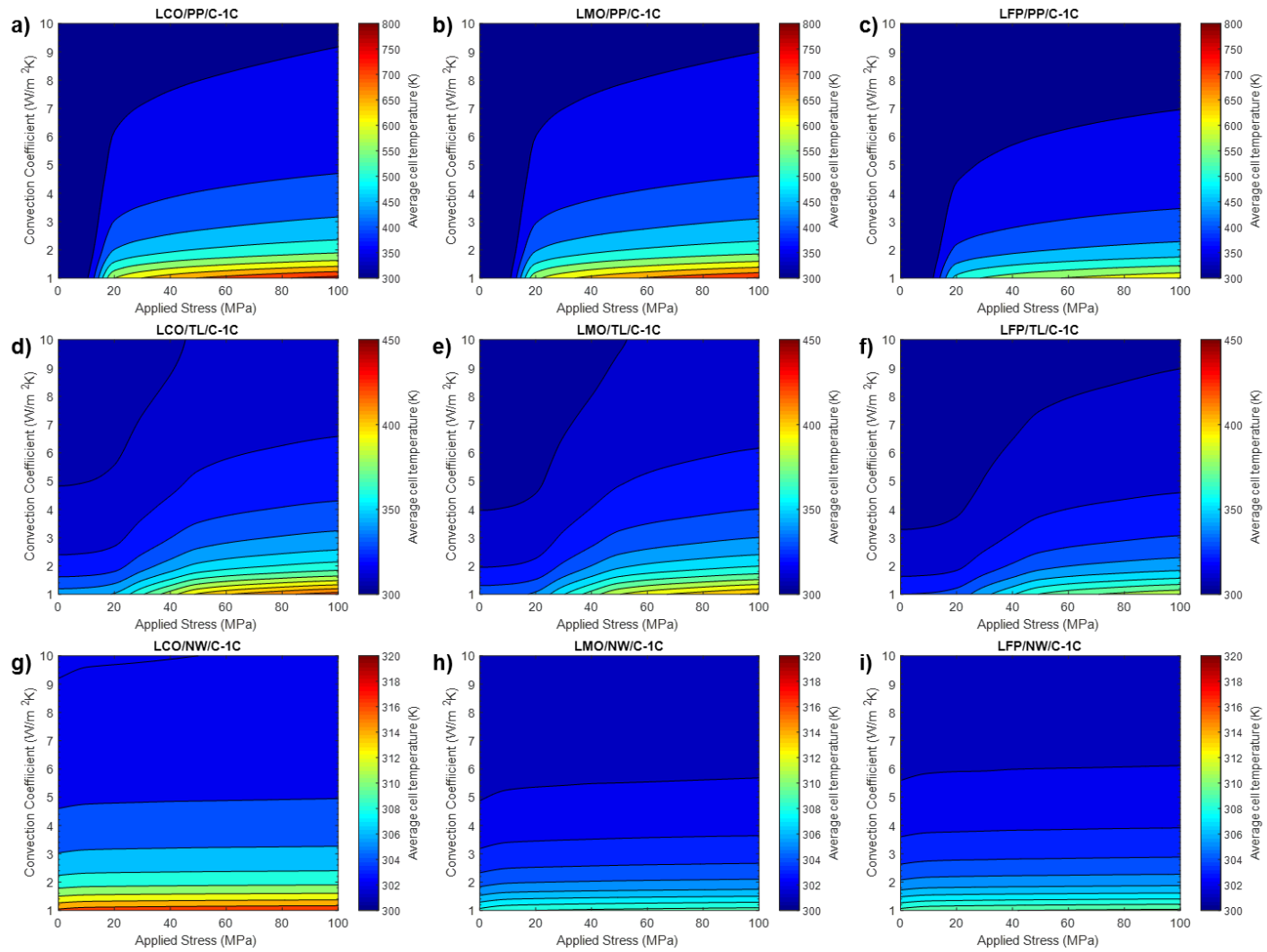


Figure 4.6. Thermal map contour predicting variation of average cell temperature for LCO/C, LMO/C and LFP/C pouch cells over a range of stress (0 – 100 MPa) and convection coefficient (1 – 10 W/m²K) for three separator material, a – c) monolayer PP, d – f) trilayer PP/PE/PP, g – i) Non-woven.

For LCO/C and LMO/C cells with monolayer PP separator (Fig 4.5.a, b), the temperature domain reaches a domain greater than 400K (or 130°C) for stresses above 80 MPa and C-rates above 2.5C. The separator membrane would meltdown at these temperatures causing the possibility of electric short between the electrodes leading to thermal runaway. For the LFP/C cell (Fig. 4.5.c) the maximum temperature possible is about 370K (or 100°C) predicting a lower possibility of meltdown under high load and fast charging application. Trilayer separator membrane (Fig 4.5.d – f) is much safer in operation under extreme loading conditions. The maximum temperature under high loading condition predicted was as high as 350K (or 77°C) for the LCO/C cell and as low as 325K (or 52°C) for LFP/C cell. The best performance was recorded for non-woven separator-based cells (Fig. 4.5.g – i). Under heavy loading condition, the maximum temperature varies between 325K (or 52°C) and 310K (or 37°C) for LCO/C and LFP/C cells, respectively.

Similar thermal maps were created by predicting the maximum cell temperature over a cycle upon variation of the applied stress (0 – 100 MPa) and the convection coefficient (1 – 10 W/m^2K). Contour maps were plotted for lithium-ion pouch cells with monolayer PP (Fig 4.6.a – c), trilayer PP/PE/PP (Fig 4.6.d – f), and non-woven (Fig 4.6.g – i) as separator membranes. The cell temperature was found to be extremely sensitive of convection coefficient for PP separator-based cells (Fig. 4.6.a – c). The maximum temperature recorded was greater than 750K (or 480°C) for the LCO/C cell and 450K (or 180°C) for LFP/C cell at 0.5 W/m^2K and 100MPa load. However, at high cooling coefficient ($h = 10W/m^2K$) the battery is safe to operate at a running temperature of 310K (or 37°C). For a trilayer separator (Fig. 4.6.d – f), LCO/C cell has a maximum temperature of 450K (or 180°C) and LFP/C cell has 370K (or 100°C). The cell temperature drops down to 300K (or 27°C) at 10 W/m^2K cooling coefficient and up to 30 MPa for LCO/C, 40 MPa for LMO/C and 100 MPa for LFP/C cells. Non-woven

separator-based cells predicted a safe-operating maximum temperature of 325K (or 52°C) for the LCO/C cell, 310K (or 37°C) for the LMO/C and LFP/C cells.

The thermal contours could be used as a design map for deciding the loading and operating condition for structural lithium-ion cells. Any domain with temperature ranging 120°C or greater could be considered as meltdown situation leading to thermal runaway. It could also be stated that monolayer PP separators were found to be the worse for application in structural pouch cells and non-woven were the most applicable.

4.4 Conclusion

A novel approach towards application of lithium-ion cells as structural units capable of operating under load was developed. The concept of modeling the separator membrane as an open-cell foam was theorized and validated against experimental evidence. A chemo-thermal diffusion-based thermal model was developed to simulate the thermal profile for three different lithium-ion cells in combination with five different separator membranes. An ionic-conductivity model was developed to predict the conductivity variation of the separator under compressive stress. It was established that LCO/C cells generate the highest thermal energy and LFP/C the lowest. Furthermore, monolayer PP membrane were established as the worst candidate for structural pouch cells as they have terrible performance under loaded condition and have a high feasibility of separator meltdown leading to thermal runaway of the battery. Trilayer membranes show a reasonably good performance but are over-shadowed by the performance of non-woven membrane material. The non-woven materials show excellent thermal characteristic due to their significantly higher ionic-conductivity. Hence, trilayer-based LFP/C cells are concluded as the best candidate for a thermally stable, high-performance lithium-ion pouch cell for structural applications.

CHAPTER 5. CHEMO-ECONOMIC ANALYSIS OF BATTERY AGEING AND CAPACITY FADE IN LITHIUM-ION BATTERY

5.1 Introduction

Advancements in the lithium-ion battery technology over the past couple of decades have revolutionized the electronic, automotive and power industry (Tarascon and Armand 2001; John B. Goodenough and Park 2013). Lithium-ion battery now have high energy density ($>150\text{Wh/kg}$), high cycle life (>2000 cycles) and high columbic efficiency ($>95\%$), making these energy storage units long lasting, portable and efficient (Zu and Li 2011). Lithium-ion battery being an electrochemical system, has transport of both ions and electrons. During intercalation process the lithium ions and the electrons would combine at the electrolyte/electrode interphase, making this the most critical domain in the entire battery (Dey 1970; Peled 1979, 1997; Aurbach et al. 1999; Winter 2009; Verma, Maire, and Novák 2010). A passivation layer is formed on the top of the negative electrode at the interface during charging making the electrochemical design complicated. The concept of the solid electrolyte interface (SEI) was first established by Peled et al, 1979, as an electronically insulating but ionically conductive passivation layer at the electrode/electrolyte interface (Peled 1979) and the composition of the film was determined and summarized by Peled et al, 1997 (Peled 1997) and Aurbach et al (Aurbach et al. 1999).

The SEI layer formation and growth is both a benefit and drawback for the lithium-ion battery. As the SEI layer grows, it restricts the electron tunneling from the electrolyte thus prohibiting further electrolyte reduction. This improves the electrochemical stability of the lithium battery. On the other hand, the formation and growth of the SEI layer occurs due to consumption of the active lithium material from the electrolyte, thereby reducing the capacity of the battery (Winter 2009; Verma, Maire, and Novák 2010). The SEI formation mechanism is still a highly researched topic. According to Goodenough and Kim (J. B. Goodenough and

Kim 2011) SEI is formed when the redox potential of the electrode lies outside the potential range for the battery. The potential range for the most electrodes used in lithium-ion battery have been calculated using density functional theory (J. B. Goodenough and Kim 2011; Xing et al. 2011; Delp et al. 2016; Xuerong Zhang, Pugh, and Ross 2001). SEI growth has been initially observed in lithium metal electrodes with non-aqueous electrolytes. Later, different anode materials were considered for better performance of lithium battery of which graphite as the anode showed acceptable life and performance considering capacity fading $\sim 50\%$ due to SEI formation and growth (W. J. Zhang 2011; Fong 1990; Novák et al. 1999). Experimental analysis of SEI film growth, the effective capacity fade in battery and post mortem analysis on SEI film deposition have revealed the composition, growth rate and fading ability of battery due to an active SEI. However, it is not feasible to monitor the kinetics and thermodynamics of the SEI layer with the available experimental methodology. Prognostic modeling of SEI growth and the prediction of capacity fading using electrochemical degradation models are the best option towards further analysis into the SEI. There have been several works performed on modeling the anode reduction during SEI formation using techniques like molecular dynamics and quantum chemistry (Shi et al. 2015; Urban, Seo, and Ceder 2016; Ramos-Sanchez et al. 2016). Continuum level modeling of lithium battery with SEI was initially started as a modification on the Newman electrochemical model to incorporate SEI current as the irreversible loss parameter (J. S. Newman and Tobias 1962; J. Newman et al. 2003). Peled et al, 1979 (Peled 1979) modeled a parabolic SEI growth mechanism and later the model got modified to derive the \sqrt{t} nature of the capacity loss over battery cycling (Broussely et al. 2001; Colclasure, Smith, and Kee 2011).

A continuum level modeling of lithium battery involves the solving of a set of six couple ODEs and PDEs governing the diffusion, kinetics and charge conservation as developed by Newman et al (J. Newman et al. 2003). Modeling the SEI and battery degradation involves

modifying the Newman model to include the SEI kinetics and growth. In the work the Prada et al (Prada et al. 2013) and Ekstrom and Lindbergh (Ekstrom and Lindbergh 2015), the capacity fade and power fade were modeled for a lithium ferrous phosphate (LFP)/graphite (C) battery. Reduced order models have been popularly used to approximate the solution for a battery simulation. The single particle model have been popularly used with the assumption of constant reaction current to reduce the complexity of the Newman model by decoupling the governing equations (Moura et al. 2017). Reduced order models have been also used to simulate battery degradation by SEI formation (X. Jin et al. 2017; Baek, Hong, and Cha 2015; Barai et al. 2015; Pinson and Bazant 2012). The objective of the reduced order models is to lower the complexity for the SEI kinetics by considering a substitute model or parameters for replace the reaction coefficient for the SEI current. In the work done by Baek et al (Baek, Hong, and Cha 2015), a linear SEI profile was assumed by replacing the reaction coefficient for the SEI current by a constant. Jin et al (X. Jin et al. 2017), proposed a non-linear model for the reaction coefficient and used a numerical optimization to predict capacity fade in LFP/C cell.

In the current work, a reduced order electrochemical model has been developed for a lithium-ion battery with a non-linear scheme to model the SEI current. The proposed model was applied with an efficient Euler Implicit scheme for accurate and rapid prediction of capacity fade in lithium battery. The model was adjusted for graphite-based anodes based on experimental results for lithium cobalt oxide (LCO)/graphite (C) cell and validated for LCO/C and LFP/C cell. A novel concept of ageing the lithium battery prior to commercialization was conceived and simulated to predict the capacity loss for aged lithium cell. The ageing process was design to reduce the effect capacity loss over the operation period of the battery and would be advantageous for applications were battery replacement is not affordable, like EV or biomedical applications. Finally, an economic analysis was performed to provide a cost versus capacity comparison involved selection of aged lithium battery based on the application.

5.2 Mathematical Model

A reduced-order battery degradation model was developed with the ability to predict capacity fade over multiple cycles. A single particle electrochemical model was utilized to simulate a lithium-ion pouch cell with a constant-current type discharge and a constant-current-constant-voltage type charge characteristic. The lithium cell was assumed to have a dilute reaction species behavior with the electrolyte to be a lithium source/sink providing a uniform reaction current to the electrode particles. The ionic current variation throughout the electrode was assumed to be linear. However, the overall lithium species conservation was maintained in the analysis.

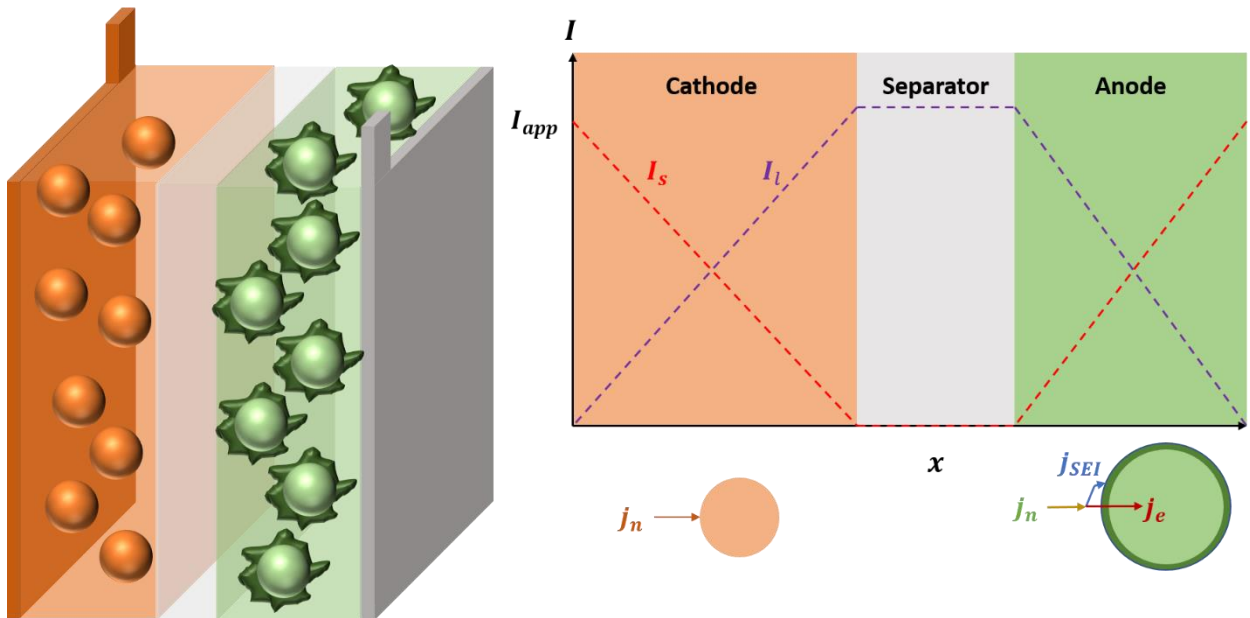


Figure 5.1 *Single particle electrolyte model representation of a lithium-ion battery with SEI growth.*

A lithium-ion pouch cell was considered with spherical electrode particles. The electrode distribution is assumed to be uniform with an average particle size considered for the cathode and anode. The diffusion of lithium-ions into the electrode is governed by Fick's Second Law. The surface of the particle was subjected to the reaction current flux (j_n).

$$\frac{\partial c_s}{\partial t} = D \left(\frac{\partial^2 c_s}{\partial r^2} + \frac{2}{r} \frac{\partial c_s}{\partial r} \right) \quad (5.1)$$

$$-D \left. \frac{\partial c_s}{\partial r} \right|_{R_e} = j_n \quad (5.2)$$

The reaction current is related to the gradient of the ionic current. Since, the ionic current varies linearly with the electrode thickness, the reaction current is a constant.

$$I_l + I_s = I_{app} \quad (5.3)$$

$$(Fa) \cdot j_n = \nabla \cdot I_l = -\nabla \cdot I_s = \frac{I_{app}}{L_e} \quad (5.4)$$

Where, I_l, I_s, I_{app} is the ionic, electronic and applied current flux, c_s is the solid-phase lithium-ion concentration, D is the lithium diffusion coefficient of the electrode, $a = \frac{3\epsilon}{R_e}$ is the effective reaction area per unit volume, ϵ, L_e are the porosity and thickness of the electrode, R_e is the average electrode particle radius, and F is the Faraday's constant.

The current and surface over-potential ($\eta = \phi_s - \phi_l - U_{OCV}$) for the positive electrode, were expressed as a function of the normalized lithium-ion concentration $\left(\frac{c}{c_{max}}\right)$, using the Butler-Volmer kinetics.

$$i_n = 2Fk_r \sqrt{c_l(c_{max} - c_s)c_s} \sinh\left(\frac{\alpha F}{RT}\eta\right) \quad (5.5)$$

For the negative electrode, the reaction current flux ($i_n = Fj_n$) was accounted as a summation of the electrode current (i_e) and the solid electrolyte interface (SEI) current (i_{SEI}). The electrode current is same as that of the positive electrode (Eq. 5.5). The SEI current is driven by the Tafel kinetic as it dominant by the cathodic potential.

$$i_n = i_e + i_{SEI} \quad (5.6)$$

$$i_{SEI} = -i_0 \exp\left(-\frac{\alpha F}{RT}(\phi_s - \phi_l - U_{SEI} - R_{SEI}i_n)\right) \quad (5.7)$$

Where, i_0 is the reaction rate coefficient for the SEI current, U_{SEI} is the SEI open circuit voltage, R_{SEI} is the SEI resistance which is dependent on the SEI film thickness (δ) and electrical conductivity of the SEI film (κ).

$$R_{SEI} = \frac{\delta}{\kappa} \quad (5.8)$$

$$\frac{d\delta}{dt} = -\frac{i_{SEI}M_{SEI}}{2F\rho_{SEI}} \quad (5.9)$$

The growth rate of the SEI film thickness ($d\delta/dt$) depends on the SEI current (i_{SEI}), molar mass and density of SEI (M_{SEI}, ρ_{SEI}). The SEI rate coefficient is modeled as a fitting parameter for graphite electrode.

$$i_0 = \beta F c_{EC} \left(\frac{D_{EC}}{\delta^2} \right) 4\pi R_e^2 \left(\frac{\delta}{A_e} \right) C_r(N)^{-0.5} \quad (5.10)$$

$$\delta = \delta_0 f(N) \quad (5.11)$$

The SEI thickness grows over the process of battery cycling with the initial SEI thickness to be δ_0 . The simulation could only be modeled considering an initially developed SEI layer. The SEI formation mechanism is a highly involved reaction mechanism with the formation time-scale being negligibly small during the first cycle charging. The SEI grows with the number of cycles (N). The reaction current coefficient for the SEI current is modeled with a set of material properties and a constant (β). The combination of material properties was selected to establish the dimension for current flux. Here, c_{EC} is the ethylene carbonate concentration in the electrolyte, and D_{EC} is the diffusion coefficient of lithium-ion in SEI. The term $F c_{EC} \left(\frac{D_{EC}}{\delta^2} \right)$ represents the volumetric current through the SEI film and $4\pi R_e^2 \delta$ represents the SEI volume. The product of these two terms per unit effective electrode area (A_e) represents the reaction current flux through the SEI. The power law for the SEI reaction flux was assumed $\alpha = -0.5$, such that upon integrating over the number cycles the capacity follows the traditional \sqrt{N} characteristic.

The electrolyte-phase lithium concentration (c_l) balance was performed based on diffusion of the lithium ions through the electrolyte. The electrolyte lithium concentration was used to predict the electrolyte phase potential (ϕ_l). The overall cell potential (V) was found as the difference between the solid-phase potentials (ϕ_s) at the current collector. The electrolyte

lithium-ion follows conservation of flux and species at the interface, while the electrolyte lithium-ion flux is zero at the current collectors.

$$\epsilon \frac{\partial c_l}{\partial t} = \nabla \cdot (D_l \nabla c_l) + (1 - t_c^0) j_n \quad (5.12)$$

$$-D_l \nabla c_l|_{cc} = 0 \quad (5.13)$$

$$-D_l \nabla c_l|_{int}^+ = -D_l \nabla c_l|_{int}^- \quad (5.14)$$

$$c_l|_{int}^+ = c_l|_{int}^- \quad (5.15)$$

$$\sigma_l \left(\frac{\partial \phi_l}{\partial x} \right) = -i_n + \sigma_l \frac{2RT}{F} (1 - t_c^0) \left(1 + \frac{\partial \ln f_{\pm}}{\partial \ln c_l} \right) \frac{\partial \ln c_l}{\partial x} \quad (5.16)$$

$$V = \phi_s^+ - \phi_s^- \quad (5.17)$$

$$Q_{cap} = \int_0^{t_{charge}} I_{app} dt \quad (5.18)$$

The capacity fade (Q_{fade}) was calculated as the time integral of the current component lost in the formation of the SEI film. As the SEI layer grew, the SEI current increased and the capacity fade progressed. The relative capacity (Q_{rel}) was calculated as the relative capacity at the end of each charge cycle with respect to the first cycle.

$$Q_{fade} = \int_0^{t_{charge}} i_{SEI} dt \quad (5.19)$$

$$Q_{rel} = \frac{Q_{cap} - Q_{fade}^N}{Q_{cap} - Q_{fade}^1} \times 100[\%] \quad (5.20)$$

5.3 Economic Analysis

An economic analysis was presented to demonstrate the cost versus fade relation for aged lithium-ion batteries. The general trend of capacity fading in lithium batteries underlies the \sqrt{t} type behavior. This implies that the relative capacity change ($\Delta Q_{rel} = Q_{rel}|_N - Q_{rel}|_{N+\Delta N}$) over a certain duration of cycles (consider $\Delta N = 100$ cycles) would reduce as N progresses, although the absolute relative fade ($Q_{rel}|_N$) would increase with N . The concept of

battery ageing arrives considering this reduction in the change in relative capacity (ΔQ_{rel}) as the cell ages.

Table 5.1 *Chemo-thermal properties for cathode (LCO and LFP), anode materials (C) and SEI.*(A. Sarkar, Shrotriya, and Chandra 2018; Safari et al. 2009)

Material Property	LCO	LFP	C
R_s (μm)	4.2	0.4	15
L_e (μm)	100	100	150
D (m^2/s)	2×10^{-13}	8×10^{-16}	3.9×10^{-14}
$k_r \left(\frac{m^{\frac{5}{2}}}{mol \cdot m^3} \right)$	1×10^{-10}	3.12×10^{-12}	5×10^{-11}
$\frac{\partial U_{OCV}}{\partial T} \left(\frac{mV}{K} \right)$	0.25	0.30	0.14
ρ_s ($\Omega \cdot m$)	1×10^4	1×10^5	6×10^{-4}
$k_{th} \left(\frac{W}{m \cdot K} \right)$	0.32	2.70	80
$c_{max} \left(\frac{mol}{m^3} \right)$	49,900	21,200	30,500
			SEI
$c_{EC} \left(\frac{mol}{m^3} \right)$	-	-	4540
D_{EC} (m^2/s)	-	-	5×10^{-19}
δ (nm)	-	-	2
β	-	-	0.8
$M_{SEI} \left(\frac{kg}{kmol} \right)$	-	-	162
$\rho_{SEI} \left(\frac{kg}{m^3} \right)$	-	-	1690

The advantage of this method is that an aged-cell would have a longer cycle life compared to new cells. On the the other hand, to maintain the absolute capacity to be same for the aged and new cells, the initial capacity of the aged-cell has to be comparatively higher than new cells. Let's consider an example problem where a new cell has an absolute capacity of 100mAh ($Q_{rel} = 100\%$) and fades to 90mAh ($Q_{rel} = 90\%$) and 85mAh ($Q_{rel} = 85\%$) by the end of 100 and 200 cycles. The change in relative capacity from 0-100 cycles is 10mAh ($\Delta Q_{rel}|_{\Delta N=100} = 10\%$). If the relative capacity at the end of 100 cycles is considered

$Q_{rel}|_{N=100} = 90\% \rightarrow Q'_{rel}|_{\substack{N'=1 \\ N=100}} = 100\%$, then the relative fade at the end of 200 cycles becomes $Q'_{rel}|_{\substack{N'=100 \\ N=200}} = 94.44\%$, and change in relative capacity fade $\Delta Q'_{rel}|_{\Delta N=100} = 4.44\%$. Now, to market a new and an aged cell, both at 100mAh capacity, the aged cell must have an initial capacity of 111mAh (or 11mAh worth more material).

The advantage and requirement of aged lithium-ion battery is focused towards applications that do not have the feasibility to change batteries over short durations. Applications like battery units for HEV or EV and cells used in pacemakers and /or other biomedical applications need to have longer cycle life (over 15 years) with minimal allowable fading. The aged-cell also come with an economic disadvantage, thereby needing to perform a capacity vs economic optimization. As the battery is aged, there is the need for more capital investment (C_{capex}) in starting material to compromise for the inherent fade involved in ageing. Furthermore, the electricity consumed in ageing of the cell adds as an operational cost (C_{opex}).

$$C_{capex} = \frac{Q_{cap}|_{desired}}{Q_{rel}|_N} \times Capital \quad (5.21)$$

$$C_{opex} = V \times Q_{cap} \times \Delta N \times Elec \quad (5.22)$$

$$C_{total} = C_{capex} + C_{opex} \quad (5.23)$$

Table 5.2 Cost analysis data for 18650 cell (Baksa and Yourey 2018; U.S. Energy Information Administration 2018).

Property	Value
$Capital \left(\frac{\$}{Ah} \right)$	3.07 (Baksa and Yourey 2018)
$Elec \left(\frac{\$}{kWh} \right)$	0.139
$Q_{cap} _{desired} (mAh)$	3400
$V (V)$	3.7
$\Delta N (cycles)$	100

The capital expenditure is calculated as the cost per unit capacity (*Capital*, \$/mAh) times the initial capacity needed. The operational expenditure is the electricity per unit (*Elec*, \$/kWh) times the energy consumed to age the cell over ΔN number of cycles.

5.4 Results and Discussion

A reduced-order multiscale mathematical model was developed to simulate battery degradation in lithium-ion battery due to SEI formation and to predict and validate capacity fade in LCO/C and LFP/C battery. The particle level and electrolyte level diffusion models were solved with a Euler Implicit solver with the special discretization completely vectorized in Matlab (MATLAB 2017). This rendered an unconditionally stable temporal iterative solver allowing the possibility of selecting larger time steps, making the computation several orders of magnitude faster. Each cycle iteration was recorder to be performed in 150ms, with a 1000 cycle fading run taking less than three minutes of solution time. The solution for voltage and SEI parameters were solved using a Newton Raphson code allowing very accurate predictions in a short number of iterations.

The electrochemical model was simulated over multiple charge/discharge cycles following a considered charging profile. The initial charging protocol followed for the simulation assumed a constant current charging (galvanostatic) till the cell voltage achieves 4.2V. Then the current was allowed to decay gradually, following a constant voltage (potentiostatic) charging. The potentiostatic condition was applied till the current reached 10% of the maximum current. At the end of the potentiostatic charging, the current was made zero to equilibrate the concentration of the lithium-ion in the electrode particle. Fig 5.2.a represents the standard charge profile considered to simulate the electrochemical SPM for the lithium-ion cell. The β constant in the SEI reaction current of the degradation model was adjusted against the experiments performed by Hu et al. (C. Hu et al. 2014).

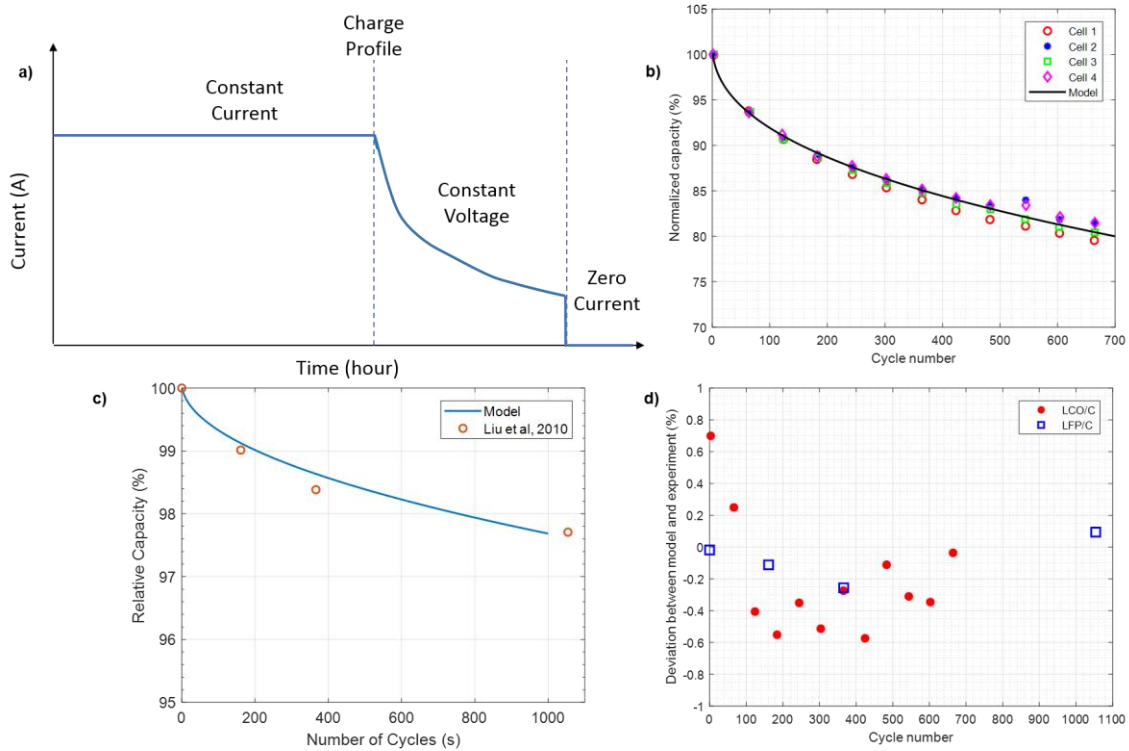


Figure 5.2 Single particle electrolyte model with battery degradation due to SEI formation, a) Representation of the charging protocol, b) Comparison of the model predicted data for LCO/C against experiments performed by Hu et al. (C. Hu et al. 2014), c) Comparison of model predicted data for LFP/C against experimental data from Liu et al. (P. Liu et al. 2010), d) Deviation of model prediction from experimental data for LCO/C and LFP/C.

The primary driving parameter found in the analysis was the growth rate of SEI film. The simulation was performed over a span of 1000 cycles and the initial capacity (at $N = 1$) was considered to be 100%. An initial SEI thickness of 2nm was assumed at the beginning of the first cycle charging to accommodate the preformed SEI. The initial SEI formation mechanism was not considered in the analysis because the SEI layer forms almost instantaneously compared to the time taken to charge the cell. The formation of SEI is a kinetic driven parameter while the growth of SEI is diffusion driven. Hence, only SEI growth was considered in the model. Fig 5.2.b shows the comparison of the model predicted capacity variation against the experimental data for LCO/C cells [ref]. The model was able to capture the trend of capacity fading in LCO/C cell with a high degree of accuracy. The deviation of the model predicted data from the average of the four cells used in the experiment was calculated

(Fig 5.2.d). The deviation for the LCO/C cell simulation was found to be within $\pm 1\%$ of the experimental results over the span of 5%. The deviation converges to near $\pm 0.1\%$ after the first 200 cycles. For the LCO/C cell model, a constant current profile of C/6 was applied followed by a 30min of constant voltage profile and ending with zero current, in each cycle, to match against the referred protocol on Hu et al. (C. Hu et al. 2014). After getting the adjusted parameter β and validating against Hu et al, the model was simulated considering LFP/C cell. Since, SEI grows on the anode and graphite being the anode for both LFP/C and LCO/C cell, it was inferred that the model validated for the LCO/C cell (Fig 5.2.b) should be able to predict capacity fading in LFP/C, or other lithium batteries with different cathode materials. The model was simulated with a LFP/C cell with the particle size for the cathode adjusted to observe the same non-dimensional time ($t_D \propto r^2/D$) as the LCO/C cell. The charge profile was changed to match the protocol observed in Liu et al [ref]. The predicted capacity fading over 1000 cycles was compared against the experimental results predicted by Liu et al. (P. Liu et al. 2010) (Fig. 5.2.c) with no adjustment made to β or any other parameter/property effecting the anode. The predicted results were in close agreement with the experimental results validating the inference that any combination of cathode material with graphite as the anode could be simulated and the capacity fade predicted by the current model. The deviation of the predicted and experimental data for the LFP/C cell over 1000 cycles was calculated (Fig. 5.2.d). The deviation was observed to be within $\pm 0.5\%$ validating the model and also providing a high degree of confidence on the level of accuracy of the model.

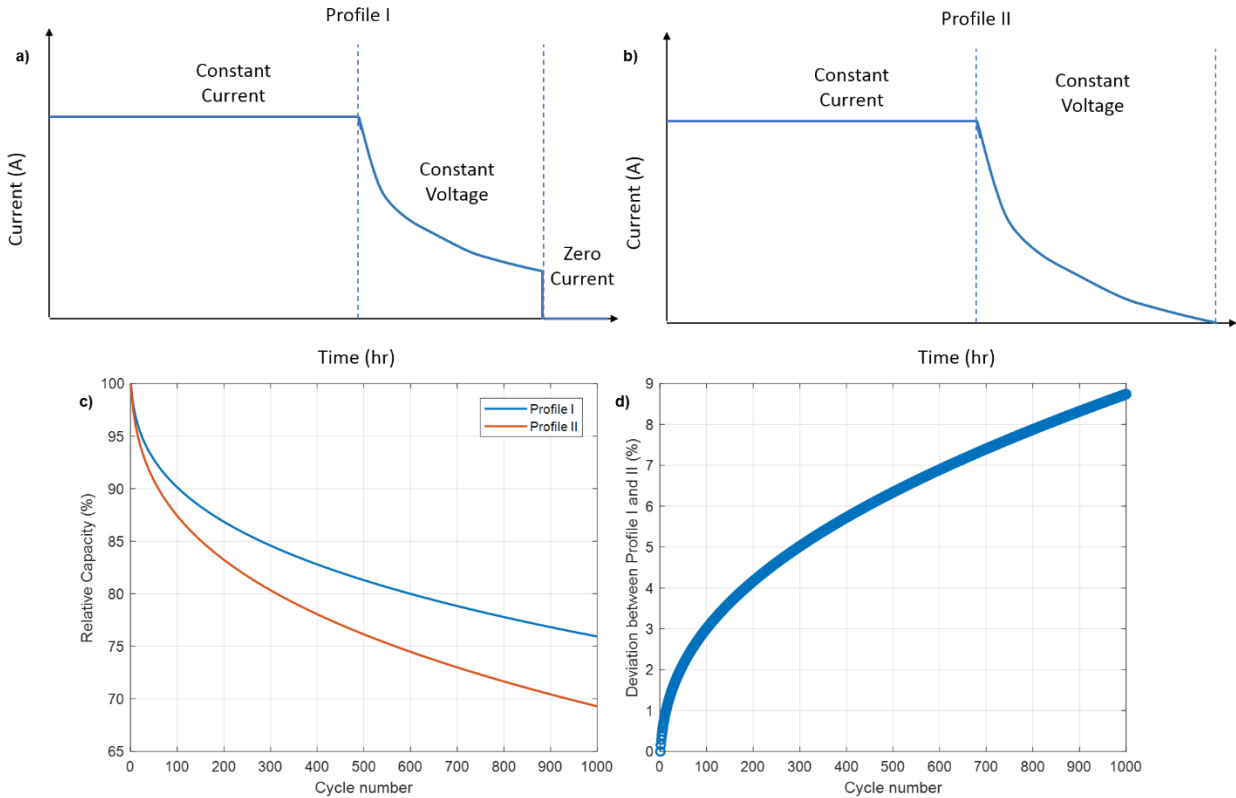


Figure 5.3 Comparison of capacity fading on LCO/C cell with two charging protocols, a) CCCVZC protocol, b) CCCV protocol, c) Comparison of relative capacity fade over 1000 cycles from Profile I and II, d) Deviation of capacity between Profile I and II over 1000 cycles.

A set of simulations were performed to compare the effect of different charging protocols on the relative fading of the battery. From Eq (5.19), the capacity lost is a time integral of the SEI current, which in turn depends on the charge profile. Mathematically a larger area under the current/time profile would mean larger capacity fade. As long as the anode is supplied with current during charging, the SEI layer would keep growing. With this mathematical inference in consideration two different charge profiles (Fig. 5.2.a, b) were simulated with the same initial rate of charging for a LCO/C cell over the same time frame. Profile I was considered the same as Fig 5.1.a, where the charging is done at constant current ($C/6$) till 4.2V was obtained, followed by 30min of potentiostatic charging and ending with a zero current profile to equilibrate the concentration profile. Profile II was considered the similar to Profile I, where the charging is done at constant current ($C/6$) till 4.2V was obtained, but the potentiostatic profile was considered till the current decayed almost to zero. So, for Profile I the

battery is not charged to completely 100% which is in contrast to Profile II. The area under the current/time curve was larger in Profile II than Profile I. The relative capacity for Profile I and II was predicted from the model and compared in Fig 5.2.c, d. Fig 5.2.c shows that the capacity fading in Profile II is more than Profile I as inferred from Eq (5.19). The deviation of the fading between profiles I and II was calculated (Fig. 5.2.d) and by 1000 cycles Profile II would have 9% lower capacity than Profile I. The standard protocol of constant current – constant voltage – zero (CCCVZC) current has higher cycle life and performance compared to a constant current – constant voltage (CCCV) charging profile. Hence, it is advantageous to not charge the battery up to 100% of its potential.

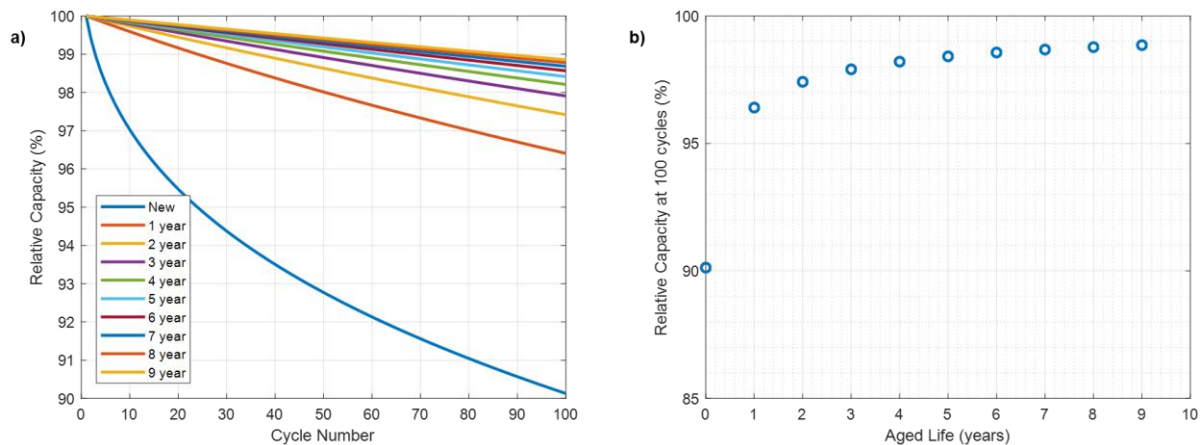


Figure 5.4 a) Capacity fade over 100 cycles for aged-batteries from ageing span of 0 - 9 years, b) Relative capacity of aged-battery at the end of 100 cycles.

A novel concept of battery ageing was conceived and considered for analysis to predict better performing and longer cycle for battery. The capacity fading (or the relative capacity) for a lithium-ion cell follows a \sqrt{N} type profile, where N is the number of charging cycles, and the fading curve flattens out and starts to saturate as the number of cycle increases. So, the change in the relative capacity over a certain number of cycles decreases and the battery is cycled. A battery fading by 10% over the first 100 cycles would fade only by 4% in the next 100 cycles. However, the overall capacity would be much lower at the end of 200 cycles compared to that in 100 cycles. The object of interest in the case of aged lithium batteries is

the change in the relative capacity (or fading) over a definite number of cycles and not the absolute capacity of the cell. For testing the implication of this hypothesis, all aged lithium cells must have the same capacity from the time of testing (or time when the battery is commercially used). The initial capacity for aged batteries could be defined as the starting capacity of these batteries prior to ageing, while commercial capacity is defined as the capacity of the battery from the point of commercial utilization. So, a 200 cycles aged battery, having the same commercial capacity as a new battery, must have a higher initial capacity than a new battery. An analysis was performed for the LCO/C cell considered in Fig. 5.1. The cell was cycled for 1000 cycles with each 100 cycles representing 1 year of battery utilization (or ageing). The ageing was considered such that at the relative capacity at the beginning of the commercial utilization (or after the ageing period) was made 100% and capacity in the cycles onwards was rescaled relative to this. For example, for a two years aged battery the capacity at the end of 200 cycles was made 100% and all the predicted capacity from 200 cycles onwards was scaled accordingly. The change in relative capacities of aged cell, from 0 to 9 years of ageing, were compared over a duration of 100 cycles (or 1 year) (Fig. 5.4.a). The relative capacity at the end of 100 cycles was the lowest for new batteries and increased as the battery was aged (Fig. 5.4.b). In the current analysis, for a new battery the relative capacity at the end of 100 cycles is 90% while for a 4 years aged cell the relative capacity by 100 cycles is 98.2%. This means that aged lithium batteries having the same commercial capacity as new batteries would have a longer cycle life. The benefit of ageing however grows out with ageing and from 5 to 9 years aged battery the capacity benefit is < 1%. This concept of longer cycle life for an aged-battery could be applied to situations where replacement of batteries is not convenient. Lithium batteries used in electric vehicles and for biomedical applications do not have the freedom to be replaced in over 15 years or plus. For such applications, aged battery would be the object of interest.

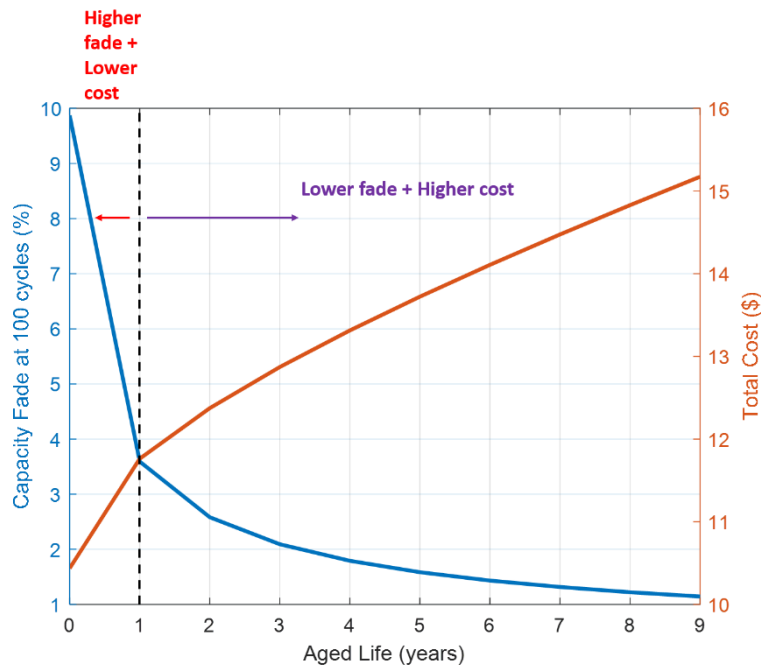


Figure 5.5 Economic analysis of 18650 cells to compare the capacity fade performance of aged-batteries against the total cost of manufacturing and ageing the cells.

Considering the benefits of ageing a battery, the ageing process involves cost in the form of capital and operational requirements. An aged battery has a higher initial capacity than a new battery of the same commercial capacity. For batteries with higher capacity, more starting material is needed, thereby involving more capital cost. Moreover, cycling process involved to age the battery requires operational cost in the form of electricity charges. An economic analysis was performed to calculate the cost of aged 18650 LCO/C batteries over a span of 0 – 9 years of ageing. Fig. 5.5 plots the fade in capacity for aged battery and the equivalent cost of ageing the battery over a span of 9 years. A simple optimization showed that the optimal fade to cost benefit is achieved for a 1 year aged battery. The capacity benefit is maximum at the end of 1 year of ageing is the maximum and the curve gradually flattens out as the ageing progresses. So, very little capacity benefit could be obtained beyond 5 – 6 years of ageing. However, the cost increases steeply making the decision to age the battery tough. So, there is tradeoff between cost and capacity especially where the application demands long cycle life battery units. For biomedical and EV applications where the commercial life is >15

years, it is beneficiary to move towards aged battery. The price paid in ageing the battery is over compensated by the price in replacing the battery. While for cell phone batteries, no ageing is needed as the commercial life for the cell phone itself is 3 – 5 years and lower cycle performance is acceptable as the batteries are cheaper to replace.

5.5 Conclusion

A reduced order electrochemical model was developed to simulate the battery degradation mechanism due to SEI formation on lithium battery anode. A Euler Implicit numerical scheme was developed to solve for the diffusion equation for the electrode and electrolyte to vectorize the model for unconditional stability and rapid convergence. A reduced order non-linear model was developed to simulate the SEI kinetics and film growth over cycling of the battery. The model was adjusted and validated for LCO/C cells to predict capacity fade over 1000cycles with an accuracy of $\pm 0.5\%$. The numerical scheme developed for this model is about $\sim 100 \times$ faster than commercial 1D lithium electrochemical models. The model was also validated against a LFP/C cell inferring that any cathode material in combination with a graphite anode could be simulated with the current model. Two different charge profiles were considered for analysis to test the fading tendency for a CCCV protocol against CCCVZC protocol. It was established that a CCCVZC which does not charge the battery up to 100% shows a much better cycle performance than a 100% charging CCCV protocol. Finally, a novel concept was introduced in which lithium batteries could be aged prior to commercial utilization for lower capacity fading. Ageing of lithium battery would allow a reduced change in the relative capacity over the same the number of cycle period of a new battery due to the non-linear nature of the fade over time curve. However, the ageing of battery involves both capital and operational cost making it an optimization problem between electrochemical requirements and economic vantage point. Aged battery would have a longer cycle life making the prime candidate for EV and biomedical applications, where the cost

inherent in the ageing process is negligible compared to the cost in replacing the unit. The concept of aged battery would be a great candidate for applications requiring cycle life >15 years, especially in pacemakers and other biomedical devices which need surgery for battery replacement.

CHAPTER 6. BOLTZMANN TRANSPORT EQUATION BASED MODELS FOR PREDICTION OF MODE-DEPENDENT PHONON THERMAL CONDUCTIVITY OF SILICON NANOPARTICLE

6.1 Introduction

Silicon and its derived compounds like silica, silicon carbide and silicates as nanoparticles have shown promising utilization in the manufacturing sector. Ceramic silicon carbide nanoparticles are dispersed in magnesium alloys, in their molten state, to produce strong, lightweight materials (L.-Y. Chen et al. 2015). The silicon carbide infusion improves the strength of magnesium alloy without affecting its plasticity and thereby has applications in manufacturing of automobile chassis and airplane structures. Silicon carbide nanoparticles are also used as lubrication for diamond turning of hard materials for low wear of the tool (Yan, Zhang, and Kuriyagawa 2011). Silica nanoparticles are being used in tire manufacturing sector, where addition of silica with carbon black reduces roll resistance and increases the fuel efficiency of the vehicle (*Nano-Produktion – Herstellung von Und Mit Nanotechnologie*, n.d.). In all these applications, silicon nanoparticles are subjected to high temperatures and the analysis of thermal properties of the nanoparticles become crucial.

Ludwig Boltzmann published his renowned transport equation in *Kinetische Theorie II* (Boltzmann 1872), where a set of partial differential equations were formulated to define the probability distribution of a collection of particles in a state of non-equilibrium. The Boltzmann transport equation (BTE) describes the statistical behavior of a thermodynamic system using random but biased distribution of particles and their relative properties (like velocity, body forces and collision characteristics). The equation considers a probability distribution for the position and momentum of a representative particle at an instant of time rather than analyzing the individual position and momentum of each particle. In one of the earliest implementations of the BTE, Klemens derived a generalized formulation for the thermal conductivity of

dielectrics (Klemens 1951). A few years later, the model proposed by Callaway to predict germanium thermal conductivity (Callaway 1959) incorporated effects of the scattering mechanisms due to point impurities, normal (N) three-phonon and Umklapp (U) processes (Kittel 1962), and boundaries. Shortly after, Holland (Holland 1963) presented a modified model that explicitly considered the contributions by both transverse and longitudinal phonons to heat conduction. Nevertheless, the relative accuracy of these models and the associated vibrational modes in predicting phonon thermal conductivity of nanomaterials has only been sparsely reported in the literature (D. Li et al. 2003; S. Jin, Tang, and Fischetti 2008; Liangruksa and Puri 2001; Z. Zhu et al. 2013).

In this work, we infer that longitudinal modes of phonons dominate the transverse modes and contributes to towards stronger thermal conductivity at higher temperature. We consider a crystalline silicon (Si) nanoparticle with diameter of 115 nm as our test bed. The motivation for the material selection is driven by the promising utilization of silicon nanoparticles in machining and manufacturing sector, and their novel use in the manufacturing of electrodes in high capacity lithium-ion cells (Tarascon and Armand 2001; Whittingham 2004; Ellis, Lee, and Nazar 2010; Chang et al. 2014).

6.2 Mathematical Model

The simplified formulation of the BTE at steady state and in the absence of body forces on the Si nanoparticle takes the form $v \cdot \frac{\partial f_0}{\partial r} = -\frac{f-f_0}{\tau}$, where f is the instantaneous probability distribution of particles with velocity v , and τ is the relaxation time. The initial probability distribution f_0 for phonon mediated thermal transport is $f_0 = \frac{1}{e^{\frac{\hbar\omega}{k_B T}} - 1}$ from Bose-Einstein distribution, where \hbar is Dirac constant, ω the phonon frequency, and k_B the Boltzmann constant. Subsequently, the change in f due to the radial temperature gradient is,

$$\delta f = -\tau v \left(\frac{\hbar\omega}{k_b T^2} \right) \frac{e^{\frac{\hbar\omega}{k_b T}}}{\left(e^{\frac{\hbar\omega}{k_b T}} - 1 \right)^2} \frac{\partial T}{\partial r} \quad (6.1)$$

The total heat flux due to the temperature gradient

$$\begin{aligned} q &= \int_0^{\omega_D} v \delta f \hbar\omega D(\omega) d\omega \\ &= \int_0^{\omega_D} v \left(-\tau v \left(\frac{\hbar\omega}{k_b T^2} \right) \frac{e^{\frac{\hbar\omega}{k_b T}}}{\left(e^{\frac{\hbar\omega}{k_b T}} - 1 \right)^2} \frac{\partial T}{\partial r} \right) \hbar\omega \left(\frac{\omega^2}{2\pi^2 v^3} \right) d\omega = -k_{th} \frac{\partial T}{\partial r} \end{aligned} \quad (6.2)$$

Where $D(\omega)$ is the density of states for the vibrational modes, and k_{th} is the thermal conductivity due to phonon transport. Consequently,

$$k_{th} = \int_0^{\omega_D} \left(\frac{\hbar^2 \omega^3}{2\pi^2 v k_b T^2} \right) \frac{e^{\frac{\hbar\omega}{k_b T}}}{\left(e^{\frac{\hbar\omega}{k_b T}} - 1 \right)^2} \tau d\omega \quad (6.3)$$

τ depends on phonon scattering processes, the three dominant ones being due to phonon-phonon, phonon-impurity interactions and boundary scattering. The phonon-phonon scattering that occurs due to interactions between vibrational modes can be classified as either normal (N) or Umklapp (U) scattering. N processes conserve the phonon momentum and hence contribute minimally to the thermal resistance (Maznev and Wright 2014). The wave vector conservation involves a reciprocal lattice vector in U processes and effects changes in the momentum resulting in a resistance to thermal transport (Maznev and Wright 2014). Literature suggests that at low temperatures, only N scattering is prevalent (Holland 1963; Z. Zhu et al. 2013), as temperature increases both scattering mechanisms contribute to the heat conduction through the nanoparticle. Boundary scattering, predominantly noted for characteristic system geometries that are smaller than phonon mean free path for the material, occurs due to differences in lattice vibrational frequencies at interfaces.

The τ approximation proposed by Klemens and Callaway is rooted to Matthiessen's rule (Matthiessen and Vogt 1864), by summing the contributions due to phonon-phonon scattering, phonon-impurity scattering and boundary effects, respectively. While both models consider only longitudinal modes for heat conduction, the Klemens model ignores the N scattering as reflected from the first terms of their respective expressions for τ shown below.

$$\tau_{klemens}^{-1} = A_k T \omega^2 e^{-\frac{B_k}{T}} + C \omega^4 + \frac{v_b}{d} \quad (6.4)$$

$$\tau_{callaway}^{-1} = (B_1 + B_2) T^3 \omega^2 + C \omega^4 + \frac{v_b}{d} \quad (6.5)$$

Here, v_b is the average phonon velocity derived from the transverse (v_T) and longitudinal (v_L) components as $v_b^{-1} = \frac{1}{3}[2v_T^{-1} + v_L^{-1}]$, and d is the particle dimension. The Holland formulation incorporates, on one hand, both N (for low and high temperatures) and U scattering (only for high temperatures) mechanisms, and on the other hand the individual contributions of longitudinal and transverse acoustic modes to k_{th} are also accounted for.

$$\tau_T^{-1} = B_T T^4 \omega + C \omega^4 + \frac{v_b}{d} + \tau_{TU}^{-1} \quad (6.6)$$

Where the Umklapp relaxation component,

$$\tau_{TU}^{-1} = \begin{cases} 0, \theta < \theta_1 \\ B_{TU} \omega^2 / \sinh(\omega), \theta \geq \theta_1 \end{cases} \quad (6.7)$$

$$\tau_L^{-1} = B_L T^3 \omega^2 + C \omega^4 + \frac{v_b}{d} \quad (6.8)$$

$$k_{th} = k_T + k_L = \frac{2}{3} \int_0^{\omega_2} \left(\frac{\hbar^2 \omega^3}{2\pi^2 v_T k_b T^2} \right) \frac{\frac{\hbar \omega}{e^{k_b T}}}{\left(\frac{\hbar \omega}{e^{k_b T}} - 1 \right)^2} \tau_T d\omega \quad (6.9)$$

$$+ \frac{1}{3} \int_0^{\omega_3} \left(\frac{\hbar^2 \omega^3}{2\pi^2 v_L k_b T^2} \right) \frac{\frac{\hbar \omega}{e^{k_b T}}}{\left(\frac{\hbar \omega}{e^{k_b T}} - 1 \right)^2} \tau_L d\omega$$

The integral range for the frequencies is substituted to corresponding temperatures by $\theta_i = \frac{\hbar\omega}{k_b}$. The parameters used in the calculations for k_{th} of the Si nanoparticle are listed in Table 6.1. The dimension of the nanoparticle being smaller than Si mean free path. Ballistic heat transfer and scattering due to boundary collisions are anticipated to be predominant. We use the Mathematica 10.4 (Inc. 2016) package to perform the integrations numerically.

Table 6.1 *The input and fitting parameters for crystalline silicon required to predict thermal conductivity using Klemens, Callaway and Holland formulations of the Boltzmann transport equation are listed.*

Parameter	Value	Parameter	Value
$\theta_1 (K)$	1.80×10^2 (Holland 1963)	$v_t (m/s)$	5.86×10^3 (Holland 1963)
$\theta_2 (K)$	2.10×10^2 (Holland 1963)	$v_l (m/s)$	8.48×10^3 (Holland 1963)
$\theta_3 (K)$	5.70×10^2 (Holland 1963)	$v_b (m/s)$	6.53×10^3
$\theta_D (K)$	6.58×10^2 (Holland 1963)	$B_T (K^{-4})$	7.50×10^{-14} (Z. Zhu et al. 2013)
$C (s^3)$	1.32×10^{-45} (Hopkins and Duda 2001)	$B_{TU} (s)$	7.80×10^{-18} (Z. Zhu et al. 2013)
$B_1 + B_2 (s/K^3)$	3.80×10^{-24} (Holland 1963)	$B_L (s)$	1.00×10^{-24} (Z. Zhu et al. 2013)
$A_k (s/K)$	1.23×10^{-19} (Holland 1963)	$d (nm)$	1.15×10^2
$B (K)$	1.40×10^2 (Hopkins and Duda 2001)	$\lambda_{mfp} (nm)$	3.00×10^2 (Ju and Goodson 1999)

6.3 Results and Discussion

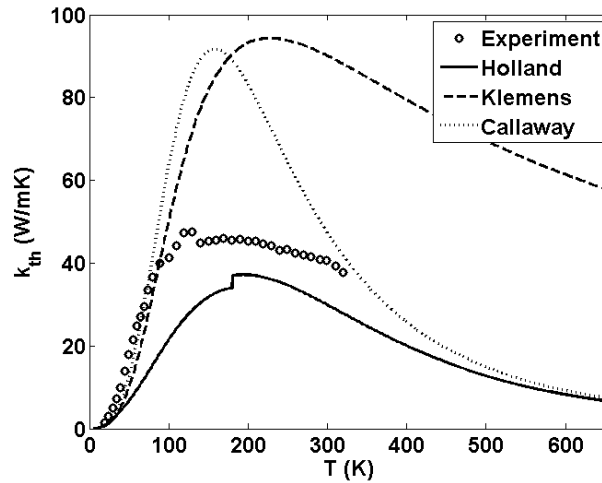


Figure 6.1 *Thermal conductivity predictions for a 115 nm silicon nanoparticle as a function of temperature as obtained from the Klemens, Callaway and Holland models based on the parameters listed in Table 1 are compared against experimental measurements in the literature (D. Li et al. 2003). While the Klemens model significantly overpredicts the thermal conductivities beyond the low temperature region, the Callaway model shows reasonable concurrence with experimental data at very low and at near room temperatures. The Holland model provides the best estimates for the thermal conductivity, with predictions within ~20% of the measured values.*

Fig 6.1 presents the k_{th} for the crystalline Si nanoparticle over a range of temperatures (5 – 658 K) as predicted from the different models in comparison to the experimental measurements. At room temperature, $k_{th} \approx 30.00, 48.00$ and 90.00 W/m.K, respectively, from the Holland, Callaway and Klemens formulations. The maximum k_{th} from the different models differ in magnitude as well as the temperature at which they occur: 91.65 W/m.K at 115 K (Callaway), 94.32 W/m.K at 125 K (Klemens) and 37.20 W/m.K at 200 K (Holland). The Klemens model only considers U processes as compared to Callaway and Holland models that incorporate both N and U scattering. However, the similar evolution of the Callaway and Klemens predictions at low temperatures suggests, as we describe later from Fig 6.2, that at low temperatures the relaxation times associated with the scattering processes considered in the two models are similar. As temperature increases, both models predict a maximum and then k_{th} decreases. The reduction, more pronounced for the Callaway model than the Klemens

formulation, is attributed to the phonon-phonon U scattering term. τ for U scattering as proposed by Callaway is dependent on T^{-3} while Klemens considered it to be proportional to T^{-1} . Since $k_{th} \propto \tau$, the Callaway prediction decays faster than the Klemens model estimates. The Holland model calculates results akin to Callaway and Klemens models for very low temperatures but deviates to a lower maximum k_{th} . The inclusion of the scattering effects due to transverse vibrational modes in addition to the longitudinal phonons, further reduces k_{th} in comparison to the Callaway model calculations. However, as temperature increases, predictions from both the Holland and Callaway models converge. Holland considered only N type scattering at low temperatures, but like the Callaway model, incorporated both N and U processes above a threshold temperature (~ 180 K for Si). We corroborate that thermal transport in the nanoparticle is predominantly by longitudinal modes at high temperatures because of the strong agreement in the results from the two models above the Debye temperature (~ 658 K) for Si.

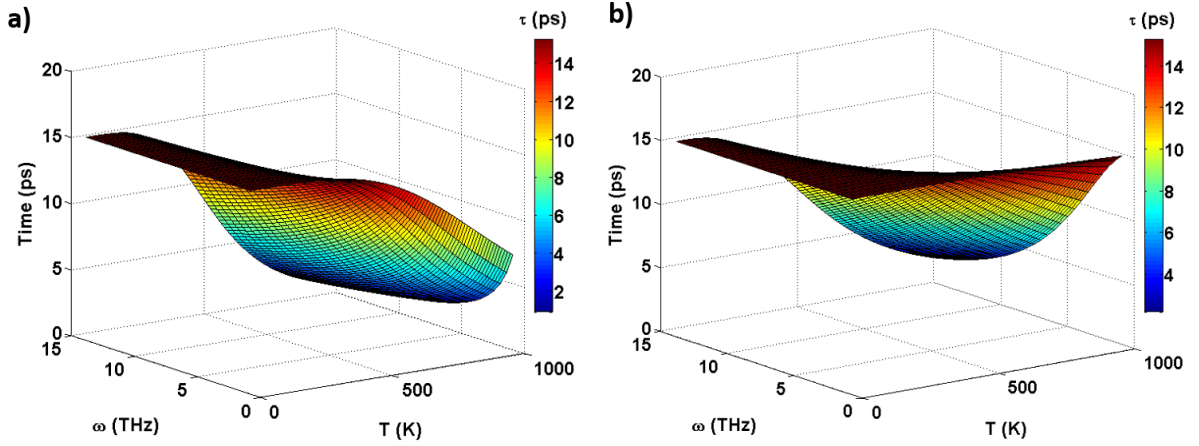


Figure 6.2 The variation of the relaxation time (τ) as a function of temperature (T) and vibrational frequencies (ω) are illustrated for the (a) transverse acoustic (TA) and the (b) longitudinal acoustic (LA) modes used in the Holland formulation of the Boltzmann transport equation. While the effect of T on relaxation time is weak at low temperatures, τ decreases significantly with increasing temperature for higher T values.

The predictions from all the three models show good agreement for macroscopic structures (Hopkins and Duda 2001). However, as presented in Fig 6.1, the experimental k_{th} measurements for nanostructures differ from model estimates: for instance, in case of a Si

nanowire, a maximum $k_{th} = 45.00 \text{ W/m.K}$ is recorded at 140 K, while near room temperature ($\sim 300 \text{ K}$) $k_{th} = 38.00 \text{ W/m.K}$ (Ju and Goodson 1999). Results from the Holland, Callaway and Klemens models differ from the experimental data by $\sim 20\%$, 40% and 250% , respectively, at room temperature. Again, including effects of phonon scattering processes due to both transverse (TA) and longitudinal (LA) acoustic modes improves the predictive accuracy of Holland model relative to the other formulations. This observation asserts that for nanoscale materials both longitudinal and transverse modes influence k_{th} , especially at low temperatures.

Fig 6.2 shows the variation of τ with temperature and vibrational frequencies for (a) TA, and (b) LA modes. As Fig 6.2.a shows, τ for the TA modes reduces with temperature while persists with a relatively constant value for changes in the vibrational frequencies except for high temperatures. Thus, the contribution of k_T to the overall k_{th} is notable at low temperatures but gradually diminishes as the nanoparticle becomes hotter. τ for LA modes remains constant with temperature for low frequencies, as presented in Fig 6.2.b, and reduces rapidly with increasing T for high frequency modes. At low temperatures, both modes display negligible τ variations with T , which leads to the similar increases in k_{th} from all the three models, as noted previously in Fig 6.1. The τ dependence on T become significant at high temperatures, causing k_{th} to achieve a maximum and then decay. Above 500 K, τ due to the TA modes is smaller relative to the LA phonons, implying that longitudinal modes become the predominant contributor to k_{th} at high temperatures, as reflected earlier from Fig 6.1.

6.4 Conclusion

In summary, we compare three different approaches to solving the BTE for predicting thermal conductivity of a spherical Si nanoparticle across a wide temperature range. The predictions from the Klemens, Callaway and Holland models revealed a close agreement at low temperatures but deviated significantly with increasing T . The T^{-3} dependence of the relaxation time in the Callaway model contributes to a steeper decay in k_{th} values relative to

that observed in the Klemens formulation where $\tau \propto T^{-1}$. Results from the Holland model are in strong agreement with experimentally measured k_{th} due to the consideration of both transverse and longitudinal vibrational modes, and the incorporation of N (normal) scattering at low temperatures, and both N and U (Umklapp) processes for higher T values. Analyses of the relaxation time for the longitudinal and transverse acoustic modes suggests that τ decreased insignificantly at low T but the reduction is more pronounced at higher temperatures. Thus, k_{th} increase for low temperatures is similar for all the models, while decrease is faster as per Holland model for a hotter nanoparticle due to the consideration of longitudinal modes of phonon transport. The inference of longitudinal phonon mode dominance in thermal transport at high temperatures show strong concurrence with prior experimental results. Therefore, for high temperature manufacturing applications of silicon nanoparticle, the consideration of thermal diffusion based of longitudinal phonon scattering is crucial for a stable thermal design.

CHAPTER 7. THERMO-MECHANICAL ANALYSIS OF BRUSHLESS DC MOTOR FOR APPLICATION OF BONDED PERMANENT MAGNETS

7.1 Introduction

A novel methodology to reduce the waste critical materials and lower the permanent magnet price-point is to reuse the material wasted during manufacturing operations like cutting, machining. Additive manufacturing (AM) being the trending technology in fabrication and rapid-prototyping is well-suited to fabricate magnets involving expensive and critical rare-earth elements. By avoiding the losses in subtractive manufacturing, like machining wastes, AM exhibits advantages in reduced materials waste and energy consumption, with benefits of no machining tooling required and low labor cost, etc. In field of magnetic AM process, 3D printing technology by extrusion process is still in-developmental stage. Alternative manufacturing technologies such as laser metal printing has been utilized to rapidly synthesize Fe-Co magnets with varying compositions, enabling fast assessment of magnetic properties of this binary system (Geng et al. 2016). Recent works on extrusion printing of NdFeB bonded magnets have been explored (Huber et al. 2016; L. Li et al. 2017). In the work by Li et al (L. Li et al. 2017), the melt-extrusion process using the Big Area Additive Manufacturing (BAAM) system demonstrated a superior methodology in fabrication of bonded magnets with comparable magnetic and mechanical as-of standard injection molding methods.

Electric machine drives are the back-bone to the global energy, transportation and economic architecture. The ability to convert mechanical output to electrical energy and vice-versa provide the electric machines a unique ability to be integrable with almost every possible technological innovation from the smallest household device to the largest industrial scale apparatus. Electric machines and drives broadly include motors, generators, and actuators. There have been several research models and experimental prototypes covering the design aspect of electric machine drives based upon the application requirements. Among the three-broad

classification, electric motors are the most integrated machine, ranging from micro-dental motors, household hair-dryer and coffee grinder, to larger scale motors for electric vehicles and construction machines. The conception and testing of electric motors before commercialization is key towards an efficient design. Numerical methods including finite element analysis and resistive reduced-order models are two approaches used to design electric machines prior to prototyping and testing. There have been several finite element model of electric motor reports over the past two decades, since the revolution of computational techniques.

The brushless permanent magnet machines (BPM) is one of the highest torque density electrical machinery (Popescu et al. 2013). In the last three decades, the development and manufacturing of BPMs have seen a very significant interest from various industrial fields: water pumping systems, hybrid and electric vehicles, renewable energy generation, aerospace, home appliances, etc. Theoretically seen as an everlasting source of energy within the electrical machine system, the permanent magnet materials may be irreversible demagnetized and hence losing energy due to the thermal stress and high faulty electrical loads. The thermal stress on the permanent magnets occur due to the losses dissipated in the machine. To protect the permanent magnets thermally, it is necessary to mitigate the thermal losses as the induced eddy-currents losses in the magnet blocks, or via an efficient cooling system. Depending on the application, cooling systems could be employed with natural convection, forced convection or radiation cooling. Thermal analysis of electric motors is generally regarded as a more challenging area of analysis than electromagnetic analysis in terms of the ease of constructing a model and achieving good accuracy. The study by Popescu et al. (Popescu et al. 2013) provide various approaches towards thermal management of the permanent magnet in BPM. The stator losses in BPMs are a function of current and stator winding resistance. The temperature affects both the required current for the motor to deliver an imposed output torque and the electrical resistivity of the material used to build the stator winding. The increase in winding temperature

gives an increase in copper resistivity. A solution for mitigating the proximity losses have been proposed by Wrobel et al. (Wrobel et al. 2014), in which twisted wires, winding arrangement with flat rectangular wire placed along the slot leakage-flux lines, reduced slot fill factor with copper wires pushed within the slots further away from the slot opening region. Iron losses are also a dominant phenomenon in thermal generation. Typically for 100°C temperature rise, NdFeB magnets will lose 11% of the magnetic flux, SmCo magnets will lose 3% magnetic flux and ferrite magnets will lose 20% magnetic flux. For an improved thermal removal from the system, materials with higher thermal conductivity, having forced convection with high heat transfer coefficient or using materials with high emissivity and a good view factor should be considered. For the submersible pump system water cooling would be ideal with liquid forced convection ($h = 50 - 20000 \left(\frac{W}{m^2K} \right)$).

The structural and mechanical stability of submersible pump motors depend on the balancing of the generator shaft, the dynamic loading, material characterization and design of the system. The balancing and dynamic loading depend on the distribution of mass along the motor assembly. An unbalanced system would deflect during operation causing an oscillating motion during operation. This would induce fatigue loading due to variable torsion and bending loads in the motor shaft. Materials like certain grades of steel (preferably low carbon) have a higher fatigue life due to their high strength characteristics. Therefore, a balanced design of the PM motor would be advisable for such applications.

In the current work, a 3D model of a 20 W brushless DC (BLDC) surface mounted permanent magnet (SPM) motor for submersible water pump application was developed based on an existing design (Lee and Jung 2012). The application of the novel 3D printed bonded magnets were tested with the objective to reduce critical material utilization. The electromagnetic and thermo-mechanical performance analysis was performed using finite element analysis to predict feasibility of design under operating conditions. Linear definition

of unaligned, anisotropic bonded Nd-Fe-B permanent magnets was used. The magnets were obtained from Magfine and contain 65 vol% loading of Nd-Fe-B blended in nylon.

7.2 Magnet Model

A 20W BLDC motor model with surface mounted permanent magnet was developed to test the performance of the 3D printed bonded NdFeB magnets. The magnets were printed in Oakridge National Laboratory, and test for the magnetic properties in collaboration with Ames Laboratory. The starting material for the BAAM printed magnets were obtained from Magfine and different blends of magnetic sample were tested based on the volume fraction of magnetic powder in Nylon-12 matrix. Two different compositions were analyzed including 65 vol.% and 40 vol.% bonded magnets to test the performance in the 20W SPM BLDC motor.

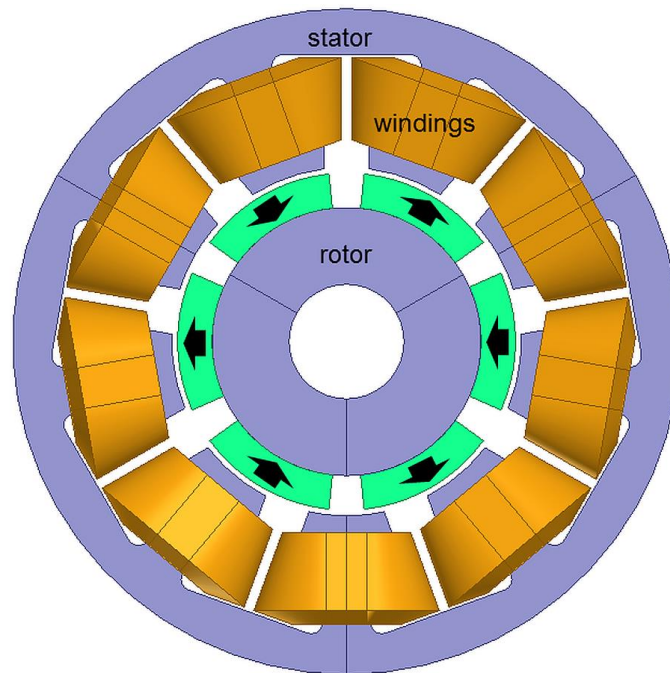


Figure 7.1. 3D FEA model for a 20W SPM Brushless DC motor.

The 3D illustration of the 20W BLDC motor (Fig 7.1) represents a 6-pole/9-slot electric motor designed to be used for a submersible pump application. The stator is located on the outside and is fixed to the casing of the motor. The shaft is mounted through the rotor and held into the casing using roller bearings. The coils are excited by a 3-phase AC current with $I_{rms} = 9 A_{rms}/turns$ and a supply voltage of $V = 2.22 V$ flowing through the coils. Anisotropic

bonded NdFeB magnets were used as the permanent magnets for the rotor. The following specifications were observed for the design of the motor, represented in Table 7.1.

Table 7.1 *Design parameter for 20W BLDC motor.*

Specification	Value
Rated Power (W)	20
Rated Torque (mNm)	0.1195
Rated Speed (rpm)	3,600
Outer Stator Diameter (mm)	58.07
Inner Stator Diameter (mm)	30.4
Outer Rotor Diameter (mm)	29.4
Inner Rotor Diameter (mm)	10
Airgap Length (mm)	0.5
Stack Length (mm)	7.3
Number of Slots	9
Number of Poles	6
Magnet Thickness (mm)	3
Magnet Volume (mm ³)	1,453
Magnet Remanence (T)	0.358
Magnet Coercivity (kA/m)	240
Magnet Material	Anisotropic bonded Nd-Fe-B

Under steady state condition, the torque/output power vs time was plotted for the motor model (Fig 7.2). Steady state torque ripples were observed in the analysis with maximum deviation within $\pm 0.5\%$ of the average torque/power. The ripples were not severe enough to be deteriorating to the performance of the motor and also would not produce enough noise as the motor would be placed underground. The average power output from the FEM analysis was predicted to be 19.5W with a mechanical efficiency of 98%.

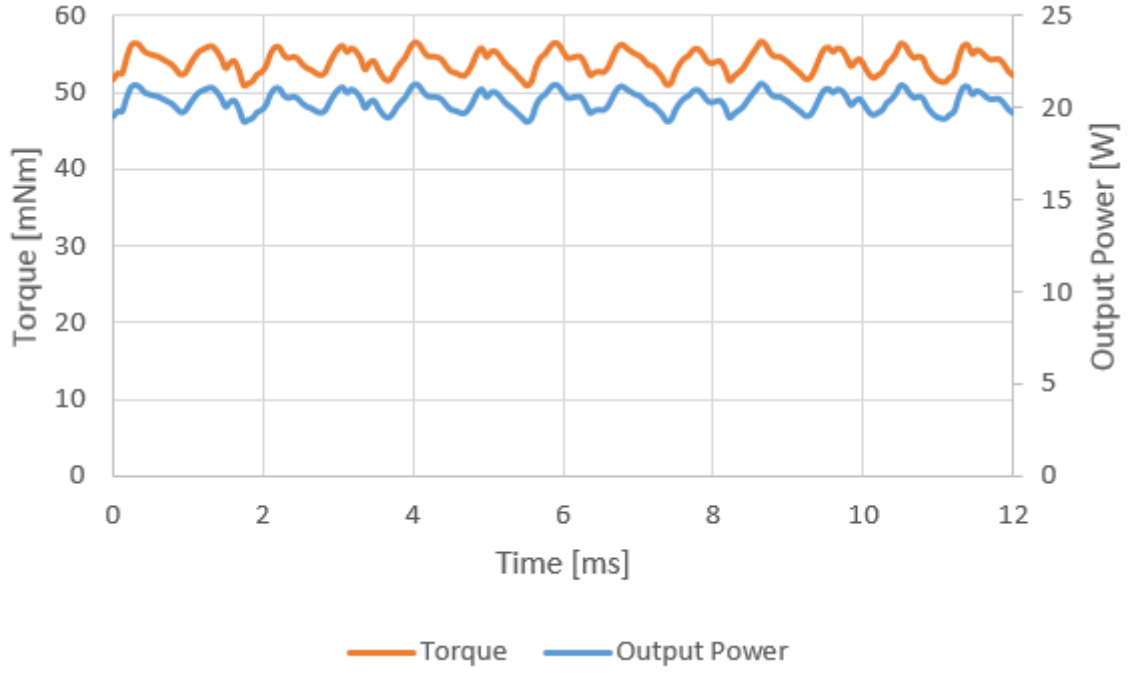


Figure 7.2 Torque/Output Power versus time for a 20W BLDC motor.

$$\eta_{mech} = \frac{P_{out}}{VI_{rms}} \quad (7.1)$$

A thermo-mechanical analysis was performed for the BLDC motor. Several modes of heat generation effect the thermal performance of electric motors including, ohmic loss (P_{ohmic}), hysteresis loss ($P_{hysteresis}$), and eddy current loss (P_{eddy}).

$$P_{ohmic} = I^2 R_{coil} \quad (7.2)$$

$$P_{hysteresis} = \eta B_{max}^n f \forall \quad (7.3)$$

$$P_{eddy} = K_e B_{max}^2 f^2 t^2 \forall \quad (7.4)$$

Where, R_{coil} is the coil resistance, η is the hysteresis coefficient, B_{max} is the maximum flux density, n is the Steinmetz exponent, f is the frequency of magnetic reversal, \forall is the volume of magnetic material, K_e is the eddy current constant, and t is the thickness of the material. The Ohmic loss is the most dominant mode of heat generation in motors because of the high current flowing through the copper coils. Hysteresis and eddy current losses are not very dominant depending on the selection of good electrical steel laminates. The hysteresis loss occurs due to energy released from the cyclic magnetization and demagnetization of the core

material. The eddy current losses are skin effect and occur when the cyclic magnetization causing induced-emf generate a whirlpool of current inside the coils and core.

A thermal diffusion model was applied in tandem with the electromagnetic module to simulate the steady state operating temperature for the motor. Considering the difference in magnitude of the time scale between electromagnetic and thermal problem, a two-step thermo-electromagnetic coupling was applied. The electromagnetic solution was first simulated at room temperature and the temperature was predicted based on the thermal diffusion model. This temperature was used to reevaluate all the material properties and electromagnetic followed by thermal model was simulated to predict the steady state temperature for the motor.

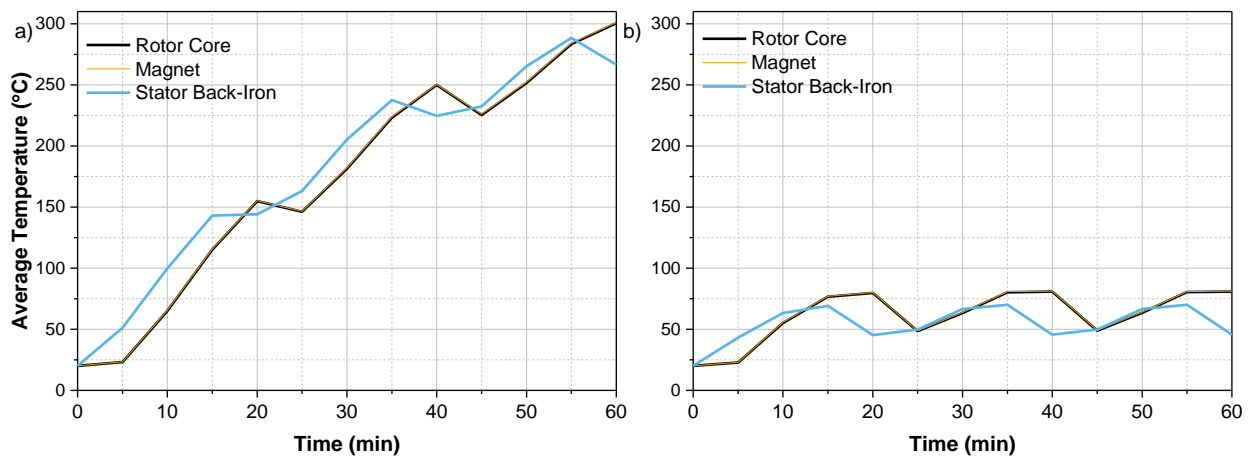


Figure 7.3. Thermal profile over 1 hour of operation of a 20W BLDC motor, a) Initial design, natural convection; b) Initial design with forced water cooling, and revised low current density design with natural convection.

The coupled thermo-electromagnetic simulations were performed over an operating period of one hour for the battery (Fig 7.3). With the initial design, the motor was simulated with natural convection (Fig 7.3.a). The model predicted an increasing temperature profile reaching up till 300°C by the end of the hour. Such a temperature domain is not suited for operating a SPM motor as the polymer would melt much before this state, and even if the polymer lasted, NdFeB magnets have a Curie Temperature of 310°C. The model was simulated with forced water convection and also reducing the current density to $9 A_{rms}/turns$ with natural convection (Fig 7.3.b). In both cases the average steady state temperature observed was

70°C, which is acceptable for an electric motor. Hence, the design was concluded safe to operate from a thermal perspective.

7.3 Material property prediction

Since, the bonded magnets were a new material concept, the experimental data covering all design aspects were not available. However, these materials being a polymer matrix composite, it was possible to predict the thermo-mechanical properties based on the volumetric mixing ratio of the particulate and matrix phases. The first analysis was designed based on Hashin-Shtrikman formulation of upper and lower limits for material properties of a composite material (Hashin and Shtrikman 1962). The following formulation was used for prediction of the thermal conductivity bounds for the bonded magnets:

$$k^- = \frac{k_m k_p + 2k_m(k_m \phi_p + k_p \phi_m)}{2k_m + k_m \phi_m + k_p \phi_p} \quad (7.5)$$

$$k^+ = \frac{k_m k_p + 2k_p(k_m \phi_p + k_p \phi_m)}{2k_p + k_m \phi_m + k_p \phi_p} \quad (7.6)$$

Where, k^- and k^+ are the effective bounds of thermal conductivity for a composite material with properties of the matrix phase represented by k_m and that of the dispersed (particulate) phase represented by k_p . The volume fraction of the dispersed phase is ϕ . The average properties of the two bounds were compared against an empirical model by Guth and modified by Gold (Guth and Gold 1938).

$$k = k_m(1 + 2.5\phi + 14.1\phi^2) \quad (7.7)$$

The following data was considered for Nylon-12 as the matrix and NdFeB as the dispersed phase: $k_m = 0.25 \frac{W}{mK}$ and $k_p = 9.0 \frac{W}{mK}$. Previous experimental studies have predicted that the Guth-Gold model follows very close to the experimentally observed property values. Another analysis was performed to predict the thermal conductivity of the bonded magnets using Miller bounds (Miller 1969).

$$\frac{k^+}{(k_m k_p)^{0.5}} = \frac{1 + \phi(\alpha - 1)}{\alpha^{0.5}} \left[1 - \frac{\phi(\alpha - 1)^2(1 - \phi)}{3 + [1 + \phi(\alpha - 1)][1 + \phi(\alpha - 1) + 3(\alpha - 1)(1 - 2\phi)G]} \right] \quad (7.8)$$

$$\frac{k^-}{(k_m k_p)^{0.5}} = \alpha^{0.5} \left[\alpha - \phi(\alpha - 1) - \frac{\frac{4}{3}\phi(\alpha - 1)^2(1 - \phi)}{[1 + \alpha + 3(\alpha - 1)(2\phi - 1)G]} \right] \quad (7.9)$$

Where, $\alpha = \frac{k_1}{k_2}$, such that $k_1 > k_2$ and $G = 1/9$ for spherical dispersed phase particles.

The predicted thermal properties are represented in Table 7.2.

Table 7.2 Model prediction results for thermal conductivity of 65 vol.% NdFeB.

Models	Thermal Conductivity [W/m-K]
Hashin-Shtrikman	1.369 – 5.120 (Avg:3.244)
Miller	1.659 – 4.186 (Avg:2.922)
Guth Gold	2.146

One-way coupling of the electromagnetic and mechanical/structural solution was performed using ANSYS Maxwell, ANSYS Workbench and ANSYS Mechanical to evaluate the stress field, deformation and strain in the rotor and stator components due to the Maxwell stress tensor generated from the current flux density (\mathbf{j}) interacting with the magnetic field (\mathbf{B}) of the motor. The force due to this stress field is represented as follows,

$$\mathbf{F}_{DC} = \frac{1}{2} \int (\mathbf{j} \times \mathbf{B}) dV \quad (7.10)$$

The force field in the 20W BLDC electromagnet model was evaluated in ANSYS Maxwell, considering no eccentricity existing in the in the rotor. Considering the given analysis is for a DC motor, the Maxwell forces are independent of time. The following materials were considered from the ANSYS Engineering Data for the following components,

Table 7.3 ANSYS mechanical model materials for 20W BLDC motor components.

Component	Material
Rotor	Structural Steel
Shaft	Structural Steel
Magnets	65 vol.% Nd-Fe-B in bonded magnet (user-defined)
Stator	Structural Steel
Air Box	Atmospheric Air
Coils	Copper Alloy

Observation of stress-strain data represented the magnets to be a soft material with low strength and but high toughness. The material did not seem brittle because brittle materials characteristically do not show plastic yielding and/or strain hardening. The low strength of the material could be a challenge in design as these would not be able to handle heavy loading. Fig. 7.4 shows the force magnitude change over time in the motor. The average force was estimated to be 8 N over the duration of 12ms of operation. The force was calculated from the Maxwell force formulation at each nodal point in the FEA and interpolated as a vector field over the entire motor domain. This force was created because the electric flux was not parallel to the magnetic field within the motor, leading to a force density in the material which would cause deformation of the stator and rotor components.

The equivalent von-mises stress profile in the stator and rotor are shown in Fig. 7.5. In the stator, the stress field was concentrated at the teeth of the stator acting as cantilever beams. In the rotor, the stress was localized to the interface between magnets and rotor surface, which could cause debonding under critical loading.

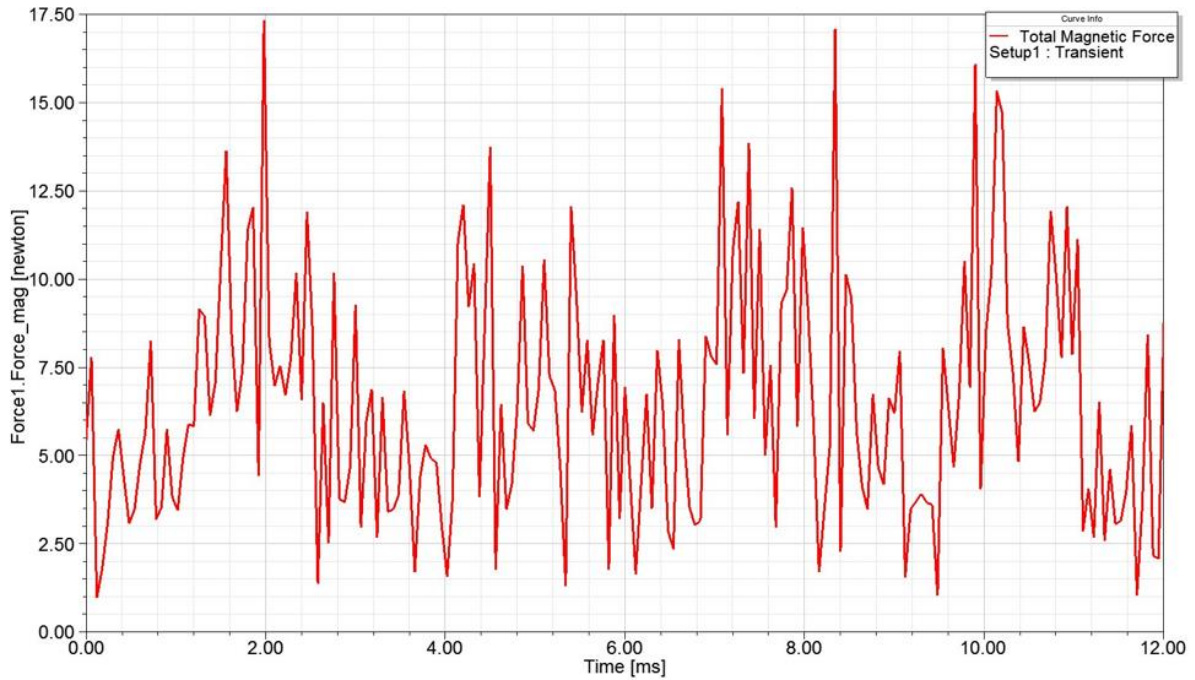


Figure 7.4. Force profile over 1 cycle operation of 20W BLDC motor.

The magnitude of maximum stress in the stator and rotor were 0.2 MPa and 0.8 MPa respectively, which were considerably less than the yield strength of steel (400MPa) and bonded magnets (6.1 MPa). In conclusion, the design is safe in operation and would not fail mechanically.

The low stress profile causes negligible deformation in the material. The maximum equivalent strain in the stator and rotor were $1.07 \times 10^{-4} \%$ and $1.84 \times 10^{-3} \%$ respectively. Such low strains would cause negligible degree of deformation, implying a safe design. In the rotor, the strain was localized only to the magnets because of the low elastic modulus of the 65 vol.% Nd-Fe-B magnets compared to the structural steel for the body of the rotor. This strain difference would cause localized stress generation (as observed from the stress profile) and could lead to debonding of the magnets from the rotor surface in extreme cases.

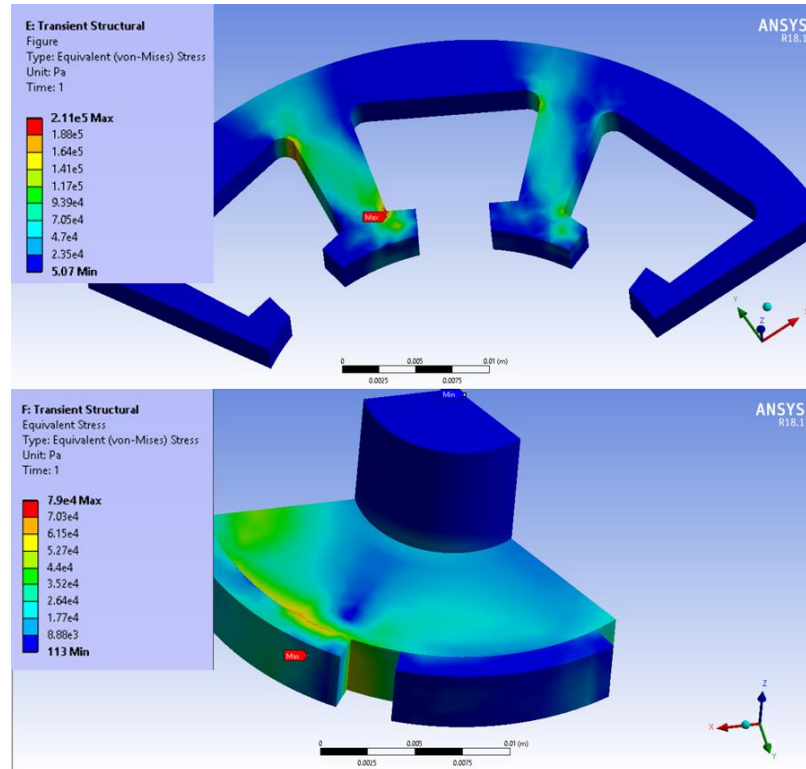


Figure 7.5. Von-mises stress contour for 20W BLDC motor, a) stator armature; b) rotor with magnets.

7.4 Conclusion

A 20W BLDC motor was modeled using FEA to simulate the thermo-mechanical and electromagnetic performance of the motor under operating conditions. The novel bonded magnet technology was implied as the surface mounted permanent magnets for the motor. A 3D FEA model was simulated to test the electromagnetic performance of the magnetic material and the motor was found to be 98% efficient. The thermal performance predicted the possibility of a meltdown upon operation necessitating the need to redesign the coils for lower current density. A steady state temperature of 70°C was predicted under passive cooling. The thermal conductivity of the material was predicted using first principle techniques for composite material. The mechanical performance analysis concluded that the motor was mechanically safe in design. Considering the thermo-mechanical performance of the motor, the design was approved for prototyping.

7.5 Appendix

The motor being approved to be a safe design was considered for prototyping. The laminate sheet design for the stator and rotor was done in AutoCad. Rotor and stator laminations were cut, stacked and bonded from Polaris Laminations using silicon steel M19 26-gauge laminates (Fig 7.6.a). The casing model was made using Solidworks and prototyped from Boyd Lab (Fig 7.6.b). The motor assembly and testing were not completed considering the end of the first five years plan for the CMI and the commencement of the Phase 2 with different targeted responsibilities.

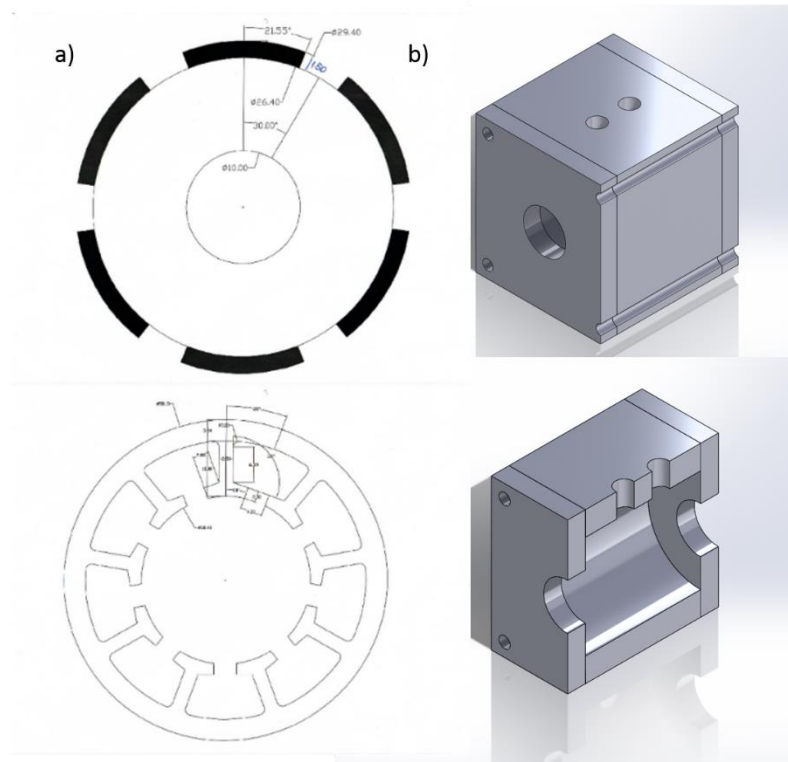


Figure 7.6 Motor prototyping, a) Design of stator and rotor laminates; b) Design of the motor casing.

CHAPTER 8. CONCLUSION AND FUTURE SCOPE

8.1 Summary and Conclusions

Summarizing the work done for the doctoral thesis, multiphysics thermo-mechanical models were developed, to analyze the performance, material property prediction, and life and degradation mechanisms, primarily for electrochemical systems with extension towards electromagnetic machines. A thermo-chemo-mechanical model was developed to simulate the lithiation of electrode particles in a lithium-ion battery. The stress model was capable of predicting the elastic and plastic stress regimes during lithiation for different rates of charging. The thermal heat generation model was able to predict the heat generation in electrode materials from four different heating mechanisms including, polarization heating, entropic heating, joule heating and heat generated from plastic strain energy. The chemical model was developed to predict the cycle life degradation for lithium-ion batteries due to SEI formation. The multiphysics models for stress, thermal and chemical degradation were coupled to predict the performance of lithium batteries under different operating conditions. An extension of the thermo-mechanical analysis was performed for electromagnetic systems, targeted towards brushless DC motors to test the application for novel bonded permanent magnets.

The chemo-mechanical model was developed to solve a coupled mass transfer equation for evaluating the time-dependent growth of lithium-ion concentration in the electrode particle. An elastic-perfectly plastic deformation was considered to model the stress state of the particle during (de)lithiation. A closed form solution of the stress profile was formulated based upon the lithium-ion concentration in the particle. A set of five material indices were developed to account for the effect of elastic and plastic stresses on the charging capacity and mechanical stability of the electrode material. The stress formulation was used to evaluate the stress field in a fully lithiated LMO particle during discharge at 2C and 3C rates of charging. The growth of the plastic regime and its effect on the stress field near the core of the particle was analyzed.

It was found that higher plastic deformation causes the core to be under a tensile hydrostatic stress of magnitude several times the yield strength of the material. Since the stress state is hydrostatic and the material was assumed to be solid, with no cracks, the core of the particle was under no deformation. In conclusion, the presence of microcracks or voids near the particle center under such high tensile stress fields would cause void coalescence, leading to crack formation and failure of the particle over multiple charging cycles. The material selection based on mechanical stability was developed from these coupled chemo-mechanical equations. The five indices were used to compare six candidate electrode materials by comparing their charging capacity and mechanical toughness under the condition of elastic and plastic deformation. It was found that LMO/graphite as electrode materials have excellent mechanical stability and fracture resistance under elastic loading. However, when considering plastic deformation, LFP/silicon electrodes could handle large deformations making them suitable for high voltage and faster charging applications.

The thermo-mechanical model evaluated the heat generation by six candidate electrodes based on four heating mechanisms. Apart from the three well-known heating sources, i.e. polarization, entropic and joule, a fourth heating source was formulated from the plastic strain energy during large deformation of the electrode particle. The strain energy stored when a material deforms plastically is partly dissipated in the form of heat generation. Apart from the joule heating source, LFP/silicon was found to generate the least heat among all other electrode materials compared in this analysis. Due to the high resistivity of LFP electrodes, they generate higher joule heat, which could be controlled by coating them with conducting filler material. The material comparison showed that LCO and graphite electrodes generate a large amount of heat during operation, while LFP and silicon were good choices for a thermally stable design. Finally, comparison of the total heat generated by the electrode materials over multiple rates of charging lead to the inference that LFP electrodes are suitable

for low rates of charging ($C < 4$) and LMO are suitable for high rates of charging application.

A novel method was developed for predicting the mechanical response for separator membrane under compression. The model assumed the an open-cell foam architecture for the separator and was used to model the variation of ionic conductivity under compressive load. Five different separator materials were simulated with three types of lithium battery including LCO/C, LMO/C and LFP/C cells. The thermal profile was simulated under different rates of charging, compressive load and cooling characteristics. Thermal contour plots were presented as a design guide towards prediction of safe zones of operation for structurally safe lithium cells.

A chemical reduced-order degradation mechanism was developed to predict the capacity fading in lithium-ion cells due to SEI formation. The model was validated against experimental data for LCO/C cell (C. Hu et al. 2014) and LFP/C cell (P. Liu et al. 2010). Two charge profiles were compared to predict the fading tendency under different charging protocols. It was concluded that charging the battery up till full capacity would be more detrimental towards the cycle life of the battery. A novel concept of battery ageing was introduced. The reduction in the effective capacity fade for aged battery was observed from the capacity analysis. A chemo-economic analysis was performed to create a design guide for aged lithium-ion battery by comparing the capacity benefit of ageing the cell against the cost of ageing the battery. The targeted market of aged lithium battery could be implied for biomedical and EV applications, where battery replacement is costlier than aged battery.

A brief work on the use of Boltzmann Transport Equation to predict the thermal conductivity of silicon nanoparticles over a range of temperature. Three different models were used to compare the predicted results against experimental data. The predictions by the Holland model were found to be in strong agreement with experimentally measured k_{th} due to the consideration of both transverse and longitudinal vibrational modes, and the incorporation of

N (normal) scattering at low temperatures, and both N and U (Umklapp) processes for higher T values.

Finally, a 3D FE thermo-mechanical and electromagnetic coupled model was developed for a 20W BLDC motor to test the application of bonded NdFeB magnets. The model was redesigned to have a 98% efficient motor with a predicted power output of 19.5W and steady state operating temperature of 70°C with passive cooling. The thermal conductivity of the bonded magnets was predicted using first principle analysis for polymer composite matrix. The mechanical analysis predicted that the maximum stress was concentrated in the magnet/rotor junction. However, the stress magnitude was 0.2MPa, which would not cause delamination of the magnet from the rotor. The motor was considered for prototyping to test the performance upon completion of the coupled FEM.

In conclusion, multiphysics analysis was performed for electrochemical and electromagnetic system in order to predict operating performance, feasibility, life and optimum material properties under different operating conditions. The works could be applied to model the motor and battery unit for an EV application.

8.2 Future Work

A tremendous amount of research, both theoretical and experimental, have been dedicated towards the development and study of lithium-ion battery systems over the decade. There has been a massive undertaking towards the synthesis of better energy storing electrodes which can be thermally and mechanically robust under fast charging and heavy loading conditions. From a theoretical perspective, several models have emerged over the decade targeting to simulate the operation of lithium-ion batteries in real-world application. There are several elastic-based and purely plastic-based stress-driven diffusion models. Our work incorporates a combined elasto-plastic thermo-chemo-mechanical mathematical framework which could be applied to both perfectly plastic electrodes, like silicon, and elastic with some

plastically deforming electrodes like LMO and Si. Furthermore, our work on battery degradation due to SEI provides an efficient numerical scheme to predict capacity fade with high degree of accuracy. The material indices developed in this project provides a design guide for industry and scientists towards better design and selection of electrode materials depending upon the need of the application. Finally, our work on thermal profiling of pouch cells under compression is the commencement towards a new scope of structurally integrable lithium-ion battery system.

One of the several future scopes for this project is to integrate the structural battery work with the SEI and also incorporate lithium metal deposition (plating). Lithium plating is of tremendous interest in the present-day lithium technology as it severely deteriorates the battery performance when operating at very high rates of charging (or fast charging) or under colder atmospheric conditions. The future work would investigate the conditions causing lithium plating, the effect of pore-closure of the separator under stress on plating and the techniques to mitigate the condition. A suite of experiments would be needed to support the modeling, to be able to generate an understanding of the physics behind dendritic growth (or lithium plating). Another future project could be the analysis of the conditions causing SEI film fracture and reformation leading to faster capacity fade. The future aim is to obtain an integrated module of mathematical frameworks that could predict the chemo-thermo-mechanical performance and degradation of lithium-ion battery under most operating conditions.

REFERENCES

- Armand, Michel, and J. M. Tarascon. 2008. "Building Better Batteries." *Nature* 451 (7179). Nature Publishing Group: 652.
- Arora, Pankaj, and Zhengming Zhang. 2004. "Battery Separators." *Chemical Reviews* 104 (10): 4419–62. doi:10.1021/cr020738u.
- Ashby, Michael F. 2005. "Materials Selection in Mechanical Design." *MRS Bull* 30 (12): 995.
- Aurbach, D., B. Markovsky, M. D. Levi, E. Levi, A. Schechter, M. Moshkovich, and Y. Cohen. 1999. "New Insights into the Interactions between Electrode Materials and Electrolyte Solutions for Advanced Nonaqueous Batteries." *Journal of Power Sources*. doi:10.1016/S0378-7753(99)00187-1.
- Bach, S, J P Pereira-Ramos, N Baffier, and R Messina. 1992. "Thermodynamic Data of Electrochemical Lithium Intercalation in LiMn_2O_4 ." *Electrochimica Acta* 37 (7). Elsevier: 1301–5.
- Baek, K. W., E. S. Hong, and S. W. Cha. 2015. "Capacity Fade Modeling of a Lithium-Ion Battery for Electric Vehicles." *International Journal of Automotive Technology*. doi:10.1007/s12239-015-0033-2.
- Baksa, Steven, and William Yourey. 2018. "Consumer-Based Evaluation of Commercially Available Protected 18650 Cells." *Batteries* 4 (3). Multidisciplinary Digital Publishing Institute: 45.
- Baldwin, Richard S, William R Bennett, Eunice K Wong, MaryBeth R Lewton, and Megan K Harris. 2010. "Battery Separator Characterization and Evaluation Procedures for NASA's Advanced Lithium-Ion Batteries." *Nasa/Tm*, no. NASA/TM-2010-216099: 1–59.
- Barai, P., K. Smith, C.-F. Chen, G.-H. Kim, and P. P. Mukherjee. 2015. "Reduced Order Modeling of Mechanical Degradation Induced Performance Decay in Lithium-Ion Battery Porous Electrodes." *Journal of the Electrochemical Society*. doi:10.1149/2.0241509jes.
- Bazinski, S J, and X Wang. 2014. "The Influence of Cell Temperature on the Entropic Coefficient of a Lithium Iron Phosphate (LFP) Pouch Cell." *Journal of The Electrochemical Society* 161 (1). The Electrochemical Society: A168--A175.
- Berla, Lucas A, Seok Woo Lee, Yi Cui, and William D Nix. 2015. "Mechanical Behavior of Electrochemically Lithiated Silicon." *Journal of Power Sources* 273. Elsevier: 41–51.
- Bernardi, D, E Pawlikowski, and John Newman. 1985. "A General Energy Balance for Battery Systems." *Journal of the Electrochemical Society* 132 (1). The Electrochemical Society: 5–12.
- Blomgren, George E. 2017. "The Development and Future of Lithium Ion Batteries." *Journal of The Electrochemical Society* 164 (1). The Electrochemical Society: A5019--A5025.
- Boltzmann, Ludwig. 1872. "Weitere Studien Über Das Wärmegleichgewicht Unter Gasmolekülen." *Kinetische Theorie II*, 115–225. doi:10.1017/CBO9781139381420.023.

- Bower, Allan F. 2009. *Applied Mechanics of Solids*. CRC press.
- Breitfuss, Christoph, Wolfgang Sinz, Florian Feist, Gregor Gstrein, Bernhard Lichtenegger, Christoph Knauder, Christian Ellersdorfer, et al. 2013. "A 'Microscopic' Structural Mechanics FE Model of a Lithium-Ion Pouch Cell for Quasi-Static Load Cases." *SAE International Journal of Passenger Cars - Mechanical Systems* 6 (2): 2013-01-1519. doi:10.4271/2013-01-1519.
- Broussely, M., S. Herreyre, P. Biensan, P. Kasztejna, K. Nechev, and R. J. Staniewicz. 2001. "Aging Mechanism in Li Ion Cells and Calendar Life Predictions." In *Journal of Power Sources*. doi:10.1016/S0378-7753(01)00722-4.
- "BU-205: Types of Lithium-Ion." 2017. *Battery University*. Accessed December 5. http://batteryuniversity.com/learn/article/types_of_lithium_ion.
- Callaway, J. 1959. "Model for Lattice Thermal Conductivity at Low Temperatures." *Physical Review* 113 (4): 1046–51. doi:10.1103/PhysRev.113.1046.
- Cannarella, John, and Craig B. Arnold. 2013. "Ion Transport Restriction in Mechanically Strained Separator Membranes." *Journal of Power Sources* 226: 149–55. doi:10.1016/j.jpowsour.2012.10.093.
- Cannarella, John, and Craig B. Arnold. 2014. "Stress Evolution and Capacity Fade in Constrained Lithium-Ion Pouch Cells." *Journal of Power Sources* 245: 745–51. doi:10.1016/j.jpowsour.2013.06.165.
- Chan, Candace K, Hailin Peng, Gao Liu, Kevin McIlwrath, Xiao Feng Zhang, Robert A Huggins, and Yi Cui. 2008. "High-Performance Lithium Battery Anodes Using Silicon Nanowires." *Nature Nanotechnology* 3 (1). Nature Publishing Group: 31.
- Chang, Jingbo, Xingkang Huang, Guihua Zhou, Shumao Cui, Peter B Hallac, Junwei Jiang, Patrick T Hurley, and Junhong Chen. 2014. "Lithium-Ion Batteries: Multilayered Si Nanoparticle/Reduced Graphene Oxide Hybrid as a High-Performance Lithium-Ion Battery Anode." *Advanced Materials (Deerfield Beach, Fla.)* 26 (5): 665. doi:10.1002/adma.201470028.
- Chen, C H, and K Amine. 2001. "Ionic Conductivity, Lithium Insertion and Extraction of Lanthanum Lithium Titanate." *Solid State Ionics* 144 (1–2). Elsevier: 51–57.
- Chen, L, F Fan, L Hong, J Chen, Y Z Ji, S L Zhang, T Zhu, and L Q Chen. 2014. "A Phase-Field Model Coupled with Large Elasto-Plastic Deformation: Application to Lithiated Silicon Electrodes." *Journal of The Electrochemical Society* 161 (11). The Electrochemical Society: F3164--F3172.
- Chen, Lian-Yi, Jia-Quan Xu, Hongseok Choi, Marta Pozuelo, Xiaolong Ma, Sanjit Bhowmick, Jenn-Ming Yang, Suveen Mathaudhu, and Xiao-Chun Li. 2015. "Processing and Properties of Magnesium Containing a Dense Uniform Dispersion of Nanoparticles." *Nature* 528 (7583): 539–43. doi:10.1038/nature16445.
- Chen, Man, Qiujuan Sun, Yongqi Li, Ke Wu, Bangjin Liu, Peng Peng, and Qingsong Wang. 2015. "A Thermal Runaway Simulation on a Lithium Titanate Battery and the Battery Module." *Energies* 8 (1). Multidisciplinary Digital Publishing Institute: 490–500.

- Christensen, John, and John Newman. 2006a. "A Mathematical Model of Stress Generation and Fracture in Lithium Manganese Oxide." *Journal of The Electrochemical Society* 153 (6). The Electrochemical Society: A1019--A1030.
- Christensen, John, and John Newman. 2006b. "Stress Generation and Fracture in Lithium Insertion Materials." *Journal of Solid State Electrochemistry* 10 (5). Springer: 293–319.
- Colclasure, Andrew M., Kandler A. Smith, and Robert J. Kee. 2011. "Modeling Detailed Chemistry and Transport for Solid-Electrolyte-Interface (SEI) Films in Li-Ion Batteries." *Electrochimica Acta*. doi:10.1016/j.electacta.2011.08.067.
- Dash, Ranjan, and Sreekanth Pannala. 2016. "Theoretical Limits of Energy Density in Silicon-Carbon Composite Anode Based Lithium Ion Batteries." *Scientific Reports* 6. Nature Publishing Group: 27449.
- Dawson, M. A., J. T. Germaine, and L. J. Gibson. 2007. "Permeability of Open-Cell Foams under Compressive Strain." *International Journal of Solids and Structures* 44 (16): 5133–45. doi:10.1016/j.ijsolstr.2006.12.025.
- Delp, Samuel A., Oleg Borodin, Marco Olguin, Claire G. Eisner, Joshua L. Allen, and T. Richard Jow. 2016. "Importance of Reduction and Oxidation Stability of High Voltage Electrolytes and Additives." *Electrochimica Acta*. doi:10.1016/j.electacta.2016.05.100.
- Deshpande, V.S., and N.A. Fleck. 2000. "High Strain Rate Compressive Behaviour of Aluminium Alloy Foams." *International Journal of Impact Engineering* 24 (3): 277–98. doi:10.1016/S0734-743X(99)00153-0.
- Dey, A. N. 1970. "FILM FORMATION ON LITHIUM ANODE IN PROPYLENE CARBONATE." *Journal of The Electrochemical Society*. doi:10.5194/bg-14-5727-2017.
- Doyle, Marc, Thomas F Fuller, and John Newman. 1993. "Modeling of Galvanostatic Charge and Discharge of the Lithium/Polymer/Insertion Cell." *Journal of the Electrochemical Society* 140 (6). The Electrochemical Society: 1526–33.
- Doyle, Marc, John Newman, Antoni S Gozdz, Caroline N Schmutz, and Jean-Marie Tarascon. 1996. "Comparison of Modeling Predictions with Experimental Data from Plastic Lithium Ion Cells." *Journal of the Electrochemical Society* 143 (6). The Electrochemical Society: 1890–1903.
- Ekstrom, H., and G. Lindbergh. 2015. "A Model for Predicting Capacity Fade Due to SEI Formation in a Commercial Graphite/LiFePO₄ Cell." *Journal of the Electrochemical Society*. doi:10.1149/2.0641506jes.
- Ellis, B L, K T Lee, and L F Nazar. 2010. "Positive Electrode Materials for Li-Ion and Li-Batteries." *Chemistry of Materials* 22 (3): 691–714. doi:10.1021/cm902696j.
- Etacheri, Vinodkumar, Rotem Marom, Ran Elazari, Gregory Salitra, and Doron Aurbach. 2011. "Challenges in the Development of Advanced Li-Ion Batteries: A Review." *Energy & Environmental Science* 4 (9). Royal Society of Chemistry: 3243–62.
- Fell, Christopher R, Danna Qian, Kyler J Carroll, Miaofang Chi, Jacob L Jones, and Ying Shirley Meng. 2013. "Correlation between Oxygen Vacancy, Microstrain, and Cation

- Distribution in Lithium-Excess Layered Oxides during the First Electrochemical Cycle.” *Chemistry of Materials* 25 (9). ACS Publications: 1621–29.
- Fong, Rosamaria. 1990. “Studies of Lithium Intercalation into Carbons Using Nonaqueous Electrochemical Cells.” *Journal of The Electrochemical Society*. doi:10.1149/1.2086855.
- Gabrisch, Heike, Rachid Yazami, and Brent Fultz. 2004. “Hexagonal to Cubic Spinel Transformation in Lithiated Cobalt Oxide TEM Investigation.” *Journal of The Electrochemical Society* 151 (6). The Electrochemical Society: A891--A897.
- Geng, J., I. C. Nlebedim, M. F. Besser, E. Simsek, and R. T. Ott. 2016. “Bulk Combinatorial Synthesis and High Throughput Characterization for Rapid Assessment of Magnetic Materials: Application of Laser Engineered Net Shaping (LENS™).” *JOM*. doi:10.1007/s11837-016-1918-x.
- Giancoli, Douglas C. 2008. *Physics for Scientists and Engineers with Modern Physics*. Pearson Education.
- Gioia, Gustavo, Yu Wang, and Alberto M. Cuitiño. 2001. “The Energetics of Heterogeneous Deformation in Open-Cell Solid Foams.” *Proceedings of the Royal Society A: Mathematical, Physical and Engineering Sciences* 457 (2009): 1079–96. doi:10.1098/rspa.2000.0707.
- Gong, L., S. Kyriakides, and W. Y. Jang. 2005. “Compressive Response of Open-Cell Foams. Part I: Morphology and Elastic Properties.” *International Journal of Solids and Structures* 42 (5–6): 1355–79. doi:10.1016/j.ijsolstr.2004.07.023.
- Goodenough, J. B., and Youngsik Kim. 2011. “Challenges for Rechargeable Batteries.” *Journal of Power Sources*. doi:10.1016/j.jpowsour.2010.11.074.
- Goodenough, John B., and Kyu Sung Park. 2013. “The Li-Ion Rechargeable Battery: A Perspective.” *Journal of the American Chemical Society*. doi:10.1021/ja3091438.
- Gor, G. Y., J. Cannarella, J. H. Prevost, and C. B. Arnold. 2014. “A Model for the Behavior of Battery Separators in Compression at Different Strain/Charge Rates.” *Journal of the Electrochemical Society* 161 (11): F3065–71. doi:10.1149/2.0111411jes.
- Gotcu, Petronela, and Hans J Seifert. 2016. “Thermophysical Properties of LiCoO₂--LiMn₂O₄ Blended Electrode Materials for Li-Ion Batteries.” *Physical Chemistry Chemical Physics* 18 (15). Royal Society of Chemistry: 10550–62.
- Guth, Eugene, and O Gold. 1938. “On the Hydrodynamical Theory of the Viscosity of Suspensions.” *Physical Review*. doi:10.1021/la001321r.
- Hallaj, S Al, R Venkatachalapathy, J Prakash, and J R Selman. 2000. “Entropy Changes Due to Structural Transformation in the Graphite Anode and Phase Change of the LiCoO₂ Cathode.” *Journal of the Electrochemical Society* 147 (7). The Electrochemical Society: 2432–36.
- Hashin, Z., and S. Shtrikman. 1962. “A Variational Approach to the Theory of the Elastic Behaviour of Polycrystals.” *Journal of the Mechanics and Physics of Solids*. doi:10.1016/0022-5096(62)90005-4.

- Hellwig, Christian, Seniz Sörgel, and Wolfgang G Bessler. 2011. "A Multi-Scale Electrochemical and Thermal Model of a LiFePO₄ Battery." *Ecs Transactions* 35 (32). The Electrochemical Society: 215–28.
- Hoang, Khang. 2014. "Understanding the Electronic and Ionic Conduction and Lithium Over-Stoichiometry in LiMn₂O₄ Spinel." *Journal of Materials Chemistry A* 2 (43). Royal Society of Chemistry: 18271–80.
- Holland, M. 1963. "Analysis of Lattice Thermal Conductivity." *Physical Review* 132 (6): 2461–71. doi:10.1103/PhysRev.132.2461.
- Hopkins, P E, and J C Duda. 2001. *Introduction to Nanoscale Thermal Conduction*. INTECH Open Access Publisher.
- Hu, Chao, Gaurav Jain, Puqiang Zhang, Craig Schmidt, Parthasarathy Gomadam, and Tom Gorka. 2014. "Data-Driven Method Based on Particle Swarm Optimization and k-Nearest Neighbor Regression for Estimating Capacity of Lithium-Ion Battery." *Applied Energy*. doi:10.1016/j.apenergy.2014.04.077.
- Hu, Yuhang, Xuanhe Zhao, and Zhigang Suo. 2010. "Averting Cracks Caused by Insertion Reaction In Lithium-Ion Batteries." *Journal of Materials Research* 25 (6): 1007–10. doi:10.1557/jmr.2010.0142.
- Huang, M, Z Suo, and Q Ma. 2002. "Plastic Ratcheting Induced Cracks in Thin Film Structures." *Journal of the Mechanics and Physics of Solids* 50 (5). Elsevier: 1079–98.
- Huber, C., C. Abert, F. Bruckner, M. Groenefeld, O. Muthsam, S. Schuschnigg, K. Sirak, et al. 2016. "3D Print of Polymer Bonded Rare-Earth Magnets, and 3D Magnetic Field Scanning with an End-User 3D Printer." *Applied Physics Letters*. doi:10.1063/1.4964856.
- Inc., Wolfram Research. 2016. "Mathematica 10.4." Champaign, Illinois: Wolfram Research Inc.
- Jin, S, T W Tang, and M V Fischetti. 2008. "Simulation of Silicon Nanowire Transistors Using Boltzmann Transport Equation under Relaxation Time Approximation." *Ieee Transactions on Electron Devices* 55 (3): 727–36. doi:10.1109/ted.2007.913560.
- Jin, Xing, Ashish Vora, Vaidehi Hoshing, Tridib Saha, Gregory Shaver, R. Edwin García, Oleg Wasynczuk, and Subbarao Varigonda. 2017. "Physically-Based Reduced-Order Capacity Loss Model for Graphite Anodes in Li-Ion Battery Cells." *Journal of Power Sources*. doi:10.1016/j.jpowsour.2016.12.099.
- Joachin, Humberto, Thomas D Kaun, Karim Zaghbi, and Jai Prakash. 2009. "Electrochemical and Thermal Studies of Carbon-Coated LiFePO₄ Cathode." *Journal of the Electrochemical Society* 156 (6). The Electrochemical Society: A401--A406.
- Ju, Y. S., and K. E. Goodson. 1999. "Phonon Scattering in Silicon Films with Thickness of Order 100 Nm." *Applied Physics Letters* 74 (20): 3005. doi:10.1063/1.123994.
- Julien, Christian M, Alain Mauger, Karim Zaghbi, and Henri Groult. 2014. "Comparative Issues of Cathode Materials for Li-Ion Batteries." *Inorganics* 2 (1). Multidisciplinary Digital Publishing Institute: 132–54.

- Kam, Kinson C, and Marca M Doeff. 2012. "Electrode Materials for Lithium Ion Batteries." *Mater. Matters* 7 (4): 56–62.
- Kermani, G., and E. Sahraei. 2017. "Review: Characterization and Modeling of the Mechanical Properties of Lithium-Ion Batteries." *Energies* 10 (11). doi:10.3390/en10111730.
- Kittel, Charles. 1962. *Elementary Solid State Physics: A Short Course*. Wiley.
- Klemens, P. G. 1951. "The Thermal Conductivity of Dielectric Solids at Low Temperatures (Theoretical)." *Proceedings of the Royal Society A: Mathematical, Physical and Engineering Sciences* 208 (1092): 108–33. doi:10.1098/rspa.1951.0147.
- Kosova, N V, N F Uvarov, E T Devyatkina, and E G Avvakumov. 2000. "Mechanochemical Synthesis of LiMn₂O₄ Cathode Material for Lithium Batteries." *Solid State Ionics* 135 (1–4). Elsevier: 107–14.
- Kushima, Akihiro, Jian Yu Huang, and Ju Li. 2012. "Quantitative Fracture Strength and Plasticity Measurements of Lithiated Silicon Nanowires by in Situ TEM Tensile Experiments." *ACS Nano* 6 (11). ACS Publications: 9425–32.
- Lai, Wei-Jen, Mohammed Yusuf Ali, and Jwo Pan. 2014. "Mechanical Behavior of Representative Volume Elements of Lithium-Ion Battery Cells under Compressive Loading Conditions." *Journal of Power Sources* 245: 609–23. doi:<http://dx.doi.org/10.1016/j.jpowsour.2013.06.134>.
- Lakes, R., P. Rosakis, and A. Ruina. 1993. "Microbuckling Instability in Elastomeric Cellular Solids." *Journal of Materials Science* 28 (17): 4667–72. doi:10.1007/BF00414256.
- Lee, Gyeong Chan, and Tae Uk Jung. 2012. "Design Comparisons of BLDC Motors for Electric Water Pump." In *2012 IEEE Vehicle Power and Propulsion Conference, VPPC 2012*. doi:10.1109/VPPC.2012.6422656.
- Li, C, H P Zhang, L J Fu, H Liu, Y P Wu, E Rahm, R Holze, and H Q Wu. 2006. "Cathode Materials Modified by Surface Coating for Lithium Ion Batteries." *Electrochimica Acta* 51 (19). Elsevier: 3872–83.
- Li, Deyu, Yiyang Wu, Philip Kim, Li Shi, Peidong Yang, and Arun Majumdar. 2003. "Thermal Conductivity of Individual Silicon Nanowires." *Applied Physics Letters* 83 (14): 2934–36. doi:10.1063/1.1616981.
- Li, Ling, Brian Post, Vlastimil Kunc, Amy M. Elliott, and M. Parans Paranthaman. 2017. "Additive Manufacturing of Near-Net-Shape Bonded Magnets: Prospects and Challenges." *Scripta Materialia*. doi:10.1016/j.scriptamat.2016.12.035.
- Liangruksa, M, and I K Puri. 2001. "Lattice Thermal Conductivity of a Silicon Nanowire under Surface Stress." *Journal of Applied Physics* 109 (1): 113501.
- "Lithium Titanate." 2017. *Wikipedia*. Accessed December 5. https://en.wikipedia.org/wiki/Lithium_titanate.

- Liu, Binghe, Hui Zhao, Huili Yu, Jie Li, and Jun Xu. 2017. "Multiphysics Computational Framework for Cylindrical Lithium-Ion Batteries under Mechanical Abusive Loading." *Electrochimica Acta* 256. Elsevier: 172–84.
- Liu, Ping, John Wang, Jocelyn Hicks-Garner, Elena Sherman, Souren Soukiazian, Mark Verbrugge, Harshad Tataria, James Musser, and Peter Finamore. 2010. "Aging Mechanisms of LiFePO₄ Batteries Deduced by Electrochemical and Structural Analyses." *Journal of The Electrochemical Society*. doi:10.1149/1.3294790.
- Liu, Wei, Min-Sang Song, Biao Kong, and Yi Cui. 2017. "Flexible and Stretchable Energy Storage: Recent Advances and Future Perspectives." *Advanced Materials* 29 (1): 1603436. doi:10.1002/adma.201603436.
- Liu, Xiao Hua, Li Zhong, Shan Huang, Scott X Mao, Ting Zhu, and Jian Yu Huang. 2012. "Size-Dependent Fracture of Silicon Nanoparticles during Lithiation." *Acs Nano* 6 (2). ACS Publications: 1522–31.
- Lu, Languang, Xuebing Han, Jianqiu Li, Jianfeng Hua, and Minggao Ouyang. 2013. "A Review on the Key Issues for Lithium-Ion Battery Management in Electric Vehicles." *Journal of Power Sources*. doi:10.1016/j.jpowsour.2012.10.060.
- Lundgren, Henrik. 2015. "Thermal Aspects and Electrolyte Mass Transport in Lithium-Ion Batteries." KTH Royal Institute of Technology.
- Ma, Z S, Z C Xie, Y Wang, P P Zhang, Y Pan, Y C Zhou, and Chunsheng Lu. 2015. "Failure Modes of Hollow Core--Shell Structural Active Materials during the Lithiation--Delithiation Process." *Journal of Power Sources* 290. Elsevier: 114–22.
- Maher, Kenza, and Rachid Yazami. 2013. "Effect of Overcharge on Entropy and Enthalpy of Lithium-Ion Batteries." *Electrochimica Acta* 101. Elsevier: 71–78.
- MATLAB, Release. 2017. "The Math Work Inc., 2017."
- Matthiessen, Augustus, and Carl Vogt. 1864. "On the Influence of Temperature on the Electric Conducting-Power of Alloys." *Philosophical Transactions of the Royal Society of London* 154 (1864): 167–200. doi:10.1098/rstl.1864.0004.
- Maznev, A. A., and O. B. Wright. 2014. "Demystifying Umklapp vs Normal Scattering in Lattice Thermal Conductivity." *American Journal of Physics* 82 (11): 1062–66. doi:10.1119/1.4892612.
- Miller, Melvin N. 1969. "Bounds for Effective Electrical, Thermal, and Magnetic Properties of Heterogeneous Materials." *Journal of Mathematical Physics*. doi:10.1063/1.1664794.
- Moura, Scott J., Federico Bribiesca Argomedo, Reinhardt Klein, Anahita Mirtabatabaei, and Miroslav Krstic. 2017. "Battery State Estimation for a Single Particle Model with Electrolyte Dynamics." *IEEE Transactions on Control Systems Technology*. doi:10.1109/TCST.2016.2571663.
- Nano-Produktion – Herstellung von Und Mit Nanotechnologie*. n.d. "Hessen-Nanotech NEWS 4/2006."

- Newman, John S., and Charles W. Tobias. 1962. "Theoretical Analysis of Current Distribution in Porous Electrodes." *Journal of The Electrochemical Society*. doi:10.1149/1.2425269.
- Newman, John, Karen E. Thomas, Hooman Hafezi, and Dean R. Wheeler. 2003. "Modeling of Lithium-Ion Batteries." In *Journal of Power Sources*. doi:10.1016/S0378-7753(03)00282-9.
- Novák, Petr, Felix Joho, Roman Imhof, Jan Christoph Panitz, and Otto Haas. 1999. "In Situ Investigation of the Interaction between Graphite and Electrolyte Solutions." *Journal of Power Sources*. doi:10.1016/S0378-7753(99)00119-6.
- Ogihara, Hideki. 2012. "Lithium Titanate Ceramic System as Electronic and Li-Ion Mixed Conductors for Cathode Matrix in Lithium-Sulfur Battery."
- Padhi, Akshaya K, Kirakodu S Nanjundaswamy, and John B Goodenough. 1997. "Phospho-Olivines as Positive-Electrode Materials for Rechargeable Lithium Batteries." *Journal of the Electrochemical Society* 144 (4). The Electrochemical Society: 1188–94.
- Park, Ok Kyung, Yonghyun Cho, Sanghan Lee, Ho-Chun Yoo, Hyun-Kon Song, and Jaephil Cho. 2011. "Who Will Drive Electric Vehicles, Olivine or Spinel?" *Energy & Environmental Science* 4 (5). Royal Society of Chemistry: 1621–33.
- Paulsen, J M, and J R Dahn. 1999. "Phase Diagram of Li- Mn- O Spinel in Air." *Chemistry of Materials* 11 (11). ACS Publications: 3065–79.
- Peabody, Christina, and Craig B. Arnold. 2011. "The Role of Mechanically Induced Separator Creep in Lithium-Ion Battery Capacity Fade." *Journal of Power Sources* 196 (19): 8147–53. doi:10.1016/j.jpowsour.2011.05.023.
- Peled, E. 1979. "The Electrochemical Behavior of Alkali and Alkaline Earth Metals in Nonaqueous Battery Systems—The Solid Electrolyte Interphase Model." *Journal of The Electrochemical Society*. doi:10.1149/1.2128859.
- Peled, E. 1997. "Advanced Model for Solid Electrolyte Interphase Electrodes in Liquid and Polymer Electrolytes." *Journal of The Electrochemical Society*. doi:10.1149/1.1837858.
- Pharr, Matt, Kejie Zhao, Xinwei Wang, Zhigang Suo, and Joost J Vlassak. 2012. "Kinetics of Initial Lithiation of Crystalline Silicon Electrodes of Lithium-Ion Batteries." *Nano Letters* 12 (9). ACS Publications: 5039–47.
- Pinson, M. B., and M. Z. Bazant. 2012. "Theory of SEI Formation in Rechargeable Batteries: Capacity Fade, Accelerated Aging and Lifetime Prediction." *Journal of the Electrochemical Society*. doi:10.1149/2.044302jes.
- Popescu, Mircea, Dave Staton, David Dorrell, Fabrizio Marignetti, and Douglas Hawkins. 2013. "Study of the Thermal Aspects in Brushless Permanent Magnet Machines Performance." In *Proceedings - 2013 IEEE Workshop on Electrical Machines Design, Control and Diagnosis, WEMDCD 2013*. doi:10.1109/WEMDCD.2013.6525165.
- Prada, E., D. Di Domenico, Y. Creff, J. Bernard, V. Sauvant-Moynot, and F. Huet. 2013. "A Simplified Electrochemical and Thermal Aging Model of LiFePO₄-Graphite Li-Ion

- Batteries: Power and Capacity Fade Simulations.” *Journal of the Electrochemical Society*. doi:10.1149/2.053304jes.
- Qi, Yue, Louis G Hector, Christine James, and Kwang Jin Kim. 2014. “Lithium Concentration Dependent Elastic Properties of Battery Electrode Materials from First Principles Calculations.” *Journal of The Electrochemical Society* 161 (11). The Electrochemical Society: F3010--F3018.
- Ramadesigan, V., P. W. C. Northrop, S. De, S. Santhanagopalan, R. D. Braatz, and V. R. Subramanian. 2012. “Modeling and Simulation of Lithium-Ion Batteries from a Systems Engineering Perspective.” *Journal of the Electrochemical Society* 159 (3): R31–45. doi:10.1149/2.018203jes.
- Ramos-Sanchez, G., F. A. Soto, J. M. Martinez de la Hoz, Z. Liu, P. P. Mukherjee, F. El-Mellouhi, J. M. Seminario, and P. B. Balbuena. 2016. “Computational Studies of Interfacial Reactions at Anode Materials: Initial Stages of the Solid-Electrolyte-Interphase Layer Formation.” *Journal of Electrochemical Energy Conversion and Storage*. doi:10.1115/1.4034412.
- Rao, K V, and A Smakula. 1965. “Dielectric Properties of Cobalt Oxide, Nickel Oxide, and Their Mixed Crystals.” *Journal of Applied Physics* 36 (6). AIP: 2031–38.
- Ravichandran, Guruswami, Ares J Rosakis, Jon Hodowany, and Phoebus Rosakis. 2002. “On the Conversion of Plastic Work into Heat During High-Strain-Rate Deformation.” In *AIP Conference Proceedings*, 620:557–62.
- Ren, Dongsheng, Xuning Feng, Languang Lu, Minggao Ouyang, Siqi Zheng, Jianqiu Li, and Xiangming He. 2017. “An Electrochemical-Thermal Coupled Overcharge-to-Thermal-Runaway Model for Lithium Ion Battery.” *Journal of Power Sources* 364. Elsevier: 328–40.
- Renganathan, Sindhuja, Godfrey Sikha, Shriram Santhanagopalan, and Ralph E White. 2010. “Theoretical Analysis of Stresses in a Lithium Ion Cell.” *Journal of The Electrochemical Society* 157 (2). The Electrochemical Society: A155--A163.
- Rong, Jiepeng, Xin Fang, Mingyuan Ge, Haitian Chen, Jing Xu, and Chongwu Zhou. 2013. “Coaxial Si/Anodic Titanium Oxide/Si Nanotube Arrays for Lithium-Ion Battery Anodes.” *Nano Research* 6 (3). Springer: 182–90.
- Safari, M., M. Morcrette, A. Teyssot, and C. Delacourt. 2009. “Multimodal Physics-Based Aging Model for Life Prediction of Li-Ion Batteries.” *Journal of The Electrochemical Society*. doi:10.1149/1.3043429.
- Sahraei, Elham, Michael Kahn, Joseph Meier, and Tomasz Wierzbicki. 2015. “Modelling of Cracks Developed in Lithium-Ion Cells under Mechanical Loading.” *RSC Advances* 5 (98): 80369–80. doi:10.1039/c5ra17865g.
- Sahraei, Elham, Joseph Meier, and Tomasz Wierzbicki. 2014. “Characterizing and Modeling Mechanical Properties and Onset of Short Circuit for Three Types of Lithium-Ion Pouch Cells.” *Journal of Power Sources* 247: 503–16. doi:10.1016/j.jpowsour.2013.08.056.

- Sarkar, A., P. Shrotriya, and A. Chandra. 2018. "Parametric Analysis of Electrode Materials on Thermal Performance of Lithium-Ion Battery: A Material Selection Approach." *Journal of the Electrochemical Society* 165 (9). doi:10.1149/2.0061809jes.
- Sarkar, Abhishek, Pranav Shrotriya, and Abhijit Chandra. 2017. "Fracture Modeling of Lithium-Silicon Battery Based on Variable Elastic Moduli." *Journal of The Electrochemical Society* 164 (11). The Electrochemical Society: E3606--E3612.
- Sato, Noboru. 2001. "Thermal Behavior Analysis of Lithium-Ion Batteries for Electric and Hybrid Vehicles." *Journal of Power Sources* 99 (1–2). Elsevier: 70–77.
- Satyavani, TVSL, B Ramya Kiran, V Rajesh Kumar, A Srinivas Kumar, and S V Naidu. 2016. "Effect of Particle Size on Dc Conductivity, Activation Energy and Diffusion Coefficient of Lithium Iron Phosphate in Li-Ion Cells." *Engineering Science and Technology, an International Journal* 19 (1). Elsevier: 40–44.
- Schilcher, Christiane, Chris Meyer, and Arno Kwade. 2016. "Structural and Electrochemical Properties of Calendered Lithium Manganese Oxide Cathodes." *Energy Technology* 4 (12). Wiley Online Library: 1604–10.
- Scrosati, Bruno, and Jürgen Garche. 2010. "Lithium Batteries: Status, Prospects and Future." *Journal of Power Sources* 195 (9). Elsevier: 2419–30.
- Sethuraman, Vijay A, Annam Nguyen, Michael J Chon, Siva P V Nadimpalli, Hailong Wang, Daniel P Abraham, Allan F Bower, Vivek B Shenoy, and Pradeep R Guduru. 2013. "Stress Evolution in Composite Silicon Electrodes during Lithiation/Delithiation." *Journal of The Electrochemical Society* 160 (4). The Electrochemical Society: A739--A746.
- Sheidaei, Azadeh, Xinran Xiao, Xiaosong Huang, and Jonathon Hitt. 2011. "Mechanical Behavior of a Battery Separator in Electrolyte Solutions." *Journal of Power Sources* 196 (20): 8728–34. doi:10.1016/j.jpowsour.2011.06.026.
- Shi, Siqi, Jian Gao, Yue Liu, Yan Zhao, Qu Wu, Wangwei Ju, Chuying Ouyang, and Ruijuan Xiao. 2015. "Multi-Scale Computation Methods: Their Applications in Lithium-Ion Battery Research and Development." *Chinese Physics B*. doi:10.1088/1674-1056/25/1/018212.
- Su, Xin, Qingliu Wu, Juchuan Li, Xingcheng Xiao, Amber Lott, Wenquan Lu, Brian W Sheldon, and Ji Wu. 2014. "Silicon-Based Nanomaterials for Lithium-Ion Batteries: A Review." *Advanced Energy Materials* 4 (1). Wiley Online Library.
- Takahashi, Kenji, and Venkat Srinivasan. 2015. "Examination of Graphite Particle Cracking as a Failure Mode in Lithium-Ion Batteries: A Model-Experimental Study." *Journal of The Electrochemical Society* 162 (4). The Electrochemical Society: A635--A645.
- Tao, Tao, Shengguo Lu, and Ying Chen. 2018. "A Review of Advanced Flexible Lithium-Ion Batteries." *Advanced Materials Technologies*. doi:10.1002/admt.201700375.
- Tarascon, J M, and M Armand. 2001. "Issues and Challenges Facing Rechargeable Lithium Batteries." *Nature* 414 (6861): 359–67. doi:10.1038/35104644.

- Thomas, Karen E, and John Newman. 2003. "Thermal Modeling of Porous Insertion Electrodes." *Journal of the Electrochemical Society* 150 (2). The Electrochemical Society: A176--A192.
- U.S. Energy Information Administration. 2018. "State Electricity Profiles." <https://www.eia.gov/electricity/state/>.
- Urban, Alexander, Dong Hwa Seo, and Gerbrand Ceder. 2016. "Computational Understanding of Li-Ion Batteries." *Npj Computational Materials*. doi:10.1038/npjcompumats.2016.2.
- Verma, Pallavi, Pascal Maire, and Petr Novák. 2010. "A Review of the Features and Analyses of the Solid Electrolyte Interphase in Li-Ion Batteries." *Electrochimica Acta*. doi:10.1016/j.electacta.2010.05.072.
- Viswanathan, Vilayanur V, Daiwon Choi, Donghai Wang, Wu Xu, Silas Towne, Ralph E Williford, Ji-Guang Zhang, Jun Liu, and Zhenguo Yang. 2010. "Effect of Entropy Change of Lithium Intercalation in Cathodes and Anodes on Li-Ion Battery Thermal Management." *Journal of Power Sources* 195 (11). Elsevier: 3720–29.
- Wang, Caiyun, and Gordon G. Wallace. 2015. "Flexible Electrodes and Electrolytes for Energy Storage." *Electrochimica Acta*. doi:10.1016/j.electacta.2015.04.067.
- Wang, Feng, Lijun Wu, Baris Key, Xiao-Qing Yang, Clare P Grey, Yimei Zhu, and Jason Graetz. 2013. "Electrochemical Reaction of Lithium with Nanostructured Silicon Anodes: A Study by In-Situ Synchrotron X-Ray Diffraction and Electron Energy-Loss Spectroscopy." *Advanced Energy Materials* 3 (10). Wiley Online Library: 1324–31.
- Wang, Jian, Yuan Chen, and Lu Qi. 2011. "The Development of Silicon Nanocomposite Materials for Li-Ion Secondary Batteries." *Open Materials Science Journal* 5 (1): 228–35.
- Wang, W. L., Sanboh Lee, and J. R. Chen. 2002. "Effect of Chemical Stress on Diffusion in a Hollow Cylinder." *Journal of Applied Physics* 91 (12): 9584–90. doi:10.1063/1.1477624.
- Whittingham, M S. 2004. "Lithium Batteries and Cathode Materials." *Chemical Reviews-Columbus* 104 (10): 4271–4302.
- Winter, Martin. 2009. "The Solid Electrolyte Interphase - The Most Important and the Least Understood Solid Electrolyte in Rechargeable Li Batteries." *Zeitschrift Fur Physikalische Chemie*. doi:10.1524/zpch.2009.6086.
- Wolfenstine, Jeff, Hyungyung Jo, Yong-Hun Cho, Isabel N David, Per Askeland, Eldon D Case, Hyunjoong Kim, Heeman Choe, and Jeff Sakamoto. 2013. "A Preliminary Investigation of Fracture Toughness of Li₇La₃Zr₂O₁₂ and Its Comparison to Other Solid Li-Ionconductors." *Materials Letters* 96. Elsevier: 117–20.
- Wrobel, Rafal, James Goss, Adrian Mlot, and Phil H. Mellor. 2014. "Design Considerations of a Brushless Open-Slot Radial-Flux PM Hub Motor." In *IEEE Transactions on Industry Applications*. doi:10.1109/TIA.2013.2284298.
- Wu, B., Y. Ren, and N. Li. 2011. "LiFePO₄ Cathode Material. In Electric Vehicles-The Benefits and Barriers." *InTech*.

- Wu, Wei, Xinran Xiao, Xiaosong Huang, and Shutian Yan. 2014. "A Multiphysics Model for the in Situ Stress Analysis of the Separator in a Lithium-Ion Battery Cell." *Computational Materials Science* 83: 127–36. doi:10.1016/j.commatsci.2013.10.002.
- Xiang, Xingde, James C Knight, Weishan Li, and Arumugam Manthiram. 2014. "Understanding the Effect of Co³⁺ Substitution on the Electrochemical Properties of Lithium-Rich Layered Oxide Cathodes for Lithium-Ion Batteries." *The Journal of Physical Chemistry C* 118 (38). ACS Publications: 21826–33.
- Xie, Zhoucan, Zengsheng Ma, Yan Wang, Yichun Zhou, and Chunsheng Lu. 2016. "A Kinetic Model for Diffusion and Chemical Reaction of Silicon Anode Lithiation in Lithium Ion Batteries." *RSC Adv.* 6 (27): 22383–88. doi:10.1039/C5RA27817A.
- Xing, Lidan, Oleg Borodin, Grant D. Smith, and Weishan Li. 2011. "Density Functional Theory Study of the Role of Anions on the Oxidative Decomposition Reaction of Propylene Carbonate." *Journal of Physical Chemistry A*. doi:10.1021/jp206153n.
- Xu, Jun John, Andrew J Kinser, Boone B Owens, and William H Smyrl. 1998. "Amorphous Manganese Dioxide: A High Capacity Lithium Intercalation Host." *Electrochemical and Solid-State Letters* 1 (1). The Electrochemical Society: 1–3.
- Xu, Wen, Gang Zhang, and Baowen Li. 2015. "Effects of Lithium Insertion on Thermal Conductivity of Silicon Nanowires." *Applied Physics Letters* 106 (17). doi:10.1063/1.4919587.
- Yamada, Atsuo, Hiroshi Koizumi, Noriyuki Sonoyama, and Ryoji Kanno. 2005. "Phase Change in Li_xFePO₄." *Electrochemical and Solid-State Letters* 8 (8). The Electrochemical Society: A409–A413.
- Yan, Jiwang, Zhiyu Zhang, and Tsunemoto Kuriyagawa. 2011. "Effect of Nanoparticle Lubrication in Diamond Turning of Reaction-Bonded SiC." *International Journal of Automation Technology* 5 (3): 307–12.
- Yang, Fuqian. 2005. "Interaction between Diffusion and Chemical Stresses." *Materials Science and Engineering: A* 409 (1–2). Elsevier: 153–59.
- Yang, Xiao-Hu, Si-Cong Tan, and Jing Liu. 2016. "Thermal Management of Li-Ion Battery with Liquid Metal." *Energy Conversion and Management* 117. Elsevier: 577–85.
- Yen, William W. 2002. Wettable nonwoven battery separator. US6495292B1, issued 2002. <https://patents.google.com/patent/US6495292B1/en>.
- Yuan, Li-Xia, Zhao-Hui Wang, Wu-Xing Zhang, Xian-Luo Hu, Ji-Tao Chen, Yun-Hui Huang, and John B Goodenough. 2011. "Development and Challenges of LiFePO₄ Cathode Material for Lithium-Ion Batteries." *Energy & Environmental Science* 4 (2). Royal Society of Chemistry: 269–84.
- Zhang, Dong, Branko N Popov, and Ralph E White. 2000. "Modeling Lithium Intercalation of a Single Spinel Particle under Potentiodynamic Control." *Journal of The Electrochemical Society* 147 (3). The Electrochemical Society: 831–38.

- Zhang, Jun, Noboru Kikuchi, Victor Li, Albert Yee, and Guy Nusholtz. 1998. "Constitutive Modeling of Polymeric Foam Material Subjected to Dynamic Crash Loading." *International Journal of Impact Engineering* 21 (5): 369–86. doi:10.1016/S0734-743X(97)00087-0.
- Zhang, Wei Jun. 2011. "A Review of the Electrochemical Performance of Alloy Anodes for Lithium-Ion Batteries." *Journal of Power Sources*. doi:10.1016/j.jpowsour.2010.07.020.
- Zhang, Xiangchun, Ann Marie Sastry, and Wei Shyy. 2008. "Intercalation-Induced Stress and Heat Generation within Single Lithium-Ion Battery Cathode Particles." *Journal of The Electrochemical Society* 155 (7). The Electrochemical Society: A542--A552.
- Zhang, Xiangchun, Wei Shyy, and Ann Marie Sastry. 2007. "Numerical Simulation of Intercalation-Induced Stress in Li-Ion Battery Electrode Particles." *Journal of the Electrochemical Society* 154 (10). The Electrochemical Society: A910--A916.
- Zhang, Xiaowei, Elham Sahraei, and Kai Wang. 2016. "Deformation and Failure Characteristics of Four Types of Lithium-Ion Battery Separators." *Journal of Power Sources* 327: 693–701. doi:10.1016/j.jpowsour.2016.07.078.
- Zhang, Xuerong, James K. Pugh, and Philip N. Ross. 2001. "Computation of Thermodynamic Oxidation Potentials of Organic Solvents Using Density Functional Theory." *Journal of The Electrochemical Society*. doi:10.1149/1.1362546.
- Zhao, Kejie, Matt Pharr, Joost J Vlassak, and Zhigang Suo. 2010. "Fracture of Electrodes in Lithium-Ion Batteries Caused by Fast Charging." *Journal of Applied Physics* 108 (7). AIP: 73517.
- Zhao, Kejie, Matt Pharr, Qiang Wan, Wei L Wang, Efthimios Kaxiras, Joost J Vlassak, and Zhigang Suo. 2012. "Concurrent Reaction and Plasticity during Initial Lithiation of Crystalline Silicon in Lithium-Ion Batteries." *Journal of The Electrochemical Society* 159 (3). The Electrochemical Society: A238--A243.
- Zhao, Kejie, Wei L Wang, John Gregoire, Matt Pharr, Zhigang Suo, Joost J Vlassak, and Efthimios Kaxiras. 2011. "Lithium-Assisted Plastic Deformation of Silicon Electrodes in Lithium-Ion Batteries: A First-Principles Theoretical Study." *Nano Letters* 11 (7). ACS Publications: 2962–67.
- Zhao, Xin, Cary M Hayner, Mayfair C Kung, and Harold H Kung. 2011. "In-Plane Vacancy-Enabled High-Power Si--Graphene Composite Electrode for Lithium-Ion Batteries." *Advanced Energy Materials* 1 (6). Wiley Online Library: 1079–84.
- Zhu, H.X., N.J. Mills, and J.F. Knott. 1997. "Analysis of the High Strain Compression of Open-Cell Foams." *Journal of the Mechanics and Physics of Solids* 45 (11–12): 1875–1904. doi:10.1016/S0022-5096(97)00027-6.
- Zhu, Yujie, and Chunsheng Wang. 2010. "Galvanostatic Intermittent Titration Technique for Phase-Transformation Electrodes." *The Journal of Physical Chemistry C* 114 (6). ACS Publications: 2830–41.
- Zhu, Zimu, David A. Romero, Daniel P. Sellan, Aydin Nabovati, and Cristina H. Amon. 2013. "Assessment of the Holland Model for Silicon Phonon-Phonon Relaxation Times Using

Lattice Dynamics Calculations.” In *Journal of Applied Physics*, 113:173511. doi:10.1063/1.4803514.

Zu, Chen Xi, and Hong Li. 2011. “Thermodynamic Analysis on Energy Densities of Batteries.” *Energy and Environmental Science*. doi:10.1039/c0ee00777c.